HI JENA

Helmholtz Institute Jena

ANNUAL REPORT 2020

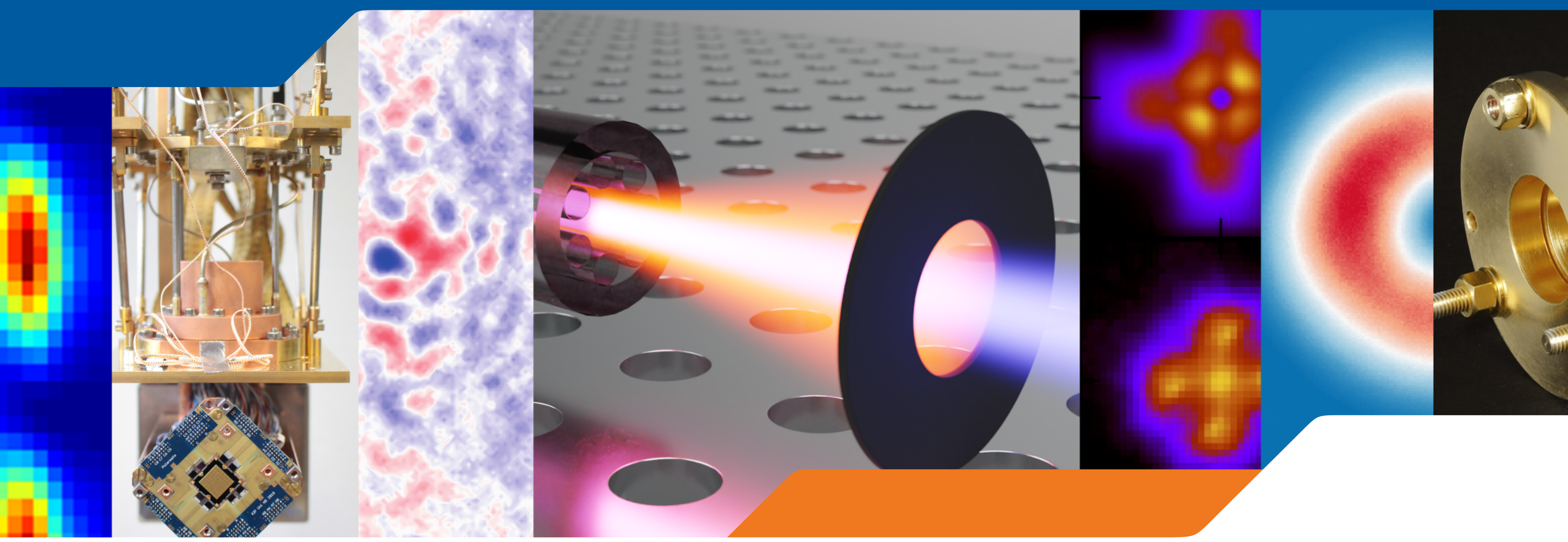

FRIEDRICH-SCHILLER-UNIVERSITÄT JENA

HELMHOLTZ ZENTRUM DRESDEN ROSSENDORF

HELMHOLTZ INSTITUTE JENA

ANNUAL REPORT 2020

IMPRINT

Publisher:	Helmholtz-Institut Jena, Fröbelstieg 3, 07743 Jena, Germany (http://www.hi-jena.de) @ GSI Helmholtzzentrum für Schwerionenforschung GmbH Darmstadt, Germany (http://www.gsi.de) GSI is member of the Helmholtz association of national research centers (http://www.helmholtz.de).
Editors:	Daniel Seipt and Arno Klenke
DOI:	10.15120/GSI-2021-00839 (http://dx.doi.org/10.15120/GSI-2021-00839)
Publication date:	July 2021

CONTENTS

PHOTON AND PARTICLE SPECTROSCOPY 37

FOREWORD

Dear friends and members of the Helmholtz Institute Jena,

The Helmholtz Institute Jena is situated on the campus of the Friedrich Schiller University Jena (FSU) with the Helmholtz centers DESY and HZDR as additional partners. It combines the established scientific expertise of the University and of our partners with the strategic mission of GSI. Embedded into the Faculty of Physics and Astronomy of the Friedrich-Schiller-University Jena, the focus of research at HI Jena is on fundamental and applied research at the borderline of strong-field physics, relativistic light-matter interactions and fundamental quantum processes.

For its research HI Jena profits substantially from the close involvement of the Institute for Optics and Quantum Electronics, the Institute for Theoretical Physics, and the Institute of Applied Physics (closely coupled to Fraunhofer IOF). Moreover, many experimental research projects are exploiting the unique research infrastructures of the large scale facilities at GSI at Darmstadt and DESY including the flagship projects FAIR and XFEL. In addition, at the campus of the FSU, HI Jena provides excellent research opportunities by operating its own infrastructures which prove to be highly attractive for students and young scientists (see below). As such, the high-power laser systems POLARIS and JETi200 have to be mentioned as well as a dedicated x-ray laboratory and a cryo-laboratory (since very recently, see below). For a detailed insight into all the various research activities and the multitude of research highlights achieved, please check out the details of our current Annual Report for 2020.

In the 12th year after its establishment, the buildup phase of the Institute has been finished and all (new) W3 positions could meanwhile be filled. Consequently, and despite the impact of the Covid-19 pandemic, all research groups are very active and in full swing leading to a continuous growth of the Institute, currently reaching about 100 scientists including PhD students and support personnel. Of course, the demand for additional office and lab space is increasing as well, and the institute is very grateful to the Federal State of Thuringia for providing it with an additional institute's building which is currently being built (civil construction is progressing very well as documented by the photos in Figure 1). The new building is located at the campus of the FSU Jena in direct neighborhood to the existing institute's building at Fröbelstieg 3. Both buildings are connected via a tunnel, enabling the use of the available high-power laser infrastructure in both buildings. Civil construction has started in March 2020 and the building is expected to be available in 2022.

Regarding strategic developments, particular focus is currently directed on enabling techniques for quantum technology and quantum technology itself, as well as on data science. Illustrating its sustained engagement in enabling techniques for quantum technology, HI-Jena has joined the consortium of leading academic institutions and industry in Germany, "Consortium for Cryogenic Detectors and Superconducting Electronics". As a first result, the cryo-laboratory started its operation recently (being a common activity of HI-Jena and the Institute of Solid State Physics of the University of Jena). Note, this activity is also part of the Helmholtz strategy document for Quantum Technologies as well as a corner stone for the engagement of HI-Jena for the application of a Distributed Detector Laboratory (DDL). Related to quantum technology, the initiative

Figure 1: Construction site of the additional institute building which is expected to be available in spring 2022.

“Quantum Hub Thuringia” by the State of Thuringia needs to be highlighted.

One central focus of the Helmholtz Institute Jena is the promotion of young scientists during the different phases of their scientific career. In particular, doctoral students are supported by the research school RS-APS of HI Jena, whose program was also affected by the Covid-19 pandemic situation. The Research School adapted well to the given situation about the academic program, moving to digital platforms. The RS-APS seminar was held via Zoom and the annual Lecture Week of RS-APS which was traditionally designed as a retreat was reorganized as a modified online version. The partnering graduate school HGS-HIRe for FAIR which offers a dedicated soft skills series for scientists to its participants changed its program to a virtual workshop series and ensured the possibility for the young researchers to participate in such courses relevant for a structured PhD program. Moreover, in 2020, RS-APS welcomed five new students to its graduate program, while the total number remains stable on a high level with 52 students participating in the research school (approximately half of the students are financed by 3rd party funding).

Research School of the Helmholtz Institute Jena

R. Märtin*[1], C. Hahn[1], and G. Weber[1]

[1]Helmholtz Institute Jena, Fröbelstieg 3, 07743 Jena

The Research School of Advanced Photon Science (RS-APS) of the HI Jena exists now for eight years and is an established institution for the PhD students working at the Helmholtz Institute Jena.

The Research School RS-APS was affected by the Covid-19 pandemic situation as all other institutions related to scientific research and education. In particular, the first lockdown had a large impact on the doctoral students and their scientific work at the University and the Helmholtz Institute Jena. Besides the restricted contact ("stay at home!"), research facilities stopped their operation and the access to the laboratories and offices was prohibited. Several doctoral students whose research was dedicated to a project at GSI, DESY or simply lab work on the campus of the university could not continue their projects and had to pause. The situation was compounded further by the lack of scientific and academic exchange with colleagues which is of great importance for the individual scientific work, and the additional burden for several students through childcare at home. Especially this situation required the support by the research school and the Helmholtz Institute Jena, for example through the extension of the duration of the financial support.

Figure 1: Picture of the entrance of the building of the HI Jena. Due to Covid-19 the access was limited or partially forbidden.

However the Research School and the HI Jena adapted well to the given situation, addressing the restrictions by using digital platforms. The RS-APS seminar was held via Zoom and the annual Lecture Week of RS-APS which was traditionally designed as a retreat was reorganized as a series of online lectures. The 8th Joint Lecture Week of RS-APS and HGS-HIRe was offered as a mini series of lectures in the afternoon of four days with the title "The Prospects of Cryogenic Detectors and Superconducting Electronics: from Fundamental Research to Applications". The scientific program covered various aspects of cryogenic-based sensor technology and electronics. The lecturers Prof. Christian Enss (University Heidelberg), Dr. Ronny Stolz (Leibniz-IPHT) and Dr. Volker Tympel (Helmholtz Institute Jena) gave a broad overview of this research for the ca. 25 students participating.

The partnering graduate school HGS-HIRe for FAIR which offers a dedicated soft skill series for scientists to its participants changed the whole to program to a virtual workshop series and ensured the possibility for the young researchers to participate in such courses relevant for a structured PhD program.

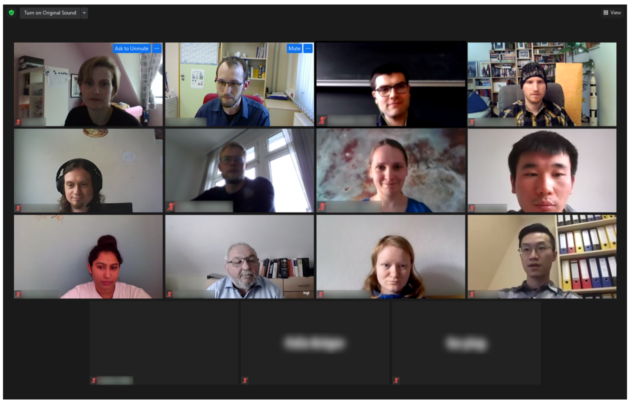

Figure 2: Picture taken during the bi-weekly RS-APS seminar. The seminar is held via Zoom in the moment.

The so-called PhD committee meeting, which is foreseen to be one of the main building blocks of structured PhD education, actually profits from the focus on digital meetings. The meeting between student, their supervisor and an additional co-supervisor ensures the exchange between doctoral student and supervisor and tracks the progress and status of the student's doctoral project. During the pandemic the decentralized work using virtual meeting tools helped to arrange these important discussion meetings more often. Therefore we encountered an increase of the conducted PhD committee meetings. This is of course of special importance while the pandemic restrictions are ongoing and the individual student has less chances for the scientific exchange on face-to-face basis. Despite the forced break due to the first pandemic shutdown nine doctoral students have finished their doctoral studies with success in 2020, which amounts to a constant completion rate. RS-APS welcomed five new students to its graduate program, while the total number remains stable on a high level with 52 students participating in the research school.

*r.maertin@hi-jena.gsi.de

HIGH POWER LASER DEVELOPMENT

ATHENA: A high-contrast frontend for the PEnELOPE laser facility

M. Hornung*[1,2], G. A. Becker[2], T. Weickhardt[2], M. Hellwing[2], M. Siebold[3], M. Löser[3], D. Albach[3], U. Schramm[3], and M. C. Kaluza[1,2]

[1]Helmholtz Institute Jena, Fröbelstieg 3, 07743 Jena; [2]Institute of Optics and Quantum Electronics (FSU Jena), Max-Wien Platz 1, 07743 Jena; [3]Helmholtz Zentrum Dresden Rossendorf, Bautzner Landstraße 400, 01328 Dresden

Within the framework of the ATHENA project, we are developing a high-contrast frontend to generate laser pulses with a center wavelength of 1030 nm, a FWHM-bandwidth of 25 nm and an output energy of 100 µJ. The system is based on chirped pulse amplification with subsequent crossed polarized wave generation [1]. The generated laser pulses will in future be used as seed pulses at the PEnELOPE [2] laser facility at HZDR.

During the past years we have designed and setup a CPA based laser frontend which consists of a seed-source, a pulse-picker, a pulse stretcher, a pulse compressor and an amplifier. After commissioning and demonstrating that the individual components are operational as a frontend system in 2019 [3] we have optimized and finalized the system with respect to the overall size, robustness and stability in 2020.

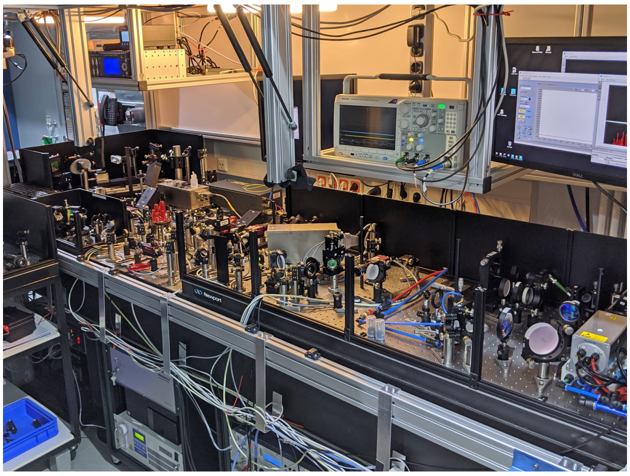

Figure 1: Photo of the ATHENA frontend laser system for PEnELOPE.

Furthermore, in 2020 the system was partially disassembled to be reassembled on robust optical breadboards with corresponding housings to allow for an easy transport from Jena to Dresden in the future and provide stable long-term operation. A photo of the reassembled setup with open housings is shown in Fig. 1.

In addition to the aforementioned CPA system a XPW system is required to enhance the temporal contrast. The XPW vacuum and optical system was assembled and tested due to space constraints on a separate optical table with POLARIS [4] laser pulses. The polarization quality of the optical components (e.g. polarizers, mirrors, vacuum transmission windows, ...) was verified in measurements to be significantly better than 10^{-6}. The final optimization of the XPW generation is still ongoing and close to finalization. A photo of the realized XPW system is shown in Fig. 2.

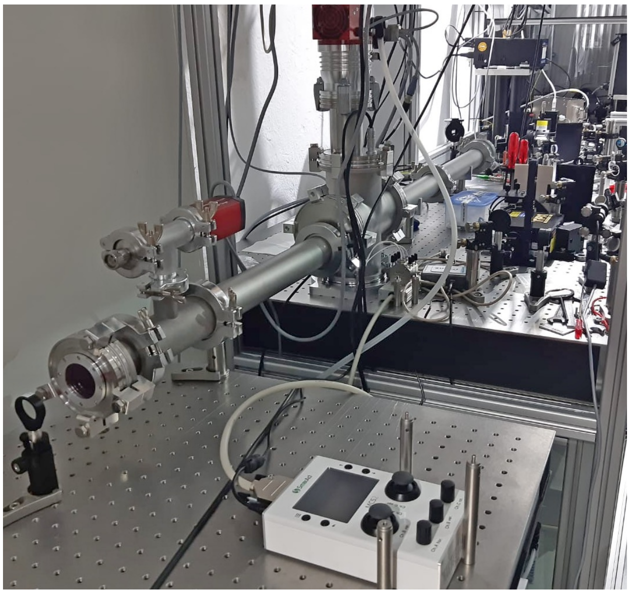

Figure 2: Vacuum and optical system for XPW generation.

In parallel to the technical finalization and full optical characterization of the frontend system in Jena we are preparing the delivery to HZDR and the installation of the frontend into the PEnELOPE laser system in the near future.

References

[1] H. Liebetrau *et al.*, Opt. Express **22**, 24776 (2014).

[2] D. Albach *et al.*, High Power Laser Sci. Eng. **7**, e1 (2019).

[3] M. Hornung *et al.*, HI Jena Annual Report 2019.

[4] M. Hornung *et al.*, Opt. Lett. **41**, 5413 (2016).

*marco.hornung@uni-jena.de

Stretcher Compressor Simulation with Aberrated Optics

M. Hornung*[1,2], M. Siebold[3], M. Löser[3], U. Schramm[3], and M. C. Kaluza[1,2]

[1]Helmholtz Institute Jena, Fröbelstieg 3, 07743 Jena; [2]Institute of Optics and Quantum Electronics (FSU Jena), Max-Wien Platz 1, 07743 Jena; [3]Helmholtz Zentrum Dresden Rossendorf, Bautzner Landstraße 400, 01328 Dresden

We performed simulations for CPA stretcher compressor systems with measured aberrated optic surfaces. These simulations were developed to understand and further optimize the temporal pulse structure of laser pulses which were stretched and compressed with existing and planned stretcher compressor systems.

The temporal pulse structure on a picosecond and femtosecond timescale is one of the most important characteristics of a high-power laser pulse used in high-intensity experiments. Deviations from a perfect temporal pulse structure (e.g. significant picosecond pedestal or aberrated spectral phase) are partially due to the usage of "real" optics in the stretcher-compressor systems. In order to connect measured data of temporal pulse structures with the quality of the used optics (e.g. surface roughness and flatness) in different laser systems (e.g. PEnELOPE [1] and POLARIS [2]) we developed a simulation using the FRED software [3]. FRED is a commercial software which is able to simulate the propagation of coherent light through optical systems.

The stretcher-compressor system of the PEnELOPE laser consist of an Offner-type stretcher and a Treacy-type compressor. This setup temporally stretches the laser pulses from 100 fs to 3 ns. After amplification the pulses are temporally compressed again. The design of this system was used in the simulations and is shown schematically in the upper left inset in Fig. 1. To verify and test the absolute simulation performance we inserted a small piston stamp mirror on the Offner stretcher convex mirror with small misalignments. The resulting optical path delay (OPD) for different scenarios is shown in Fig. 1.

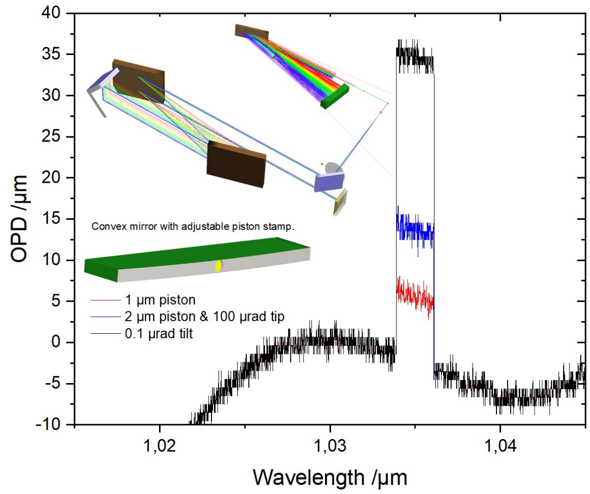

Figure 1: Calculated optical path delay vs. wavelength for different test scenarios. Inset: optical system setup.

In Fig. 2 a calculation for the different optical path lengths for a strongly aberrated convex mirror in the PEnELOPE stretcher is shown. For this calculation the measured surface quality was used and leads — as expected — to a comparably large optical path delay for different wavelengths. In this case the simulation fits well to the measured (not optimal) pulse structure. The used optic was meanwhile exchanged with a significantly improved optic and further improvement is going on.

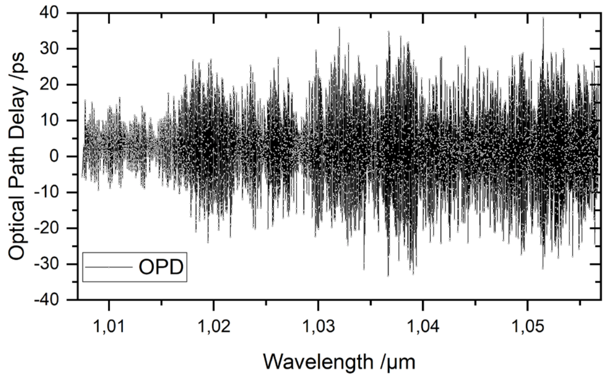

Figure 2: Optical path delay vs. wavelength for a stretcher compressor system with a strongly aberrated optic.

Further measurements and simulations for different scenarios and systems are ongoing. In the future we will extend and use the model to benchmark and optimize our laser systems with respect to optics quality and the temporal pulse structure.

References

[1] `https://photonengr.com/fred-software/`

[2] D. Albach *et al.*, High Power Laser Sci. Eng. **7**, e1 (2019).

[3] M. Hornung *et al.*, Opt. Lett. **41**, 5413 (2016).

* marco.hornung@uni-jena.de

A highly-efficient diode pumped Joule-class laser with a novel unstable cavity and its application for laser-shock peening

Jörg Körner*[2,1], Jürgen Reiter[1,2], Joachim Hein[2,1], and Malte C. Kaluza[2,1]

[1]Helmholtz Institute Jena, Fröbelstieg 3, 07743 Jena, Germany; [2]Institute of Optics and Quantum Electronics, Max-Wien-Platz 1, 07743 Jena

With a novel gain-shaped unstable laser cavity approach a compact diode pumped cryogenically cooled Yb:YAG laser delivers more than 1 J output energy in a 10 ns pulse at 10 Hz. The hexagonal tophat output profile is directly generated by the laser cavity with an outstanding optical to optical efficiency of up to 37%. The laser demonstrated its great potential in a proof of principle experiment on laser shock peening of aluminum.

Although pulsed ytterbium doped lasers intrinsically feature a higher efficiency and a better compatibility with laser diode pumping than their neodymium doped counterparts, their potential is so far mainly demonstrated in scientific systems as for instance described in [1]. The reasons are relatively small cross sections requiring complex energy extraction schemes.

Especially the utilization of unstable cavities widely reduces the complexity of a high energy laser as such allow to directly generate a high pulse energy within a single resonator with according beam size. Nevertheless, the state of the art approaches to generate a suitable tophat beam profile need a high gain rendering it incompatible with ytterbium doped media. Here we show that our novel design based on gain shaping of the cavity mode allows to significantly increase the cavity feedback [2].

Using this technology we set up an electro-optically q-switched laser with cryogenically cooled Yb:YAG as the gain medium. The laser is pumped by a 7 kW peak power laser diode module with a homogenized hexagonal tophat pump profile. The Yb:YAG is a ceramic with a Cr:YAG cladding to suppress amplified spontaneous emission and transverse lasing. The active medium is cooled to about 80 K using a bath cryostat in a high vacuum environment.

A confocal unstable cavity consisting of a convex mirror with a radius of 4 m and a concave mirror with radius of 5 m is forming the resonator resulting in a round-trip magnification of 1.25. Output coupling is realized with a thin film polarizer in combination with a Pockels cell and a quarter wave plate. The total footprint of the system is about 60x80cm^2.

The system generates a hexagonal tophat beam profile with up to 1.1 J output energy in 10 ns pulses in q-switch mode with a record high optical to optical efficiency of up to 37%. The repetition rate of the laser could be increased up to 10 Hz without significant impact on the output parameters as shown in figure 1 as a function of the pump pulse duration. For higher repetition rates a reduced output energy was observed due to the limited cooling capacity of the cryostat.

* joerg.koerner@uni-jena.de

With this laser a proof of principle experiment was conducted to demonstrate its suitability for laser shock peening. For the test an aluminum alloy EN AW 7075 sample was treated. It was coated with black vinyl tape to increase absorption and submerged in a water filled bowl approximately 1 mm below liquid level. The laser beam having an intensity of approximately 3 GW/cm^2 was incident with a small inclination from the top. The treated area was covered by stitching shots together with an overlap of 50%.

The sample was afterwards analyzed using the hole drilling method. The generated compressive residual stress was imparted up to 0.5 mm depth in the sample with a peak value of 200 MPa on its surface.

Given the preliminary character of this test, these results can be seen as very promising with respect to the intended application, but it is not limited to it. The investigation of additional applications for instance as pump laser for broad band OPCPAs or for damage testing are intended.

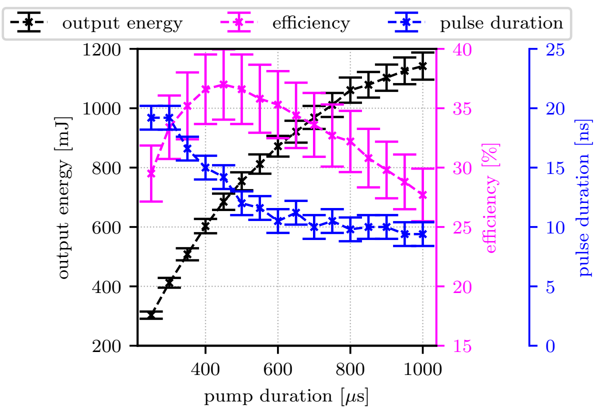

Figure 1: Output energy, optical to optical efficiency with respect to absorbed pump energy and output pulse duration as a function of pump pulse duration.

The work was performed in cooperation with Sanin Zulić, Danijela Rostohar, and Tomáš Mocek from HiLASE. The authors further acknowledge funding through ERDF and the Czech Rep. (CZ.02.1.01/0.0/0.0/15_006/ 0000674); EU programs No. 739573 and 654148; Thuringian Ministry TMWWDG (2016FE9058); German Ministry BMBF (03ZIK445, 05P15SJFA1, 03Z1H531, 03VNE2068D).

References

[1] P. Mason *et al.*, Optica **4**, 438 (2017).

[2] J. Körner, S. Zulić, D. Rostohar, A. Lucianetti, and T. Mocek, Optics Express **27**, 21622 (2019).

Diode pulse pumped, electro-optically q-switched, cryogenic Tm:YAG laser operating at 1.88 µm

Jörg Körner*[2,1], Jürgen Reiter[1,2], Joachim Hein[2,1], and Malte C. Kaluza[2,1]

[1]Helmholtz Institute Jena, Fröbelstieg 3, 07743 Jena, Germany; [2]Institute of Optics and Quantum Electronics, Max-Wien-Platz 1, 07743 Jena

We present first results on a cryogenically cooled, diode-pulse-pumped Tm:YAG laser oscillator with electro-optical q-switching. With this prototype we are investigating a novel strategy for high energy short pulse generation based on thulium doped gain media. The extra-long fluorescence lifetime is promising to reduce the necessary amount of needed diode power per Joule short pulse output. According to the spectral properties of Tm:YAG the design parameters, such as pump intensity, are required to be significantly different from that used in neodymium or ytterbium based laser systems. The laser oscillator prototype delivers more than 2 mJ with a pulse length of 650 ns in q-switch mode and 18 ns in cavity dump mode.

Thulium doped laser media exhibit an extraordinary long radiative lifetime, which is typically more than ten times longer compared to corresponding ytterbium doped gain media. They can be pumped with high power laser diodes close to 800 nm, while emission is in the range from 1.8 µm to 2 µm with a nevertheless low quantum defect, due to the intrinsic cross relaxation process.

This in principle should enable thulium based laser systems to generate high energy pulses in the short wave infrared regime with a highly advantageous ratio of output energy compared to installed pump power. In addition to applications in industry and medicine such laser systems would be ideal as pump lasers for high energy broad band Cr:ZnSe or Cr:ZnS laser amplifiers.

Using the spectroscopic parameters of cryo-cooled Tm:YAG [1] in a numerical simulation of the laser process (cf. figure 1) we found that under pulse pumped operation saturation of the laser medium will already occur at intensities as low as approximately 2 kW/cm^2, if pump pulses are as long as the radiative lifetime. This is more than 10 times lower compared to similar Yb:YAG lasers.

Therefore, a significantly lower pump intensity has to be chosen. Based on these results we designed a stable resonator oscillator with an 8 at.% doped Tm:YAG active mirror laser medium. The crystal was cooled to 120 K within a high vacuum cryostat. A 30 W fiber coupled laser diode at 783 nm was used for pumping. The spot size was 0.7 mm in diameter which results in an even higher pump intensity than proposed by the simulation to provide some power reservation for the compensation of additional losses.

Due to the low temperature the major emission is at 1.88 µm, which fits well with the absorption of chromium doped laser media. Nevertheless, this wavelength is strongly absorbed in air due to humidity. Therefore, the whole system is enclosed in a tent purged with dry nitrogen gas. The q-switch and cavity dump operation was realized with an RTP Pockels cell in combination with a polarizer.

* joerg.koerner@uni-jena.de

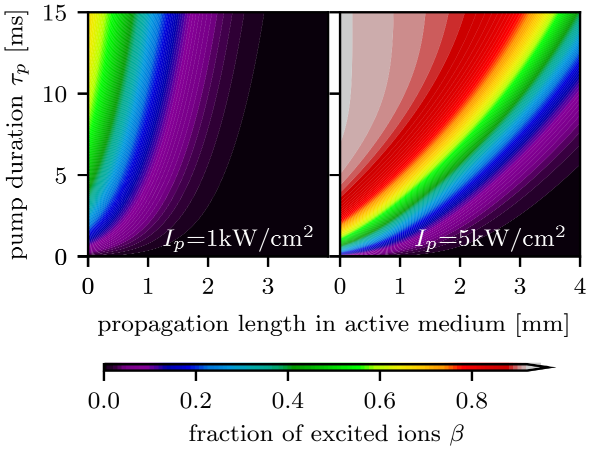

Figure 1: Simulation of the pump process in a 8 at.% doped Tm:YAG assuming 15 ms fluorescence lifetime. Relative inversion density β as a function of pump propagation distance in the active medium z and pump duration τ_p for a pump intensity of 1 kW/cm^2 (left) and 5 kW/cm^2 (right).

The system produced pulses with up to 2.55 mJ in q-switch operation with a pump pulse duration of 1.6 ms. The according pulse length was 650 ns. For the same pump duration under cavity dump operation 2.2 mJ where obtained with a pulse duration of 18 ns.

The results from this first test indicate that the high doping level in the crystal triggered unwanted decay mechanisms and significantly limited the usable fluorescence lifetime. A lower doping level should mitigate this issue. More details on the actual laser setup and simulation are published elsewhere [2].

The work was performed in cooperation with Sanin Zulić, Danijela Rostohar, and Tomáš Mocek from HiLASE. The authors further acknowledge funding through ERDF and the Czech Rep. (CZ.02.1.01/0.0/0.0/15_006/ 0000674); EU programs No. 739573 and 654148; Thuringian Ministry TMWWDG (2016FE9058); German Ministry BMBF (03ZIK445, 05P15SJFA1, 03Z1H531, 03VNE2068D).

References

[1] J. Körner *et al.*, Journal of Luminescence **202**, 427 (2018).

[2] J. Körner *et al.*, High Power Laser Science and Engineering **9** (2021).

Spectroscopic characterization of the laser media Yb^{3+}-doped $KGd(WO_4)_2$, $KY(WO_4)_2$, $YAlO_3$ and $YLiF_4$

Jörg Körner*[2,1], Jürgen Reiter[1,2], Clemens Anschütz[2], Joachim Hein[2,1], and Malte C. Kaluza[2,1]

[1]Helmholtz Institute Jena, Fröbelstieg 3, 07743 Jena, Germany; [2]Institute of Optics and Quantum Electronics, Max-Wien-Platz 1, 07743 Jena

Fluorescence lifetime, absorption and emission cross sections of ytterbium doped $KGd(WO_4)_2$, $KY(WO_4)_2$, $YAlO_3$ and $YLiF_4$ as a function of temperature in the range from 80 K to 280 K were determined. The measurement was done with a setup that intrinsicly minimizes re-absortion effects. By combining the Fuchtbauer-Ladenburg equation and the McCumber approach the validity of the results was cross-checked and measurement limitations widely removed. The retrieved data can be used as a basis for detailed numerical simulations for according laser setups to optimize efficiency and bandwidth with respect to temperature.

Exact data on the cross sections and fluorescence lifetime of a laser medium is mandatory for the design of new oscillators and amplifiers. In case of ytterbium based systems cryogenic cooling is often considered as a promising strategy for increasing efficiency and output power. As the spectral parameters significantly depend on temperature according spectral data are required.

The investigated ytterbium doped host materials $KGd(WO_4)_2$, $KY(WO_4)_2$, $YAlO_3$ and $YLiF_4$, have recently attracted interest as broadband laser media. Other applications are laser cooling and laser operation with extremely low quantum defect.

Polarized transmission and fluorescence spectra were acquired in the setup shown in Figure 1. As it has been shown in previous fluorescence measurements [1, 2] this special geometry widely reduces the influence of re-absorption and therefore allows for precise measurements especially in spectral ranges with underlying absorption. Measurements of the fluorescence lifetime were carried out in the same setup by replacing the spectrometer with a photo-diode. The samples where mounted in a liquid nitrogen flow cryostat under high vacuum conditions to avoid condensation.

Absorption cross sections were obtained from the transmission measurements using Lambert-Beer's law. Emission cross sections were obtained via two independent methods. One is the McCumber relation, which allows for the direct calculation of the emission cross sections from the previously determined absorption cross sections. The other is the Fuchtbauer-Ladenburg equation, which is based on the fluorescence spectra and the knowledge of the radiative lifetime. While the latter yields more reliable results in low absorbing spectral ranges, the first is more appropriate in high absorbing areas. Results from both methods where adapted to each other by using the radiative lifetime as the free fitting parameter. The values for the radiative lifetime obtained by this method are in good agreement with the experimentally determined fluorescence lifetimes.

It was found that all materials maintain a broad band amplification character also in the low temperature range, though the spectrum becomes more structured, while the peak emission cross sections are significantly increased. Yb:YLF and Yb:YAP feature a strong emission lime close to 1000 nm for cryogenic temperatures, which suggest a high potential for low quantum defect lasing applications. Detailed data is published elsewhere [3]. This data are used for laser optimization within different related projects (see funding statements).

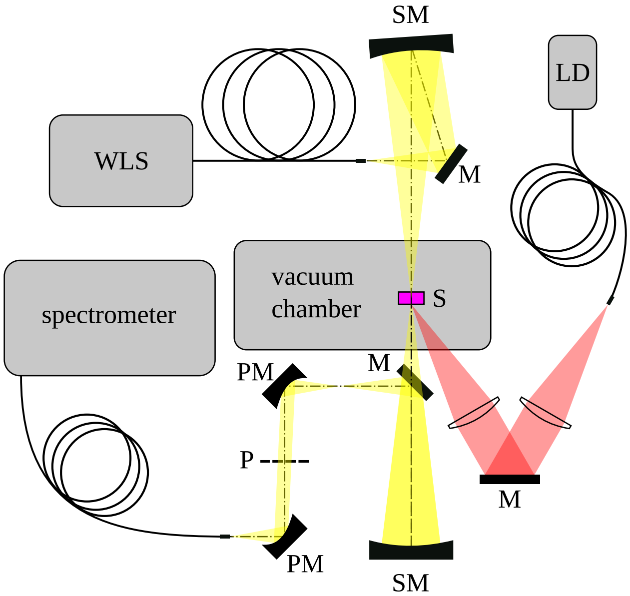

Figure 1: Schematic drawing of the measurement setup. LD... fiber coupled laser diode; M... turning mirror; P... polarizer; PM... parabolic mirror; S... sample; SM... spherical mirror; WLS... fiber coupled white light source.

The work was performed in cooperation with M. Krüger and A. Münzer from Ludwig-Maximilians University Munich. The authors further acknowledge funding through EU programs No. 739573 and 654148; Thuringian Ministry TMWWDG (2016FE9058); German Ministry BMBF (03ZIK445, 05P15SJFA1, 03Z1H531, 03VNE2068D).

References

[1] J. Körner *et al.*, Journal of the Optical Society of America B **29**, 2493 (2012).

[2] J. Körner *et al.*, Applied Physics B **116**, 75 (2014).

[3] J. Körner *et al.*, Optical Materials Express **10**, 2425 (2020).

* joerg.koerner@uni-jena.de

Kilowatt-average-power nonlinear post-compression of millijoule pulses in a gas-filled multi-pass cell

Christian Grebing[1,2], Michael Müller[1], Joachim Buldt[1], Henning Stark[1], and Jens Limpert*[1,2,3]

[1]Institute of Applied Physics, Friedrich Schiller University Jena, Albert-Einstein-Str. 6, 07745 Jena, Germany; [2]Fraunhofer Institute for Applied Optics and Precision Engineering, Albert-Einstein-Str. 7, 07745 Jena, Germany; [3]Helmholtz Institute Jena, Fröbelstieg 3, 07743 Jena, Germany

1-mJ, 31-fs pulses with an average power of 1 kW are generated by post-compression of 200-fs pulses from a high-power Yb:fiber laser system in an argon-filled multi-pass cell with an overall compression efficiency of 96%. We also analyze the output beam, revealing essentially no spatiospectral couplings or beam quality loss.

Intense sub-100 fs laser pulses can be used to drive unique secondary sources either by nonlinear frequency conversion into the Terahertz [1] and X-ray regime [2] or by acceleration of particles in a plasma [3]. Increasing the average power of the driving laser source increases the photon/particle flux of the secondary source and, thus, reduces acquisition times and improves signal-to-noise ratios in a plethora of applications. However, the pulse duration of kilowatt ultrafast laser is currently limited to >100 fs [4], which calls for efficient post compression shemes.

In this report, we present the combination of a millijoule-energy high-average power Yb:fiber laser source with a highly efficient multi-pass cell (MPC) compression stage demonstrating a close-to lossless peak power boost from 4.5 GW to 24 GW resulting in a compressed pulse duration of 31-fs [5]. The experimental results represent the highest average power of sub-100 fs pulses generated to date.

The laser source for the pulse compression is a coherently combined high-power Yb:fiber chirped-pulse amplifier system [4]. The system provides pulses with ~1-mJ pulse energy and a pulse duration of 200 fs at a repetition rate of 1 MHz resulting in an average power of ~1 kW.

The MPC itself consists of two concave mirrors with a radius-of-curvature of 0.6 m and 75 mm diameter placed in a low-pressure chamber filled with 700 mbar of argon, which acts as a nonlinear medium for self-phase modulation (SPM) induced spectral broadening. The MPC mirror distance is adjusted to 1183 mm resulting in 26 focal passes. The chirp after the MPC is removed with a chirped-mirror compressor providing a group delay dispersion (GDD) of -1923 fs^2.

The compressed output power is 1004 W when feeding 1045 W into the compression chamber resulting in an excellent combined transmission of MPC and chirped-mirror compressor of 96%, which is not achievable with alternative compression approaches.

The measured broadened spectrum behind the compression chamber is shown in the upper panel of Fig. 1 exhibiting a 20-dB-width of ~120 nm. The spectrum reveals symmetric side-wings indicating SPM dominated broadening.

*jens.limpert@uni-jena.de

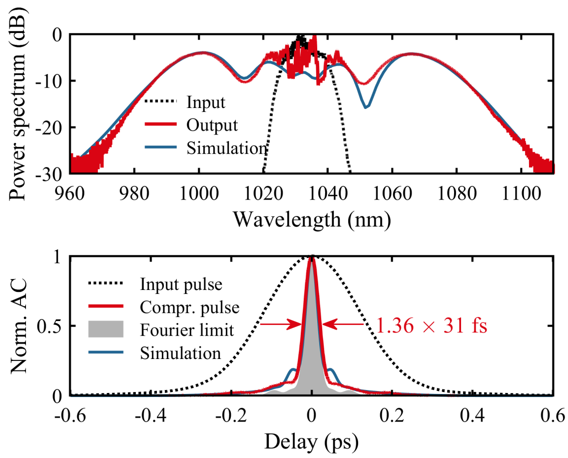

Figure 1: Upper panel: measured input (dotted line) and compressed output spectrum (measurement: blue line, simulation: red line). Lower panel: comparison of normalized autocorrelation traces of the compressed pulse (measurement: blue line, simulation: red line), input pulse (dotted line), and Fourier-limited pulse (gray area). The latter is derived from the output spectrum in the upper panel.

The compressed pulse duration is inferred from a second-order intensity autocorrelation measurement to 31 fs and is close to the theoretical limit (see Fig. 1, lower panel).

Finally, the quality of the compressed output beam was characterized in terms of the beam propagation factor M^2 and of the spatio-spectral homogeneity revealing essentially no loss in beam quality or homogeneity due to compression. Especially SPM induced spectral broadening in principle leads to a strong spatial dependence of the broadening. The characterization shows that this unwanted effect is fully compensated by the MPC topology. Hence, the setup realizes a close-to lossless compression at highest average power with excellent beam quality and homogeneity.

The authors acknowledge funding from the ERC (Grant Agreement No.835306), the Fraunhofer CAPS, and the BMBF (01DR20009A).

References

[1] P. L. Kramer *et al.*, Opt. Exp. **28**, 16951 (2020).

[2] R. Schoenlein *et al.*, Philos. Trans. R. Soc. A **377**, 20180384 (2019).

[3] S. P. D. Mangles *et al.*, Nature **431**, 535 (2004).

[4] H. Stark *et al.*, Opt. Lett. **46**, 969 (2021).

[5] C. Grebing *et al.*, Opt. Lett. **45**, 6250 (2020).

Ultra-short-pulse high-average-power Megahertz-repetition-rate coherent extreme-ultraviolet light source

Robert Klas*[1,2], Alexander Kirsche[1,2], Martin Gebhardt[1,2], Joachim Buldt[2], Henning Stark[2], Steffen Hädrich[3], Jan Rothhardt[1,2,4], and Jens Limpert[1,2,4]

[1]Helmholtz Institute Jena, Fröbelstieg 3, 07743 Jena, Germany; [2]Institute of Applied Physics, Abbe Center of Photonics, Friedrich-Schiller-University Jena, Albert-Einstein-Str. 15, 07745 Jena, Germany; [3]Active Fiber Systems GmbH, Ernst-Ruska-Ring 17, 07745 Jena, Germany; [4]Fraunhofer Institute for Applied Optics and Precision Engineering, Albert-Einstein-Str. 7, 07745 Jena, Germany

High harmonic generation (HHG), related phenomena and applications are intensively studied since more than three decades [1]. Nevertheless, the development of HHG sources to new record performance levels is still ongoing, enabling novel applications in fields as diverse as physics, biology, chemistry and material sciences. In this contribution a state of the art HHG based XUV source is presented, delivering a record high average power of 12.9 mW in a single harmonic line at 26.5 eV [2], surpassing the average power of previously demonstrated sources by an order of magnitude.

HHG is a highly nonlinear process, depending strongly on the driving laser parameters [1], particularly on the pulse duration and central wavelength. They can be optimized to maximize the efficiency of the HHG process, while highest efficiencies can be expected for shortest driving wavelength and pulse duration (supporting the particular cutoff energy) [1]. This is due to a higher applicable intensity for phase matched HHG using short pulse durations [1], in combination with the scaling of the single atom response with intensity (I^6) and central wavelength (λ^{-6}) [1]. Indeed, by employing driving lasers with short wavelength (<500 nm), but rather long pulse durations of more than 80 fs, high average power HHG sources exceeding the mW level have already been demonstrated [3].

Additional up-scaling of the XUV average power can be achieved by increasing the fundamental average power or by recycling the unconverted fundamental light in enhancement cavities [4].

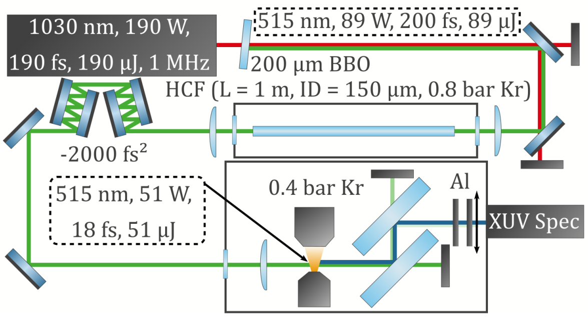

Figure 1: Experimental setup for the compression and subsequent HHG [2]. (HCF: Hollow Core Fiber, L: length, ID: inner diameter)

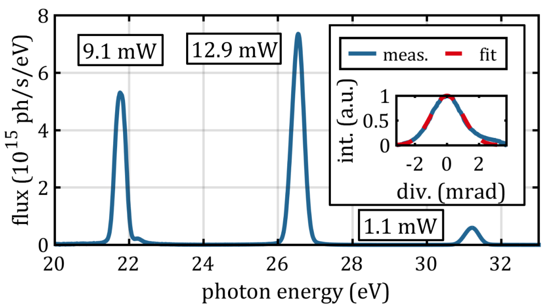

Figure 2: Optimized HHG spectrum using krypton with the corresponding average power in each harmonic line, as well as a spatial lineout of the XUV beam (shown in the inset) [2].

This work demonstrates a significant increase in in average power from table-top HHG based XUV sources [2]. This is achieved by phase matched HHG of a frequency doubled and post compressed Yb-fiber laser, which delivers a unique combination of short wavelength (515 nm) and short pulse duration (18.6 fs) at a record high average power of 51 W (Fig. 1). This new class of driving laser enables an exceptional high conversion efficiency, while the average power boosts the available photon flux to unprecedented power levels (Fig. 2). Furthermore, the measured XUV spectrum supports a Fourier limited pulse duration of sub-6 fs, which is supported by additional simulations [2].

In conclusion a new class of XUV light source is demonstrated, opening up new possibilities in the growing field of applications, such as coherent diffractive imaging of ultrafast dynamics [5] and XUV-pump XUV-probe experiments [6].

This work was supported by CAPS, ECRAPS, APPA R&D (13N12082), TMBWK (501100004404, 2017 FGR 0076), TAB (2015FGR0094), ExNet-0019-Phase 2-3.

References

[1] Z. Chang, Fundamentals of Attosecond Optics, (2016).

[2] R. Klas *et al.*, PhotoniX **2**, 4 (2021).

[3] A. Comby *et al.*, Opt. Express **27**, 20383 (2019).

[4] G. Porat *et al.*, Nat. Photonics **12**, 387 (2018).

[5] O. Kfir *et al.*, Sci. Adv. **3**, eaao4641 (2017).

[6] J. Rothhardt *et al.*, X-Ray Spectrom. **49** (2020).

*robert.klas@uni-jena.de

Water window high harmonic generation at 100 kHz repetition rate

M. Gebhardt*[1,2], T. Heuermann[1,2], R. Klas[1,2], C. Liu[1,2], A. Kirsche[1,2], M. Lenski[1], Z. Wang[1], C. Gaida[2,5], J. E. Antonio-Lopez[3], A. Schülzgen[3], R. Amezcua-Correa[3], J. Rothhardt[1,2,4], and J. Limpert[1,2,4]

[1]Helmholtz Institute Jena, Fröbelstieg 3, 07743 Jena, Germany; [2]Institute of Applied Physics, Abbe Center of Photonics, Friedrich-Schiller-Universität Jena, Albert-Einstein-Str. 15, 07745 Jena, Germany; [3]CREOL, College of Optics and Photonics, University of Central Florida, Orlando, FL 32816, USA; [4]Fraunhofer Institute for Applied Optics and Precision Engineering, Albert-Einstein-Str. 7, 07745 Jena, Germany; [5]Now with: Active Fiber Systems GmbH, Ernst-Ruska-Ring 17, 07745, Jena, Germany

Ultrafast coherent light sources, providing high photon flux at high repetition rates in the soft X-ray (SXR) spectral region are interesting for numerous applications in fundamental and life science [1]. Herein, we demonstrate a compact, fiber-based SXR source based on nonlinear pulse self-compression and high harmonic generation (HHG) in a single helium-filled antiresonant hollow-core fiber (ARHCF). Utilizing a state-of-the-art thulium-doped fiber laser as the driver, we have generated $> 10^6$ ph s^{-1} eV^{-1} at the carbon K-edge.

Most recently, there has been a significant push toward scaling the repetition rates of laser-driven SXR sources in the water window to enable faster data acquisition, space-charge-reduced photoelectron spectroscopy or coincidence detection. Here, we present an approach to SXR HHG that is based on nonlinear pulse self-compression and HHG in the same helium gas-filled ARHCF [2]. Because of the intensity enhancement resulting from temporal pulse self-compression along the waveguide, the high harmonics are generated just before the fiber output. This way, the SXR radiation can be retrieved directly from the hollow wave-guide (Fig. 1). The experiments are driven by moderate-energy, multi-cycle laser pulses, which facilitates repetition rate scaling. We couple 100 fs-, 250 μJ-pulses centered around 1.9 μm wavelength at 98 kHz repetition rate to the ARHCF input. Resulting from the quadratic wavelength dependence of the driving laser field's ponderomotive potential, the phase-matched photon energy cut-off is beyond the carbon K-edge (284 eV, see Fig. 2). To the best of our knowledge, the generated photon flux is the highest reported to date at 300 eV and a laser repetition rate >1 kHz. In future work, the efficiency and yield in the water window will be further optimized, and the source will be employed for spectroscopy as well as imaging of organic samples at high repetition rate.

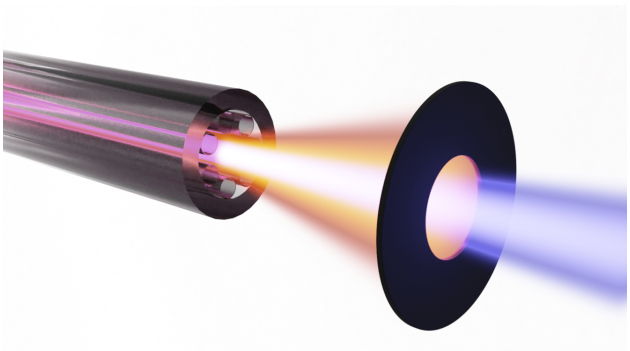

Figure 1: Principal setup of the nonlinear self-compression and high-order harmonic generation.

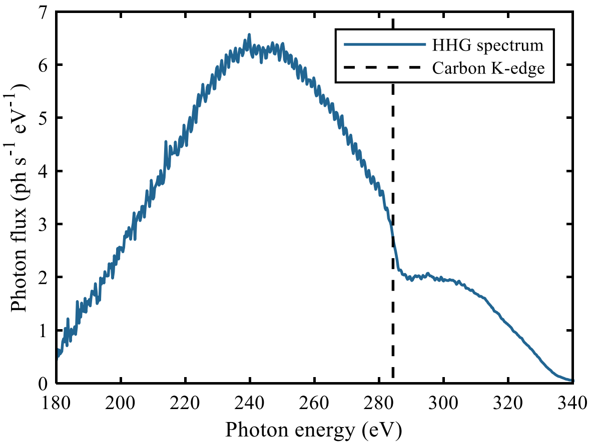

Figure 2: Spectrum of the coherent SXR source with visible absorption feature at the carbon K-edge.

The authors acknowledge funding from the Helmholtz-Institute Jena, the European Research Council (grant 835306, SALT) and the Fraunhofer Cluster of Excellence Advanced Photon Sources.

References

[1] L. Young *et al.*, J. Phys. B At. Mol. Opt. Phys. **51**, 032003 (2018).

[2] M. Gebhardt *et al.*, Light Sci. Appl. **10**, 36 (2021).

*martin.gebhardt@uni-jena.de

Differential pumping unit for window-less coupling of laser beams to ultra-high vacuum

Vinzenz Hilbert[1], Philipp Gierschke[3], Maxim Tschernajew[3], Jens Limpert[1,2,3], and Jan Rothhardt*[1,2,3]

[1]Helmholtz Institute Jena, Fröbelstieg 3, 07743 Jena, Germany; [2]Institute of Applied Physics, Friedrich-Schiller-University Jena, 07745 Jena, Germany; [3]Fraunhofer Institute for Applied Optics and Precision Engineering, 07745 Jena, Germany

Coupling extreme ultraviolet violet (XUV) radiation from high harmonic laser sources to ultra-high vacuum (UHV) setups is challenging. For this purpose, a dedicated differential pumping unit has been developed [1]. It can provide a pressure gradient of up to six orders of magnitude and a gas flux gradient of up to five orders of magnitude. Moreover, the lowest total pressure reaches deep into the 10^{-11} mbar range. Its window-less design makes it a versatile tool for loss-less XUV-beam coupling to storage rings, ion traps and cryogenic detectors.

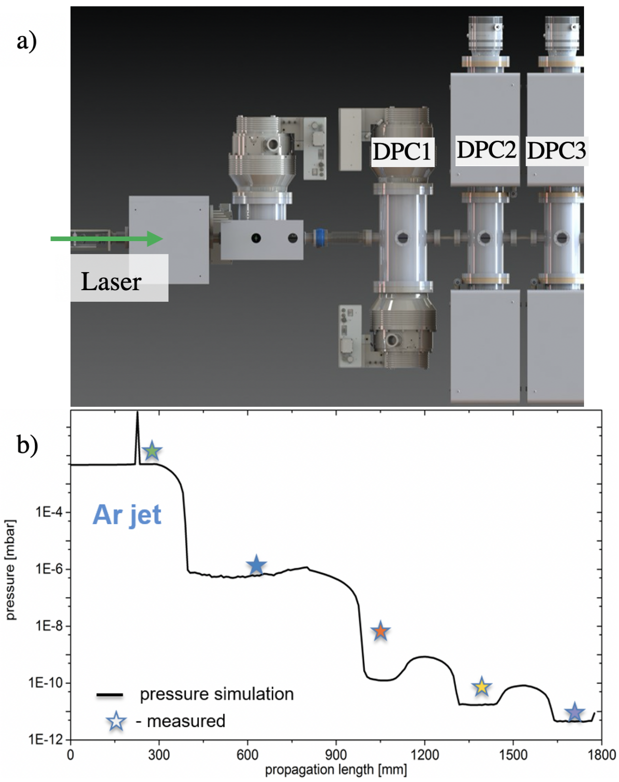

Figure 1: a) Drawing of the unit with the Differential Pumping Chambers (DPC) 1, 2, 3 b): development of the pressure along the DPU. Stars represent measured pressure in the different vacuum chambers

The application of XUV high-harmonic sources (HHG) [2] to ion storage rings opens up the promising field of laser spectroscopy and lifetime measurements of excited states of highly charged ions [3,4]. Since the transmission of any material is very low in the XUV, the high order harmonics have to be transmitted window-less from the source point to the target in the storage ring. Since high-order harmonics are generated in noble gas targets, an unwanted but significant noble gas flow towards the storage ring will be generated, resulting in a drastically reduced lifetime of the ions in the ring. We have developed a three stage differential pumping system (see Fig. 1a) which efficiently reduces the noble gas partial pressure from the harmonics source towards the UHV-storage ring. The first differential pumping chamber (DPC 1) is equipped with two 1300 l/s (N_2) turbo pumps. The second and third DPC are of similar structure. Since the required pressure is lower than the pressure limit of turbo-molecular pumps ($\sim 10^{-10}$ mbar), two ion getter pumps (IGP) are utilized per chamber, each providing 500 l/s nominal pumping speed for N_2. Fig. 1b) shows the evolution of the pressure along the DPU from the left to the right, both measured and simulated using a Monte Carlo method. Starting from an Ar-jet at 2.4 bar which is necessary for the HHG each pumping chamber reduces the pressure by more than one order of magnitude. Finally a pressure of 3×10^{-11} mbar is reached, whereas the Ar-partial pressure is even 5×10^{-12} mbar. The clear aperture of 10 mm, the compact total length of 1.7 m and the portability makes this DPU a versatile tool for any window-less UHV coupling application, particularly for loss-less XUV-beam coupling to storage rings, ion traps and cryogenic detectors.

The authors acknowledge funding from the Federal State of Thuringia (2015 FGR 0094), the European Social Fund (ESF), the Federal Ministry of Education and Research (BMBF) grant number 05P15SJFFA and the Fraunhofer Cluster of Excellence Advanced Photon Sources.

References

[1] M. Tschernajew, P. Gierschke, H. Lin, V. Hilbert, J. Kurdal, A. Stancalie, J. Limpert, J. Rothhardt, Vacuum **178**, 109443 (2020).

[2] V. Hilbert, M. Tschernajew, R. Klas, J. Limpert, J. Rothhardt, AIP Advances **10**, 045227 (2020).

[3] J. Rothhardt, M. Bilal, R. Beerwerth, A. V. Volotka, V. Hilbert, Th. Stöhlker, S. Fritzsche, and J. Limpert, X-Ray Spectrom. **49**, 165 (2020).

[4] M. Lestinsky *et al.*, Eur. Phys. J. Spec. Top. **225**, 797 (2016).

* j.rothhardt@hi-jena.gsi.de

Single-shot characterization of strongly focused coherent XUV beams

W. Eschen*[1,2], G. Tadesse[1,2], Y. Peng[2], M. Steinert[1], T. Pertsch[1,3], J. Limpert[1,2,3], and J. Rothhardt[1]

[1]Helmholtz Institute Jena, Germany; [2]Institute of Applied Physics, FSU Jena,Germany; [3]Fraunhofer IOF Jena, Germany

Measuring the wavefront in the XUV and soft X-ray region is challenging due to the lack of refracting optics in this spectral range. We report on a single-shot-capable method for characterizing focused coherent beams which relies on an amplitude mask in combination with an iterative phase retrieval algorithm. The amplitude and phase profile of a focused beam is reconstructed from a single measured far-field diffraction pattern. Our method is demonstrated in a proof-of-principle experiment using a wavelength of 13.5 nm achieving an RMS phase error of less than λ/70.

To characterize focused beams in the XUV or soft X-ray region, multi-shot techniques such as ptychography are often used [1]. These techniques require scanning, multiple acquisitions, and assume that the beam does not change during the scan.

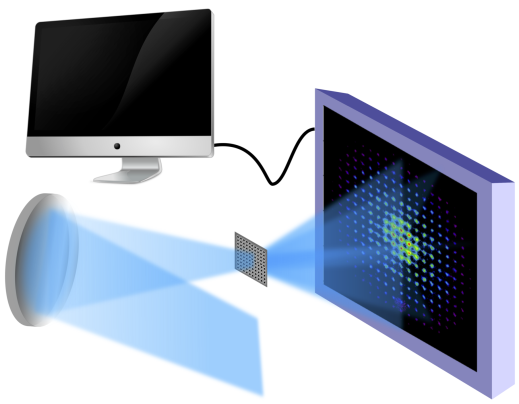

Figure 1: Schematic representation of the setup. Reproduced from [3].

We have developed a technique that can measure the amplitude and phase of a beam using only a single measured diffraction pattern. For this purpose, an amplitude-only mask, consisting of an array of small holes (see Fig. 2 a)) is placed directly in the focused beam (Fig. 1). The far-field diffraction of the transmitted beam is measured by a detector. In the next step, a phase-retrieval algorithm is used to reconstruct the electric field, which is transmitted through the small holes. Since a binary mask is used, the final illuminating beam can be interpolated from the retrieved electric field of the sub-apertures, which are arranged regularly. The feasibility of our method is demonstrated in a proof-of-principle experiment using an HHG source operating at a wavelength of 13.5 nm. A pinhole with a diameter of 2.7 µm was placed in the focus of the HHG beam to create a stable and well-defined illumination. The wavefront sensor mask was placed 500 µm behind the pinhole and its diffraction pattern was measured. The reconstructed and interpolated phase, which corresponds to the wavefront, is shown in Fig. 2 b) and shows, as expected, a spherical wavefront. To quantify the accuracy of our wavefront sensor we simulated the expected wavefront behind the pinhole. The RMS value of the difference between measurement and simulation was better than λ/70. The reconstruction of the wavefront using an iterative phase-retrieval algorithm took 20 s. Since real-time beam characterization and the alignment of complex optical systems require fast reconstructions we developed an artificial neural network to reconstruct the wavefront from the measured diffraction [2]. The use of the neural network allowed to push the reconstruction time from 20 s to a few milliseconds which enables real-time wavefront characterization. Hence, the developed wavefront sensor enables real-time, single-shot measurements of the wavefront of coherent, focused beams in the XUV to the soft X-ray range, which will enable alignment of complex optics, real time feedback of adaptive optics and single-shot wavefront measurements of HHG and free-electron laser beams. More details on the wavefront sensor are given in [3].

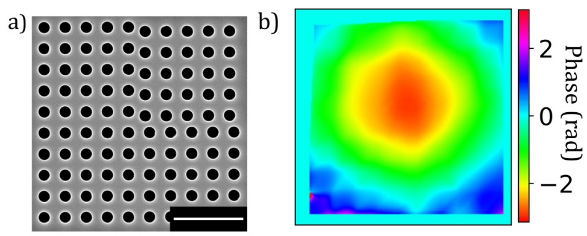

Figure 2: (a) Mask used for the experiment presented here. (b) Reconstructed wavefront of a pinhole placed 500 µm in front of the wavefront sensor. Reproduced from [3].

The authors acknowledge funding from the Federal State of Thuringia (2017 FGR 0076) and the European Social Fund (ESF).

References

[1] P. Thibault *et al.*, Ultramicroscopy **109**, 338 (2009).

[2] J. White *et al.*, Opt. Express **29**, 9283 (2021).

[3] W. Eschen *et al.*, Opt. Lett. **45**, 4798 (2020)

*wilhelm.eschen@uni-jena.de

Compact and Robust Ultra-Low Timing Jitter Fiber Laser Oscillator

Y. Ma*[1], S. H. Salman[1,2], C. Li[1], C. Mahnke[1], Y. Hua[1], S. Droste[1], J. Fellinger[2], A. S. Mayer[2], O. H. Heckl[2], C. M. Heyl[1,2], and I. Hartl†[1]

[1]Deutsches Elektronen Synchroton DESY; [2]Helmholtz Institute Jena, Germany; [3]University of Vienna

We developed an all-PM Yb:fiber integrated femtosecond NALM oscillator with sub-femtosecond timing jitter. The output is centered at 1030 nm with 51 mW average power and 19 nm bandwidth, compressible to 88 fs. The integrated design provides excellent stability and robustness, ideally suited for seeding high power laser systems in applications which require both high availability and low timing jitter.

Today, most ultrafast high-power laser applications are powered by laser systems based on Ytterbium (Yb) doped gain materials. Those laser systems require robust and stable seed oscillators, generating the ultrafast pulse-train to be amplified. Here fiber-oscillators provide robustness, reliability and cost efficiency. However, timing critical laser systems often rely on solid-state lasers, since their higher cavity Q fundamentally allows lower timing jitter.

To overcome the above limitations, we developed a sub-fs timing jitter mode locked Yb:fiber laser based on a nonlinear amplifying loop mirror (NALM) [1-3] for seeding timing critical high power laser systems for example in free electron laser (FEL) facilities [4]. The optical set-up is shown in Fig. 1. The NALM is shown on the right-hand side of the 50/50 coupler and acts as pulse-forming saturable absorber: Pulses propagate in the loop both clockwise and counterclockwise but experience a different intensity dependent phase shift, due to the asymmetric placement of the gain fiber interfering at the coupler after one round-trip. The non-reciprocal phase bias consisting of Faraday rotator and waveplate is set such that high intensity pulses are coupled towards the output arm, where a chirped fiber Bragg grating acts as cavity end-mirror and dispersion compensating element. Timing jitter measurements

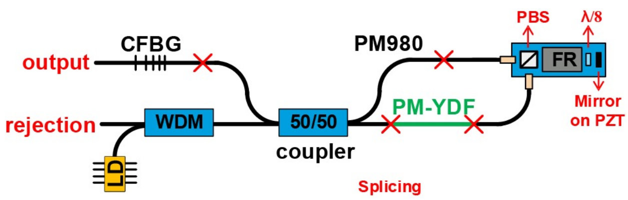

Figure 1: Experimental set-up. CFBG: chirped fiber Bragg grating; PM-YDF, PM980: Yb-doped and undoped polarization maintaining single mode fiber; PBS: polarizing beam splitter; LD: laser diode; WDM: wavelength-division multiplexer. FR: Faraday rotator; λ/8: waveplate; PZT: piezo actuator.

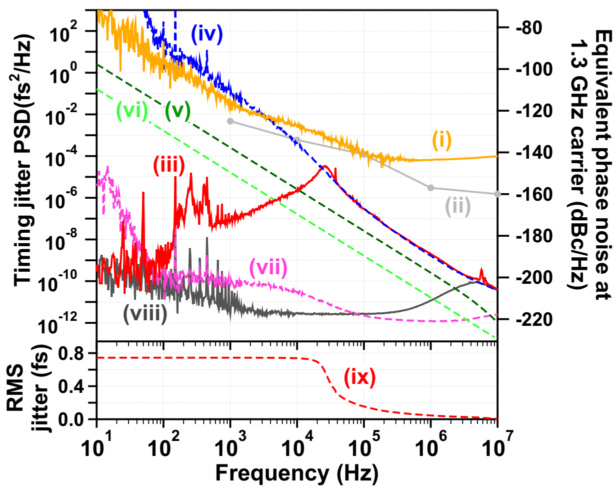

Figure 2: (i) Measured phase noise PSD (RF measurement); (ii) Instrument sensitivity (Agilent E5052B) (iii) Measured timing jitter PSD (optical cross correlator) Note: feedback loop with 25 kHz servo bandwidth was active; (iv) – (vii) Calculated timing jitter PSD contributions according to theory: (iv) RIN via self-steepening, (v) Gordon-Haus jitter, (vi) ASE noise (vii) RIN via Kramers-Kronig relations, (viii) Noise floor of the BPD; (ix) Integrated RMS jitter of curve (iii).

are shown in Fig. 2. Since the RF measurement was limited by the instrument noise floor, we performed an optical measurement by cross-correlating two identical oscillators with a slight repetition frequency offset, stabilized by a 25 kHz bandwidth servo loop. The integrated timing jitter was measured to 0.7 fs RMS [25 kHz to 5 MHz] and to 0.8 fs down to 10Hz, including the stabilization loop.

With this excellent performance, the laser meets all requirements for seeding timing critical high power, high energy laser systems at FEL facilities. We additionally demonstrated CEP stable operation, which opens up further applications such as frequency comb spectroscopy.

References

[1] M. E. Fermann *et al.*, Opt. Lett. **15**, 752 (1990).

[2] N. Kuse *et al.*, Opt. Expr. **24**, 3095 (2016).

[3] W. Hänsel *et al.*, Appl. Phys. B **123**, 41 (2017).

[4] Y. Ma *et al.*, J. Light. Technol., early access https://doi.org/10.1109/JLT.2021.3070208.

* yuxuan.ma@desy.de
† ingmar.hartl@desy.de

Generation of laser beams with orbital angular momentum @ JETi200

A. Sävert*[1,2], G. Schäfer[1], A. Seidel[2], S. Kuschel[3], and M. Zepf[1,2]

[1]Helmholtz Institute Jena, Fröbelstieg 3, 07743 Jena, Germany; [2]Institute of Optics and Quantum Electronics, Max-Wien Platz 1, 07743 Jena, Germany; [3]University of Hamburg, Luruper Chaussee 149, 22761 Hamburg, Germany

The high intensity laser facility JETi200 at the HI Jena provides ultra-bright laser pulses with a peak power in excess of 200 TW for studying laser-plasma interactions. Using phase masks allows shaping the intensity distribution in the focal plane and making new experiments feasible.

In the last years, JETi200 has been used in the field of surface high harmonic generation, laser driven ion and electron acceleration. For these kind of experiments either the highest intensity (the former) or a high intensity over a long propagation length (the latter) is desired. The focal spot hereby exhibits typically a Gaussian intensity distribution.

Recent PIC-simulations have suggested that a Gaussian focal spot is not optimal for all kind of experiments. Using a top hat like profile can reduce the growth of instabilities in overdense plasmas. In laser wake field acceleration experiments using Gaussian focal spots, the ponderomotive force of the laser pulse acts as a snow plow shoveling electrons away from the optical axis. Here, a donut shaped focal spot with an intensity depression in the center spot, see Figure 1, can generate an electron density spike on axis.

The expanded plasma structure allows accelerating electrons in a 2-dimensional manner instead of the usual 1-dimensional setup, which should increase the total accelerated charge. At the same time the acceleration of positrons is feasible.

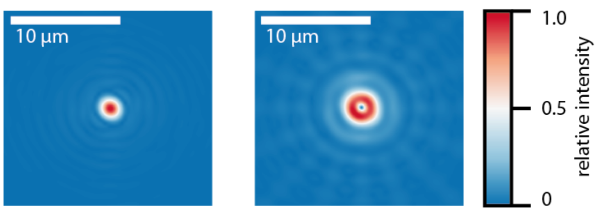

Figure 1: Simulated focal spot without (left) and with (right) phase mask.

These kind of donut shaped beams can be generated by applying a spiral phase plate in the near field of the laser pulse. Here, we have used such a plate with a topological charge of 1. The plate was manufactured using 16 slices with an equidistant stepwise increase of the phase up to 2π. The simulated far field profile in Figure1 considered this, resulting in the star like modulation in the outer parts. The plate was installed after the final power amplifier of the JETi200 laser and in front of the last expansion telescope.

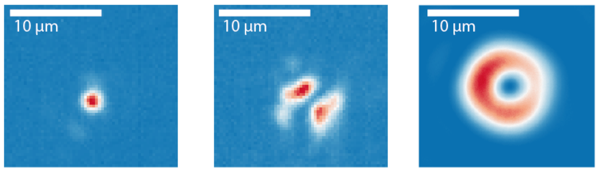

Figure 2: Measured focal spot in Target Area II using an F/1.5 off-axis parabolic mirror. Without (left) and with (middle) phase mask. Apodised beam with phase mask (right). All images are normalized.

The focal spot was recorded using the experimental diagnostics in Target Area II. There an F/1.5 off-axis parabolic mirror was used to focus the beam to a spot with a diameter of 1.5 µm (FWHM), see Figure 2. The nearly diffraction limited focal spot was optimized using a wave front sensor (phasics) in combination with a deformable mirror. After installing the spiral plate, the focal spot was imaged with the same diagnostic. Its size has increased and the profile is strongly modulated. A minor movement of the phase plate in the laser chain did not change the outcome. At this point, it is not clear whether the origin of the distorted focal spot results from residual phase aberration on the laser pulse itself or on the manufacturing tolerances of the plate. However, apodising the laser pulse to about one third of its diameter results in a more distinct shape, see Figure 2 right panel. The peak intensity is hereby reduced by more than one order of magnitude.

In a next step, a beam shaping device consisting of an amplitude mask and a spatial filter will be installed at the JETi200 laser system. This would allow generating a more top hat like profile, separating the beam annularly or vertically. For pump-probe experiments, beamsplitters are used routinely to split the beam into two parts. This becomes an issue for high intensity laser pulses, as the thickness required for such large beam optics would contribute to a large B-integral. Hence, the focusability and pulse compression gets worse. Using such shaped beams in combination with D-shaped mirrors or mirrors, which have a hole cut into; two beam can be extracted for pump probe experiments. Further, one of the two beams can be shifted in frequency by means of a frequency doubling crystal and two-color experiments are feasible.

* a.saevert@hi-jena.gsi.de

Stability of JETI200 laser

X. Huang[1,2], A. Sävert[1], B. Heinemann[2], and M. Zepf*[1]
[1]Helmholtz Institute Jena, Fröbelstieg 3, 07743 Jena, Germany; [2]DESY, 22607 Hamburg, Germany

The LUXE (Laser Und XFEL Experiment) project aims to measure processes in the strong-field quantum electrodynamics regime with high precision by colliding electrons or a high-energy photon beam with high-power, tightly focused laser beam at a repetition rate of 1 Hz. Simulations [1] predict that the probability of pair production responds highly non-linearly to the laser strength parameter. Consequently, small variations in the laser intensity lead to significant variations in the experimental observables. The required precision will be achieved by intensity tagging though precise measurements on the laser intensity of each shot. We present first results of a laser diagnostic system with an ultimate aim to monitor the shot-to-shot fluctuations with precision below 1 %.

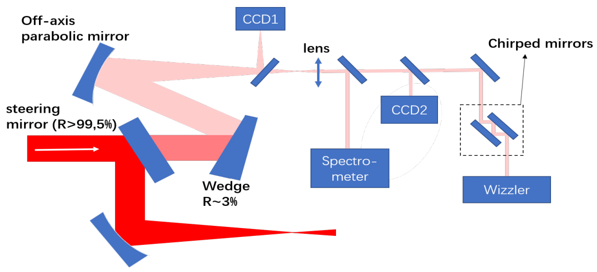

Figure 1: Layout of laser diagnostic system.

Temperature drift, air currents and mechanical vibrations cause spectral and temporal phase fluctuations, which result in the variations of pulse duration and focus radius and therefore ultimately in the focused laser intensity. The aim is to develop a laser diagnostic, capable of precised measuring the relative variation of intensity on a shot-by-shot basis and tagging the experimental data to allow precision measurements. Initial experiments were performed on JETI200 laser system. This laser is designed to have an on-target energy of > 5 J and a pulse duration of 17 fs at its best performance, with central wavelength 800 nm. Its peak power can exceed 200 TW.

As shown in Figure 1, the diagnostic system uses the leak light transmitted through a steering mirror. The light is further attenuated by a wedge with reflection rate approximately 3 %, and then focused by the off-axis parabola with focal length 600 mm. CCD camera 1 is to measure the focus area, A. Pulse energy, E, can be calculated from the results obtained by CCD 2 and the spectrometer. Finally, before the Wizzler which measures pulse duration, t, a pair

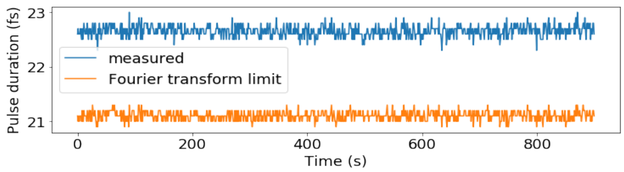

Figure 2: Pulse duration over a period of 15 minutes, with mean value 22.6 fs and RMS 0.4 %.

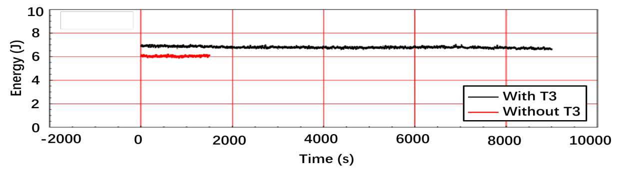

Figure 3: Pulse energy measured during 30 minutes, with mean value 6.8 J (with Titan3) and RMS 1.1 %.

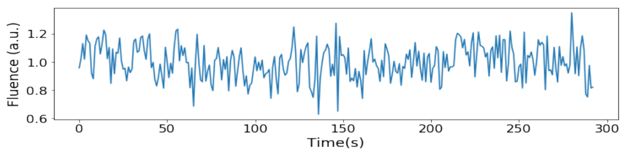

Figure 4: Fluence of focus center, with RMS 10%.

of chirped mirrors are applied to compensate for the group delay dispersion. The laser intensity, I, can be obtained according to the following equation

$$I = \frac{E}{tA}\,. \tag{1}$$

The laser was operated at a repetition rate of 1 Hz. The RMS variation of the pulse duration is 0.4 %, as in Fig. 2 and 1.1 % for energy in Fig. 3. As shown in Fig. 4, the stability of the counts of focal maximum detected on the pixels of CCD 1. fluctuates by as much as 10 %, suggesting that phase-noise, rather than energy fluctuations are the dominant source of intensity modulations. The role of phase fluctuations on the focused pulse durations will be evaluated in future.

In conclusion first tests of a system capable of monitoring fluctuations have been performed, with future work focused on detailed focal spot reconstruction using INSIGHT [2] and shot to shot pulse duration measurements.

References

[1] LUXE CDR, arXiv:2102.02032 [hep-ex].

[2] A. Borot and F. Quéré, Opt. Express **26**, 26444 (2018).

*m.zepf@uni-jena.de

LASER PARTICLE ACCELERATION

Pulse front tilt in ultrashort high-intensity laser pulses

C. Zepter*[1,2], A. Sävert[1,2], and M. C. Kaluza[1,2]

[1]Helmholtz Institute Jena, Fröbelstieg 3, 07743 Jena, Germany; [2]Institute of Optics and Quantum Electronics, Max-Wien-Platz 1, 07743 Jena, Germany

We report on the pulse front tilt (PFT) of the focused laser pulse due to spatio-temporal couplings in a laser beam. Besides the well established relation between angular dispersion and PFT the relation between PFT and spatial and temporal chirp is examined.

Today's high intensity laser systems are based on the principle of chirped-pulse amplification [1], where diffraction gratings are used to stretch and compress the pulse prior to and after amplification, respectively. Slight misalignments of the diffraction gratings lead to angular dispersion being imprinted on the pulse's near field profile which subsequently results in a pulse front tilt (PFT). Here the intensity envelope of the pulse is tilted with respect to the phase fronts being perpendicular to the pulse's propagation direction. The focusing of a laser beam with angular dispersion in the near field leads to a spatially dispersed pulse in the focal plane showing no PFT there and changing tilt direction around this plane (cf. Fig. 1(b)). However, it is also possible to generate PFT by applying GDD to a spatially dispersed pulse, independent from the PFT generated by angular dispersion [2]. To reach a precise understanding of the behavior of a pulse's spatio-temporal intensity envelope it is necessary to take into account all the pulse's spatio-temporal couplings (STCs) which are its inseperable chromatic aberrations [3].

We consider a Gaussian beam propagating along the z-axis with linear spatial chirp $\xi_0 = \mathrm{d}x_0/\mathrm{d}\omega$, linear angular dispersion $\beta_0 = \mathrm{d}\Theta_0/\mathrm{d}\omega$ and GDD φ. Here x_0 is the transverse position of a ω-component of the beam, where ω is the offset to the center angular frequency (ω_0), and Θ_0 is the propagation angle of this component. The electric field $E(x, z, \omega)$ of this Gaussian beam at its waist at $z = 0$ can be expressed as [4]

$$\begin{aligned} E(x,0,\omega) &= E_0 \exp\left(\frac{-\omega^2\tau_0^2}{4}\right)\exp\left(-i\frac{\varphi}{2}\omega^2\right) \\ &\quad \times \exp\left(\frac{-ik_0(x-\xi_0\omega)^2}{2iz_R}\right) \\ &\quad \times \exp\left(-ik_0\beta_0\omega x\right) \qquad (1) \end{aligned}$$

where k_0 is the nominal wave number, τ_0 is the rms-pulse duration and $z_R = \pi w_0^2/\lambda_0$ is the Rayleigh length with w_0 being the beam waist of the undistorted beam. Throughout the analysis we concentrated on distortions in one transverse direction only (i.e. the x-direction) thus neglecting any distortions of the laser beam in y-direction. For propagating the beam to an arbitrary position z in space we use the Huygens Fresnel integral in one dimension and

* carola.zepter@uni-jena.de

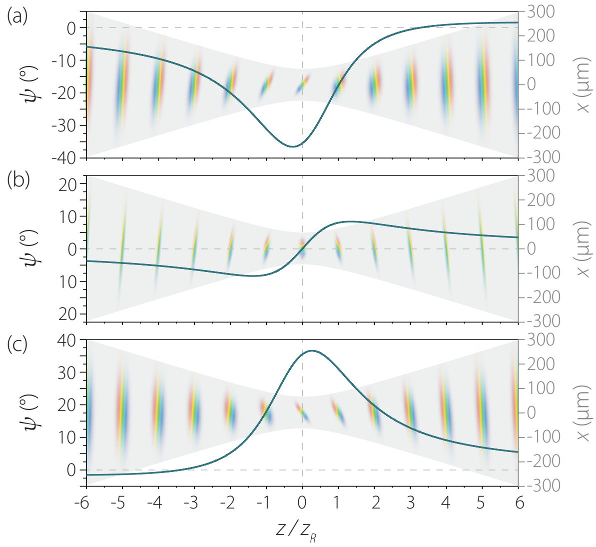

Figure 1: PFT-angle ψ as a function of z normalized to z_R, with $\xi_0 = 0.6\,\mu\mathrm{m/nm}$, $\beta_0 = -4.56\,\mu\mathrm{rad/nm}$, $\tau_0 = 17\,\mathrm{fs}$, $w_0 = 26\,\mu\mathrm{m}$ and $z_R = 1.2\,\mathrm{mm}$ for (a) GDD = +1050 fs^2, (b) GDD = 0 fs^2 and (c) GDD = -1050 fs^2. Shown in gray are the caustic of the beam along with an artist's impression of the spectrally resolved shape of a pulse front in $(x - z)$-space.

perform an inverse Fourier transformation to obtain the field in the temporal domain and the PFT-angle ψ. Fig. 1 shows the result for a beam with positive spatial chirp ($\xi_0 = 0.6\,\mu\mathrm{m\,nm}^{-1} = -2 \times 10^{-19}\,\mu\mathrm{m\,rad}^{-1}\,\mathrm{s}$), i.e. the longer wavelengths are located above, the shorter ones below the laser axis and the following parameters: $\tau_0 = 17\,\mathrm{fs}$, $w_0 = 26\,\mu\mathrm{m}$, $z_R = 1.2\,\mathrm{mm}$, $\xi_0 = -2 \times 10^{-19}\,\mu\mathrm{m\,rad}^{-1}\,\mathrm{s} = 0.6\,\mu\mathrm{m\,nm}^{-1}$ and $\beta_0 = 1{,}49 \times 10^{-18}\mathrm{rad\,rad}^{-1}\,\mathrm{s} = -4.48\,\mu\mathrm{rad\,nm}^{-1}$ for (a) GDD = +1050 fs^2, (b) GDD = 0 and (c) GDD = -1050 fs^2. It can be seen, that for no temporal chirp being present, the pulse does not show any tilt in the focal plane and changes its tilt direction around the plane. With GDD being applied the pulse's behaviour changes, as a PFT is also visible directly in the focal plane. In plasma experiments, this PFT can be visible, for example, in a changed shape of the plasma wave or its development.

References

[1] D. Strickland *et al.*, Opt. Commun. **56**, 219 (1985).

[2] S. Akturk *et al.*, Opt. Express **13**, 8642 (2005).

[3] S. W. Jolly *et al.*, J. Opt. **22**, 103501 (2020).

[4] S. Akturk *et al.*, Opt. Express **12**, 4399 (2004).

Faraday measurements from laser-driven plasma waves

C. Zepter*[1,2], A. Seidel[1,2], F. P. G. Stehr[1], A. Sävert[1,2], M. Zepf[1,2], and M. C. Kaluza[1,2]

[1]Institute of Optics and Quantum Electronics, Max-Wien-Platz 1, 07743 Jena, Germany; [2]Helmholtz Institute Jena, Fröbelstieg 3, 07743 Jena, Germany

We report on the implementation and first experiments with a Faraday-rotation diagnostics at the JETi-200 laser facility at the Helmholtz Institute Jena. With this diagnostic, the magnetic fields in a wakefield accelerator are investigated via polarization rotation of a linearly polarized, ultrahort optical probe beam.

Ultrashort-optical probing is a powerful tool to investigate the dynamics of laser-wakefield accelerators. By using few-cycle optical pulses and a high resolution imaging system the evolution of the density modulations inside the plasma and therefore the evolution of the electron plasma wave can be investigated via shadowgraphy [1, 2, 3]. Additionally the magnetic fields connected to laser wakefield acceleration can be detected exploiting the Faraday effect [4]. By combining this polarimetry measurement with shadowgraphy, deeper insight into the laser-driven acceleration process can be gained.

A linearly polarized probe beam propagating inside a plasma changes its polarization state when crossing a magnetic field oriented parallel to the beam's direction of propagation. More precisely, the beam's polarization is rotated by an angle φ_{rot} as shown in the inset of Fig. 1. This angle is defined as

$$\varphi_{\text{rot}} = \frac{e}{2\,c\,m_e\,n_c}\int_l n_e\,\vec{B}_\varphi\,\mathrm{d}\vec{s} \qquad (1)$$

where $\vec{B}_\varphi$ is the azimuthal magnetic field in the laser wakefield accelerator, c, e, m_e, n_e, n_c are the vacuum speed of light, electron charge, mass, density and critical density, respectively, and $\mathrm{d}\vec{s}$ is an infinitesimal path element along the path l of the probe beam through the plasma.

The experiments were performed with the JETi-200 Ti:Sapphire laser system at the Helmholtz Institute Jena. As a probe beam the JETi200 few-cycle probe beam system was used, delivering pulses with 7 fs pulse duration, an energy of 100 µJ and a beam diameter of 5 mm. The setup is depicted in Fig. 1. The main pulse with a center wavelength of 800 nm, a FWHM pulse duration of 20 fs measured in the near field and energy of 2.8 J were focused by an f/25 off-axis parabola to a vacuum intensity of 1×10^{19} W/cm^2, accelerating electrons in a 3 mm underdense helium plasma target. The laser-plasma interaction was imaged with a high resolution imaging system in a transverse probing geometry onto two CCD-cameras each equipped with a polarizer. The polarizers are rotated away from extinction of the original polarization in opposite directions. A pixel by pixel division of the two images then yields information about the polarization rotation of the probe beam due to magnetic fields, whereas the brightness modulations due to shadowgraphy are reduced. One exemplary polarogram obtained from the two shadowgrams is shown in Fig. 2.

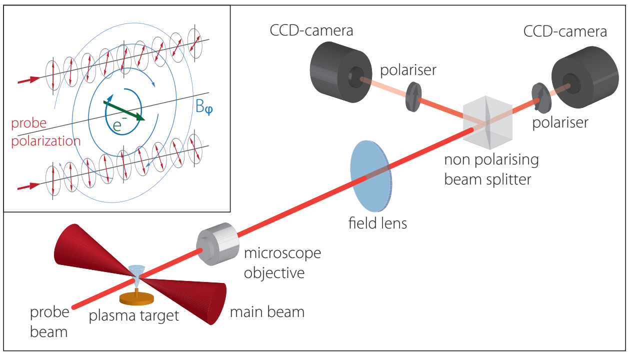

Figure 1: Schematic drawing of the Faraday rotation setup. Inset: Schematic drawing of the probe's polarization rotation due to the presence of an azimuthal magnetic field.

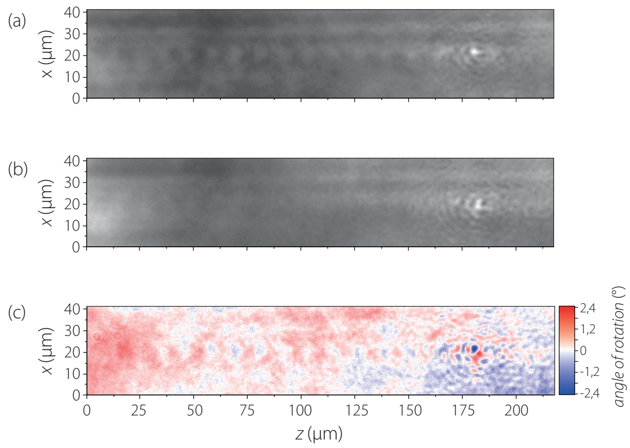

Figure 2: (c) Plot of the $\vec{B}$-field induced rotation angle of the interaction obtained by a pixel by pixel division of the two polarograms (a,b).

The images show, that at the JETi200 laser facility in-situ measurements of the plasma electron density modulations corresponding to wakefield acceleration as well as the associated magnetic fields are possible, giving direct insight into the acceleration process.

References

[1] M. C. Kaluza *et al.*, Phys. Rev. Lett. **105**, 11 (2010).

[2] A. Sävert *et al.*, Phys, Rev, Lett. **115**, 5 (2015)

[3] M. B. Schwab *et al.*, Phys. Rev. Accel. Beams **23**, 3 (2020)

[4] A. Buck *et al.*, Nat. Phys. **7**, 543 (2011)

* carola.zepter@uni-jena.de

Probing Measurements from Beam-Driven Plasma Waves

C. Zepter*[1,2], A. Seidel[1,2], A. Sävert[1,2], M. Zepf[1,2], and M. C. Kaluza[1,2]

[1]Institute of Optics and Quantum Electronics, Max-Wien-Platz 1, 07743 Jena, Germany; [2]Helmholtz Institute Jena, Fröbelstieg 3, 07743 Jena, Germany

We present the first optical probing images of electron driven plasma waves at the JETi-200 laser system. Here an electron bunch generated via laser wakefield acceleration in a first plasma target was used to drive a plasma wave in a second plasma target, being the first two stage wakefield acceleration experiment performed at the JETi-200 facility.

Over the past decades, colliders and particle acclerators have been a valuable tool to discover new physics. Radio frequency technology based electron accelerators have been able to push high-energy physics to the 100 GeV level. However, due to electrical breakdown in the accelerating structures the acceleration gradients are limited to $\lesssim$ 100 MV/m. To reach the energy frontier of particle physics - the TeV regime - long acceleration lengths of 10s of kilometers are required leading to accelerators eventually being too expensive to be built. Consequently alternative acceleration concepts have been explored with one of the most promising being wakefield acceleration in plasmas [1]. Here, an intense particle- or laser-driver-beam excites a relativistic plasma wave structure with acceleration gradients being able to exceed 100 GV/m. The concept of particle-driven plasma wakefield acceleration (PWFA) was developed in the 80s and having a major breakthrough in 2007 with the observation of energy doubling of a 42 GeV electron driver beam in a 85 cm long plasma target at SLAC [2]. Recent experiments also show the multi-gigaelectronvolt acceleration of positrons [3] and the GeV-acceleration of electrons in a proton-driven PWFA [4]. In the future the proton-driven PWFA has the potential to accelerate electron beams to the TeV-regime in a single acceleration stage [5].

The experiment was performed at the JETi-200 laser system at the Helmholtz Institute in Jena, a schematic drawing is depicted in Fig. 1. The main laser beam with a FWHM pulse duration of 20 fs measured in the near field and energy of 4.1 J were focused by an f/25 off-axis parabola to a vacuum intensity of 5×10^{19} W/cm^2, accelerating electrons in a 7 mm long underdense helium gas cell target with laser wakefield acceleration (LWFA). This resulted in electron beams with 120 pC in the energy range of 200-930 MeV with an energy peak at 800 MeV and down to 0.2 mrad FWHM divergence (see Fig. 2 (a,b)). These electron beams were used as a driver beam in a 2 mm $\times$ 1 mm - helium gas jet target. The depleted main laser beam was used to preionize the helium gas to a plasma electron density of about 1×10^{19} cm^{-3} before the driving electron pulse arrived.

*carola.zepter@uni-jena.de

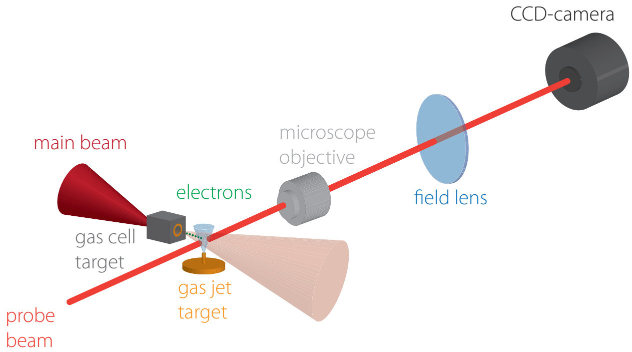

Figure 1: Schematic drawing of the experimental setup.

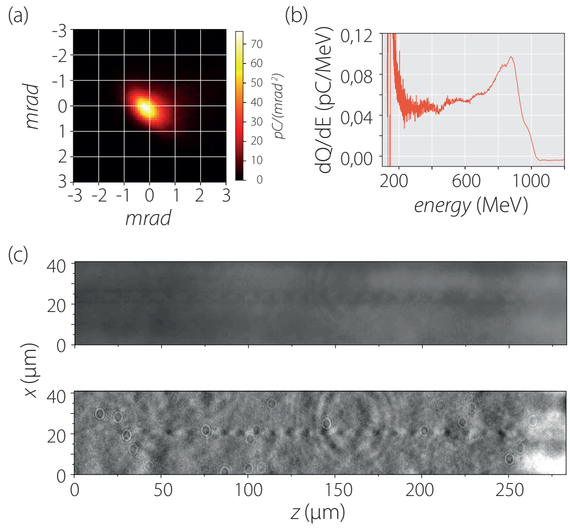

Figure 2: (a) Electron beam profile and (b) energy spectrum of a representative shot. (c) Shadowgram of an electron-driven plasma wave.

The electron bunch-plasma interaction was imaged with a high resolution imaging system and the JETi-200 few-cycle probe in a transverse probe geometry onto a CCD-camera. Fig. 2 (c) shows a shadowgram of the plasma wave in the second target driven by the electron bunch generated via LWFA in the first target.

References

[1] T. Tajima *et al.*, Phys. Rev. Lett. **43**, 267 (1979).

[2] I. Blumenfeld *et al.*, Nature **445**, 741 (2007).

[3] S. Corde *et al.*, Nature **542**, 442 (2015).

[4] E. Adli *et al.*, Nature **561**, 363 (2018).

[5] A. Caldwell *et al.*, Nat. Phys. **5**, 363 (2009).

Characterizing ultra-low emittance electron beams using structured light fields

Andreas Seidel*[1], Jens Osterhoff[2], and Matt Zepf[1,3]

[1]Friedrich-Schiller-Universität, Fürstengraben 1, 07743 Jena, Germany; [2]Deutsches Elektronen-Synchrotron DESY, Notkestraße 85, 22607 Hamburg, Germany; [3]Helmholtz Institute Jena, Fröbelstieg 3, 07743 Jena, Germany

We have performed 2D simulations on a novel, highly sensitive method for the single-shot characterization of the electron beam waist and emittance using interfering laser beams. Simulation results show applicability in the range of [0.01,1] mm mrad but promise even smaller emittances to be characterized.

Emittance describes the 6-dimensional phase-space. It is one of the most essential quality parameters for many applications, such as synchrotrons or free-electron-lasers. Developments in both conventional and laser-plasma accelerator technology now make it possible to generate electron bunches with emittances of 0.1mm mrad and better. The present methods for determining the emittance such as beam focus scanning or the pepperpot method, have shown to resolve these values, but the measurement of better emittances would become very challenging and require large setups.

In our proposed method, two laser beams cross at an angle θ, which creates a stationary interference grating. An electron bunch passes through this grating structure, and its phase space is modulated due to the ponderomotive potential acting on the bunch. In the following free space propagation, the phase space does not experience any further changes, and the modulation can be measured on a scintillation screen. The results of 2D PIC-simulations conducted using the code EPOCH are shown in Figure 1. The initial electron parameters were chosen to match present laser wakefield accelerators and the intensity of the laser is varied between 0.1 and 2 I_0 ($I_0 = 3.5 \cdot 10^{16}$ W/cm^2), where

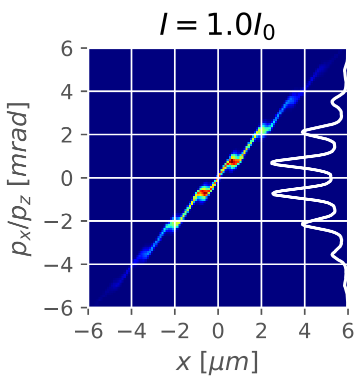

Figure 1: Momentum space of an electron beam ($\gamma_e = 100$, $\sigma_x = 100$ nm, $\sigma_{x'} = 2$ mrad, $\sigma_z = 2$ μm) after interaction with optimized laser intensities White curve: transverse momentum space integrated along x (measured signal on detector)

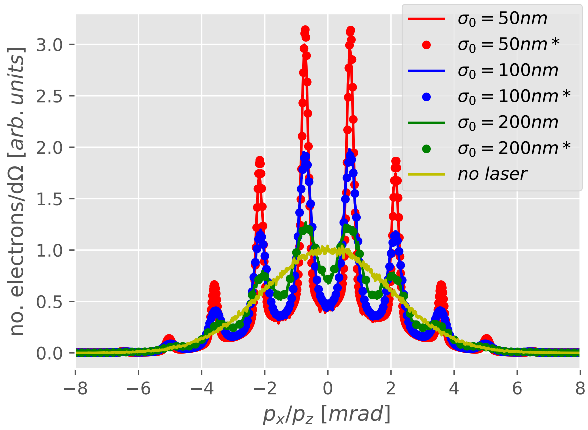

Figure 2: Transverse momentum space of electron beams with different σ_x after interaction ($\gamma_e = 100$, $\sigma_{x'} = 2$ mrad and $\sigma_z = 2$ μm)

$I_0 = 1$ corresponds to the optimal laser intensity. For an intensity $I < 0.1 I_0$, there is no measurable modulation of the phase space. However, already from 30% optimal intensity, small modulations become visible in the phase space and thus measurable in the momentum space (plotted in white color and corresponds to the measured signal on a detector). Notice that the modulations also occur at significantly higher intensities, but the depth of the modulation becomes increasingly shallower. The laser intensity parameters used in the simulations do not represent minimum requirements. Instead, by a clever design of laser focus and position of the electron bunch in phase space, the required power can be reduced to 1 TW and below. Figure 2 compares the results of the measured signal on the detector predicted by simulations and our analytical model. It can be seen that a prediction over a wide range of electron source sizes and therefore the emittance is achievable.

Although the simulations describe the interaction of monoenergetic electron bunches, this method can also be applied to poly-chromatic beams by combining this method with an electron dispersing dipole magnet deflecting in the complementary plane to the laser grating.

Future work will focus on verifying the simulation results in an experiment at JETi200.

The authors acknowledge funding from the Federal Ministry of Education and Research of Germany in the Verbund-forschungsframework (project number 05K16SJB).

*seidel.andreas@uni-jena.de

Enhanced x-ray yield from tilted shock front injection at JETI200

D. Ullmann*[1,2], H. Harsh[1,2], F. C. Salgado[1,2], S. Kuschel[3], and M. Zepf[1,2]

[1]Helmholtz Institute Jena, Fröbelstieg 3, 07743 Jena, Germany; [2]Institute of Optics and Quantum Electronics, Friedrich-Schiller-Universität Jena; [3]University of Hamburg, Edmund-Siemers-Allee 1, 20146 Hamburg

We report on preliminary results from experiments at the JETI200 laboratory. A dedicated beam time investigated the generation of x-rays by controlling the properties of electron beams from tilted shock front injectors.

Rapidly accelerating electron beams originating from laser wakefield accelerators (LWFAs) [1] are excellent prerequisites for generating short and intense x-ray pulses [2]. This radiation is triggered by the transverse motion of the accelerating electron beam known as betatron oscillations. In LWFAs, such electron beams are commonly generated by shock fronts [3]. We report on experimental investigation of tilted shock front injection, i.e. exploiting shock fronts that are oblique w.r.t. the propagation axis of the plasma accelerator as illustrated in Fig. 1 and consequently produce electron beams with increased betatron amplitude. Tilted shock front injection and the resulting radiation has

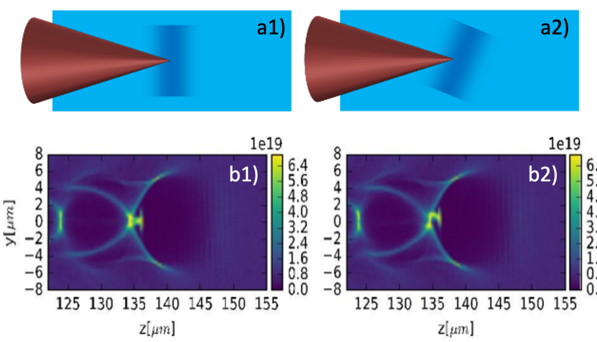

Figure 1: Principle of electron generation employing conventional (a1) and tilted shock front injection (a2). The laser propagation direction is indicated in red. b) illustrates snap shots of the LWFA injection process from particle-in-cell simulations according to a). Courtesy of S. Kuschel.

been studied at the JETI200 laser system. The JETI pulses of $\tau \approx 20$ fs FWHM duration and 5 J pulse energy were focused by an f/20 off-axis parabola to a vacuum r.m.s. diameter of 13 μm. Helium from a supersonic gas jet served as target, resulting in peak plasma densities of approximately $2 \times 10^{18}\,\mathrm{cm}^{-3}$. Tilted shocks were generated by a rotatable blade. Spectra of injected and accelerated electron populations were recorded using a permanent magnet and a scintillation screen. Simultaneously, profiles of the generated x-rays were acquired using an Andor BEN x-ray camera. This allowed for correlating properties of the electron beam and the resulting betatron radiation. Measurements excluding the blade were conducted to ensure electron trapping and radiation originated solely from shock front injection.

*daniel.ullmann@uni-jena.de

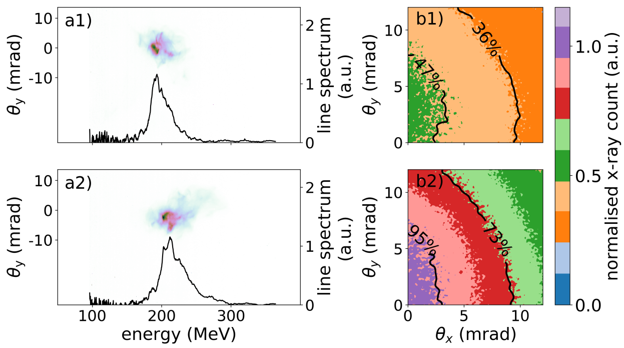

Figure 2: a), normalised electron spectra from conventional (a1) and tilted shock front injection (10°, a2) as function of the beam divergence θ_y and particle energy. Black lines illustrate the projected line spectra (right axis). Both spectra are normalised to the same value and contain a similar number of electrons. b), x-ray profiles corresponding to measurements in a) dependent on the x-ray divergence θ_x and θ_y. Both distributions are normalised to the maximum value of b2).

Figure 2 a1) shows the electron spectrum obtained from shock front injection, i.e. without rotation. The electron beam features a quasi-monoenergetic spectrum characteristic for localised injection. An electron beam injected by a 10° tilted shock front is visualised in Fig. 2 a2). The charge and energetic composition is similar for both particle beams. This is vital for comparing the x-ray profiles resulting from these beams, as the betatron radiation strongly scales with the charge and energy of the electron population [2]. The corresponding x-ray profiles are shown in Fig. 2 b) and demonstrate increased betatron flux by a factor of 2 in case of the tilted shock front injection. We anticipate further insights into the radiation properties from analysis of additional diagnostics. These include Ross filters and gold gratings and will reveal properties of the spectral content of the generated betatron radiation to complete the characterisation of this effect.

ESF funded Forschergruppe 2017*FGR0074 (Thüringer Aufbaubank).*

References

[1] T. Tajima and J. M. Dawson, Phys. Rev. Lett. **43**, 4 (1979).

[2] S. Corde et al., Rev. Mod. Phys. **85**, 1 (2013).

[3] A. Buck et al., Phys. Rev. Lett. **18**, 185006 (2013).

High Quality Betatron X-rays from JETi200

Harsh Harsh*[1], Daniel Ullman[1], Felipe C. Salgado[1,2], Alex Sävert[1], and Matt Zepf[1,2]

[1]Helmholtz Institute Jena, Fröbelstieg 3, 07743 Jena, Germany; [2]IOQ, FSU, Jena

When a relativistic laser pulse propagates in an underdense plasma, electrons are injected into the laser wakefield and their transverse oscillation gives rise to betatron X-ray emission [1]. The betatron beam has small source size (< 5 µm), fs pulse duration and high photon energy (1-100 keV) which makes it relevant for pump-probe experiments and in material and biological sciences. At JETi200 not only did we produce betatron beams for the first time but we also implemented a technique to potentially increase the betatron yield.

Betatron radiation has similar characteristics to synchrotron radiation in the wiggler regime at the fundamental wavelength [2]. The emitted betatron spectrum is a function of electron γ-factor and the electron transverse oscillation amplitude. The on-axis radiated spectrum can be simplified as:

$$\left.\frac{d^2 I}{d\omega d\Omega}\right|_{\theta=0} \simeq N_\beta \frac{3e^2}{2\pi^3 \hbar \varepsilon_0 c}\gamma^2 \xi^2 K^2_{2/3}(\xi) \qquad (1)$$

Where N_β is the number of oscillations, $K_{2/3}$ is the modified Bessel function of the second kind with $\xi = E/E_{\rm crit}$ [3]. $E_{\rm crit}$ is the energy within the distribution above and below which lies half of the radiated power, and is given as:

$$E_{\rm crit}[\mathrm{keV}] \simeq 5 \times 10^{-24} \gamma^2\, n_e[\mathrm{cm}^{-3}]\, r_\beta[\mathrm{\mu m}] \qquad (2)$$

Where n_e is plasma density and r_β is the source size [1].
A gas cell with H_2+N_2 (95 % + 5 %) mixture was used and the acceleration length was varied from 3 mm to 10 mm. Best performance was obtained a laser spot size of ≈ 25 µm, ≈ 2.5 J on target , 10 mm acceleration length and $6 \times 10^{18} cm^{-3}$ plasma density. Ross pairs were used for spectrum analysis with an estimated $\sim 10^9$ photons in 10-20 keV and $\sim 10^6$ photons in 60-80 keV energy bin, a highly competitive performance. The source size was < 3 µm with data analysis is still ongoing (see Fig. 1).
The betatron yield can be maximised by increasing the transverse momentum of the electrons in the wakefield. To control this parameter a gas jet with a razor blade was used to produce shock front which could be tilted by rotating the blade. This rotation of shock front, increased the transverse oscillation of the trapped electrons, which in turn increases the number of x-ray photons. The 5 mm gas jet with He+N_2 (95% + 5%) mixture was used and the experimental data indicates a significant increase in relative photon yield by change in shock front angle (see Fig. 2).

The authors acknowledge funding from ESF, EU and Freistaat Thüringen.

*harsh.harsh@uni-jena.de

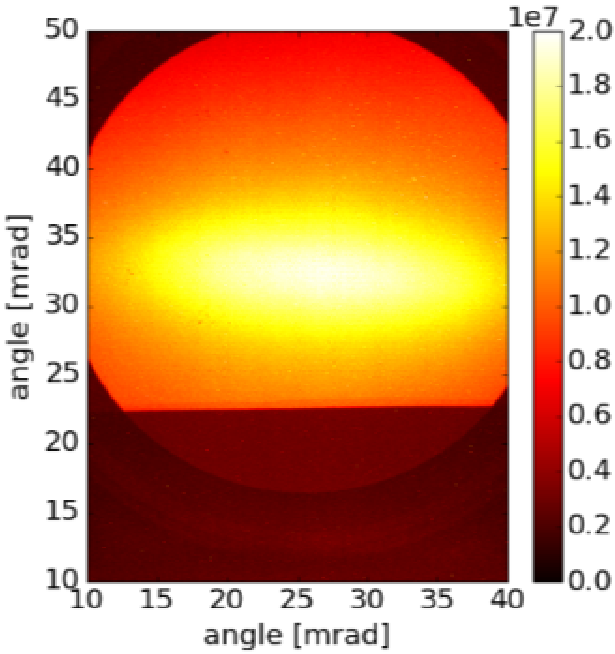

Figure 1: A 12-bit, 150 × 120 mm CMOS detector ('shadobox') was used to detect photons in 10 - 225 keV energy range. The beam has 25 × 10$mrad$ divergence and ∼18 keV critical energy.

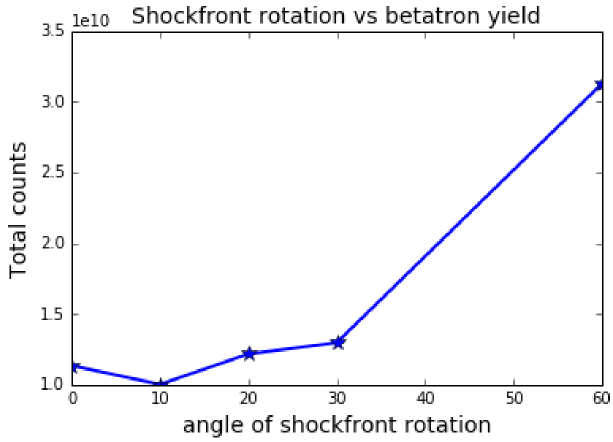

Figure 2: Demonstration of increase in betatron yield at JETi200 with shock front angle. Note the total yield is lower compared to the gas cell due to the reduced γ of the e-beam.

References

[1] M. Schnell *et al.* Phys. Rev. Lett. **108**, 075001 (2012).

[2] S. Fourmaux *et al.*, Opt. Lett. **36**, 2426 (2011).

[3] S. Corde *et al.*, Rev. Mod. Phys. **85**, 1 (2013).

Single-Shot Measurements of Space-Time Resolved Laser-Induced Ionization Dynamics on Thin Foils

Y. Azamoum*[1,2], G. A. Becker[1], S. Keppler[1,2], S. Skupin[3], G. Duchateau[4], F. Catoire[4], I. Tamer[1,2], M. Hornung[1,2], A. Kessler[1,2], M. Hellwing[1], F. Schorcht[2], and M. C. Kaluza[1,2]

[1]Institute of Optics and Quantum Electronics, Jena Germany; [2]Helmholtz Institute Jena, Germany; [3]Institut Lumière Matière, Université Lyon 1 - CNRS, Villeurbanne, France; [4]Université de Bordeaux-CNRS-CEA, CELIA, France.

We explore experimentally and numerically the ionization dynamics induced during laser-thin foil interaction at intensities $I < 10^{16}$ W/cm². Our space-time resolved pump-probe measurements using a temporally stretched broadband probe [1] allows us to determine the spatio-temporal evolution of the plasma with a single-pulse probe illumination. The performed numerical simulations exhibit ionization timescales which are in a good agreement with the measured values.

Highly energetic ion beams can, nowadays, be generated during relativistic laser-thin foil interactions. However, still a great effort is invested to enhance the beam quality for applications. Laser-driven ions are accelerated by several processes which strongly rely on the properties of the pre-plasma induced by the rising edge of the laser pulse. Therefore, a comprehensive study on the onset and the further development of the pre-plasma is of paramount importance, in particular, shedding light on the ionization processes which rule the plasma formation. In this work, we investigate the ionization dynamics for plastic and diamond-like carbon (DLC) target foils with 3 µm and 10 nm thickness, respectively. The experiments were performed at the POLARIS laser system operated at HI Jena. The pump pulse is normally incident on the target whereas the positively chirped broadband ($\Delta\lambda \sim 150$ nm) probe pulse propagates at an angle of incidence of 37° through the interaction region. The latter is imaged onto a 1D-spatially resolving spectrometer which wavelength axis is converted to a temporal window defined by the probe pulse duration of ~ 6 ps [1]. The 1D space-time resolved transmission measurements at a pump intensity of $I \approx 3 \times 10^{15}$ W/cm² are depicted in Fig. 1.

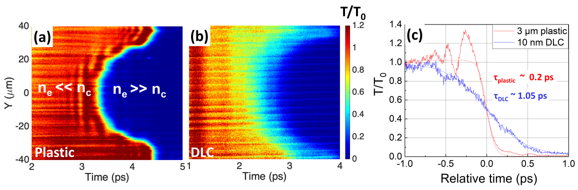

Figure 1: Transmission measurements for 3 µm thick plastic (a) and 10 nm thick DLC (b). Temporal transmission profiles at $Y = 0$ µm for plastic and DLC foils (c).

Figure 1 (a) and (b) present an opaque region corresponding to the overdense plasma where $T/T_0 \sim 0$, $n_e \gg n_c$. T and T_0 are the probe pulse's transmission with and without the main pulse. n_e, n_c are the electron density and the critical density respectively. As the ionization dynamics govern the electron density evolution, Figure 1(c) indicates that the ionization process takes longer for DLC with $\tau_{\text{DLC}} \sim 5\tau_{\text{plastic}}$. τ is the time required for the transmssion to decrease from 90 % to 10 %. To elucidate the physical processes behind this behaviour, we performed numerical calculation including an ionization model based on Multiple Rate Equation [2], to retrieve the time-dependent electron density considering the measured temporal intensity contrast of the pump pulse and solving Maxwell's equations for the probe propagation through the plasma. The calculated transmissions at a pump intensity $I = 10^{15}$ W/cm² are given in Fig. 2.

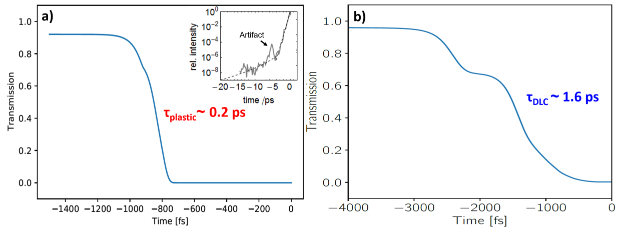

Figure 2: Simulated transmission results for 3 µm thick plastic (a) and 10 nm thick DLC (b). The inset in (a) is the measured temporal intensity contrast of the pump pulse.

The results show that n_c is reached during the rising edge of the laser pulse for both materials. Besides, the ionization starts earlier for DLC and, as observed in the experiment, $\tau_{\text{DLC}} \gg \tau_{\text{plastic}}$. The photoionization rate $\Gamma_n = \sigma_n I^n$ (σ_n is the n-photon ionization cross section) may explain these observations. On the one hand, the low band gap of DLC ($E_{\text{g-DLC}} \sim 1$ eV and $E_{\text{g-plastic}} \sim 4$ eV) results in a single photon absorption to bridge the gap ($E_{\text{ph}} = 1.2$ eV for $\lambda_{\text{POLARIS}} = 1.03$ µm). This leads to a larger Γ_n at lower I due to the highest σ_n [3]. On the other hand, Γ_n evolves linearly with I for DLC, resulting in a larger τ_{DLC} to reach the overdense plasma state. Γ_n scales, however, nonlinearly with I for plastic, leading to $\tau_{\text{plastic}} \ll \tau_{\text{DLC}}$ due to a highest Γ_n. Furthermore, due to the nm-thickness of the DLC, the optical tunneling of the probe is high ($\sim$ 70 %) when n_c is reached. Thus a higher n_e and consequently a longer τ_{DLC}, are required for the plasma to become opaque to the probe light. This study demonstrates a detailed plasma evolution which strongly depends on the interaction parameters. In the future, this investigation of the ionization dynamics will provide, not only, an unprecedent detailed initial pre-plasma condition for particle-in-cell codes but also will be a powerful tool to help retrieving the actual temporal and spatial laser pulse intensity contrasts in relativistic laser-plasma interaction.

[1] Y. Azamoum *et al.*, HI Jena Annual Report 2019, p. 35.
[2] B. Rethfeld, Phys. Rev. Lett, **92**, 187401, (2004).
[3] P. Agostini and G. Petite, Cont. Phys., **29**, 57, (1988).

*yasmina.azamoum@uni-jena.de

Preliminary Results and Interpretation of Optical Rear-Surface Radiation from Thin Foils Irradiated by High-Intensity Laser Pulses

S. Hell*[1], G. A. Becker[1], Y. Azamoum[1,2], S. Keppler[1,2], M. Hellwing[1], M. Hornung[1,2], F. Schorcht[2], and M. C. Kaluza[1,2]

[1]Institute of Optics and Quantum Electronics Jena, Germany; [2]Helmholtz Institute Jena, Germany

A spatio-spectral diagnostic of the optical radiation emitted by relativistic electrons when crossing the plasma-vacuum boundary in high-intensity laser-plasma experiments is presented. The analysis of the results from this diagnostics provides information about plasma heating and the laser intensity at the target front.

During the interaction of a high-intensity laser with an overdense plasma, short bunches of fast electrons are accelerated at the laser frequency ω_L (resonance absorption and vacuum heating) and twice the laser frequency $2\omega_\mathrm{L}$ (relativistic $\mathbf{v} \times \mathbf{B}$ heating) [1]. These fast electrons propagate to the target rear side where they produce coherent optical radiation (COR) [2, 3]. Such COR is most likely due to synchrotron and transition radiation which exhibit similar spectral characteristics [2, 4] in the spectral range of our measurement (720 nm to 940 nm). In this work, the COR emitted by fast electrons crossing the boundary between an overdense plasma and vacuum has been analyzed to investigate their temporal structure.

The experiments were performed at the POLARIS laser system, operated at the Helmholtz Institute in Jena. The laser pulses ($\lambda_L = 1030\,\mathrm{nm}$) are focused to reach an intensity of $1.1 \times 10^{18}\,\mathrm{W/cm^2}$ on a 370 nm thick aluminum foil at normal laser incidence. This laser intensity is estimated from the independent parameters pulse energy E, pulse width τ and focal spot area A, whereas the latter is measured at low intensities. Consequently the actual laser intensity in the experiment can deviate from this estimate. The target rear optical emission is imaged at an angle of 37° to the foil's normal direction by a microscope objective and a lens onto the entry slit of an imaging spectrometer. The width of this vertical slit corresponds to $\approx 4\,\mu\mathrm{m}$ on the foil's surface. The slit is imaged onto a camera after passing a grating to obtain a spectral decomposition of the vertical radiation profile. Based on polarization-resolved measurements [3], we assume coherent transition radiation (CTR) to be the source of COR in our experiment. The measured spectral CTR intensity is depicted in figure 1(a).

According to theory [2, 5], the spectral CTR intensity in figure 1(a) is governed by the factor $\sin^2(n_b\omega_L T_L/2)/\sin^2(\omega T_L/2)$ for an electron current containing n_b bunches spaced at $T_L = 2\pi/\omega_L$ and/or $2n_b$ bunches spaced at $T_L/2$. The Fourier-analysis of the CTR spectrum, as shown in figure 1(b), allows to obtain n_b from the CTR spectrum and shows a clear peak around $n_b = 39$ for bunches at ω_L, corresponding to 78 bunches at $2\omega_L$. From n_b and the measured pulse width τ one can calculate the peak laser intensity to be $1.7 \times 10^{18}\,\mathrm{W/cm^2}$ if one counts the optical laser cycles above the relativistic intensity level. The presented CTR measurement provides a more direct intensity diagnostic using less parameters and is in good agreement with the estimated intensity from the laser parameters E, τ and A. Finally, further investigation is required to understand the additional peaks observed in the Fourier analysis of the CTR spectrum, which might be due to recirculating electron bunches.

* sebastian.hell@uni-jena.de

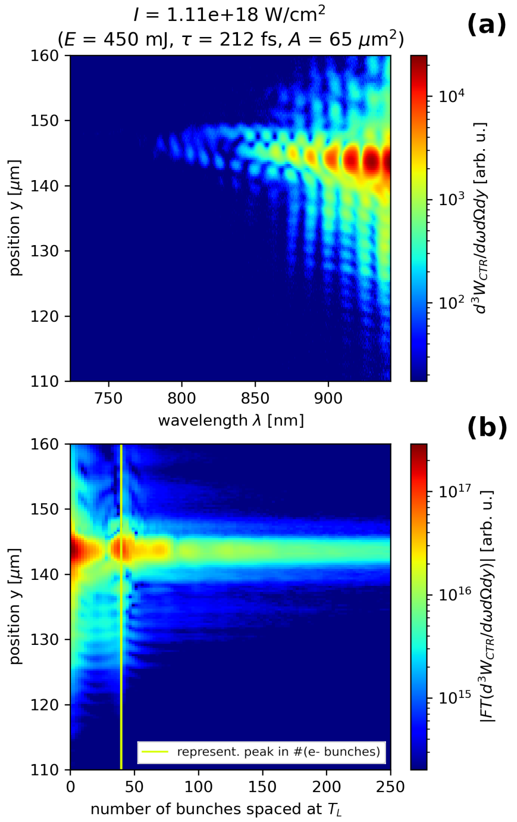

Figure 1: (a) Exemplary measurement of the imaging spectrometer. The characteristics of the laser shot (at FWHM) are specified in the image heading. (b) The Fourier-transformed spectrometer data.

References

[1] A. Macchi *et al.*, Rev. Mod. Phys. **85**, 751 (2013).

[2] H. Popescu *et al.*, Phys. Plasmas **12**, 063106 (2005).

[3] C. Bellei *et al.*, New J. Phys. **12**, 073016 (2010).

[4] K. Ishi *et al.*, Phys. Rev. A **43**, 5597 (1991).

[5] C. Bellei *et al.*, Plasma Phys. Control. Fusion **54**, 035011 (2012).

A parametric study on proton acceleration during intense laser-thin foil interaction

M. Almassarani*[1,2], S. Meng[2], B. Beleites[1,2], F. Ronneberger[1,2], G. G. Paulus[1,2], and A. Gopal[1,2]

[1]Helmholtz Institute Jena, Fröbelstieg 3, 07743 Jena, Germany; [2]Institut für Optik und Quantenelektronik, Physikalisch-Astronomische Fakultät, Friedrich-Schiller-Universität, Max-Wien Platz 1, 07743 Jena, Germany

We experimentally investigated the accelerated proton beam characteristics -maximum energy and number- by varying the incident laser polarization, energy, focal spot size, and pulse duration. The proton spectra were recorded using a single-shot Thomson parabola spectrometer with a wide detection range from few tens of keV up to several MeV. Experimental findings are in agreement with theoretical works.

It is understood that the experimental conditions greatly affect the temperature of the energetic electrons and subsequently the accelerated protons and these conditions can vary between different laser systems. Thus to find the optimal conditions for the particle acceleration process on our laser system we carefully varied the laser parameters and recorded and analyzed the proton and electron spectra. The experiments were carried out in the Jeti40 laser facility where the polarization state of the laser was controlled by a 4-inch halfwave plate placed in the collimated beam. The laser pulses were focused by a 45° off-axis parabola (OAP) onto an Aluminium target with a thickness of 6 μm reaching intensities above 1×10^{19} W/cm^2. We constructed the energy spectra of the protons emitted in the target normal direction by using a single-shot Thomson parabola spectrometer (TPS) equipped with an (MCP) and a (CCD). The TPS is capable of detecting protons with energy from 30 keV up to several MeV in a single shot. We also used a magnetic deflection spectrometer with image plates to measure the temperature of the electrons along the target normal direction. The setup is shown in Fig. 1.

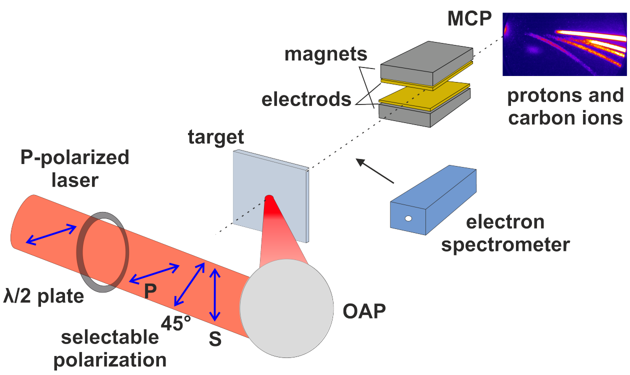

Figure 1: Schematic of the experimental setup.

We investigated the dependence of the temporal duration on the proton yield and energy for various polarization states of the incident laser. The results are presented in Fig. 2. We observe an increase in the maximum proton energy until 70 fs duration of the incident laser pulse, followed by a decrease with the laser pulse duration following a scaling law of $(1/\tau_{laser})^{0.5}$. This is in agreement with the analytical model of a radially confined surface charge induced by laser-accelerated electrons on the target rear surface[2].

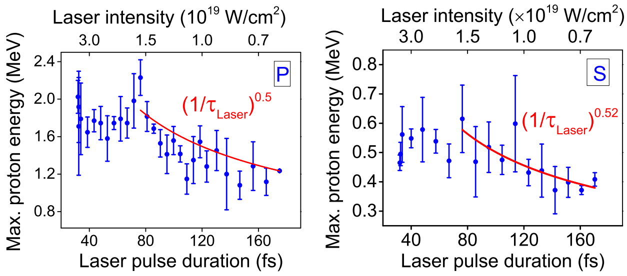

Figure 2: Maximum proton energy as a function of laser pulse duration. (left) P- and (right) S-polarization. Red (solid) line is a power-law fitting.

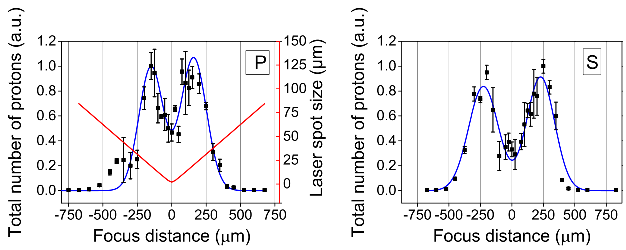

Figure 3: Total number of protons as a function of the target position along the laser focus, blue (solid) line is a Gaussian peak fit. (left) P-, (right) S-polarization. Red line represents laser spot size on target.

In a separate measurement, we fixed both the laser energy and the pulse duration while varying the laser spot size on the target by moving it along the focal axis. As a result, the intensity on target varied with the spot size. We summed the number of all detected protons from 30 keV up to 2 MeV. The results are presented in Fig. 3. We observe a double-peak structure around the zero position of the focus for both polarization states which we accounted for by the volumetric effect. Although the laser intensity decreases fast away from the focus, the irradiated area on the target is larger meaning that a higher number of particles is involved in a given volume.

References

[1] M. Almassarani *et al.*, submitted (2021).

[2] J. Schreiber *et al.*, Phys. Rev. Lett. **97**, 045005 (2006).

*mohammed.almassarani@uni-jena.de

PHOTON AND PARTICLE SPECTROSCOPY

High harmonic generation in CdSe quantum dots

Harshitha N. G. *[1,2], V. Korolev[1], R. Baruah[3], M. Wächtler[3], C. Spielmann[1,2], and D. Kartashov[1]

[1]Institute of Optics and Quantum Electronics, Max-Wien-Platz 1, 07743 Jena, Germany; [2]Helmholtz Institute Jena, Fröbelstieg 3, 07743 Jena, Germany; [3]Leibniz Institute of Photonic Technology, Department Functional Interfaces, Albert-Einstein-Straße 9, 07745 Jena, Germany

The enhancement and control of non-linear phenomena at a nanometre scale has a wide variety of applications in science and industry. One important non-linear process is high harmonic generation (HHG) that can be altered by the complex electronic structure of exotic materials in many interesting ways. For example, one recent study highlighted that the quantum confinement feature of nanomaterials can result in an enhancement of the HHG yield [1]. In this report, we present experimental results on high-order harmonic generation from thin layers of CdSe quantum dots.

Quantum dots are zero-dimensional (0D) semiconductor nanocrystals having charge carriers confined in all three spatial dimensions. This confinement results in discrete electronic structure resembling the electronic/optical behaviour of individual "artificial" atoms or molecules. One of the consequences of this confinement is a strong dependence of the bandgap on QDs diameter.

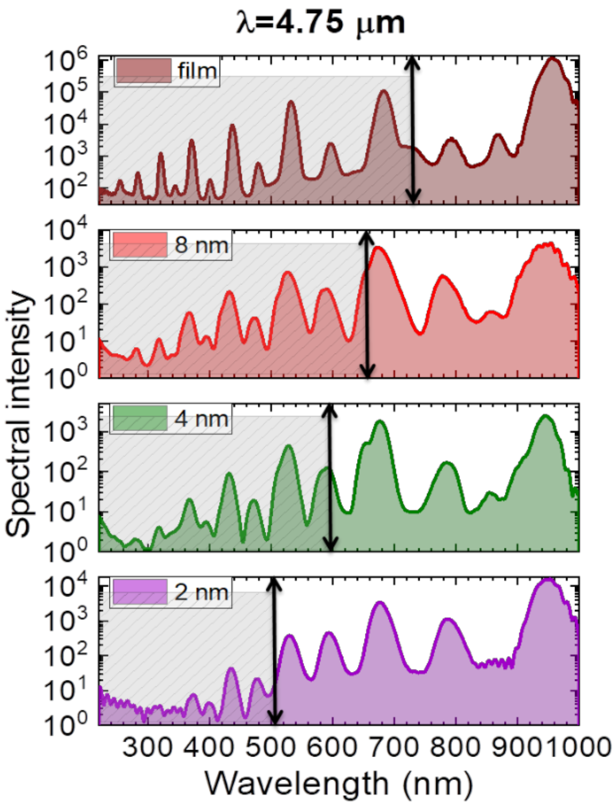

Figure 1: High-order harmonic (HH) spectra emitted from a CdSe film and CdSe QDs of various sizes excited by femtosecond MIR laser pulses.

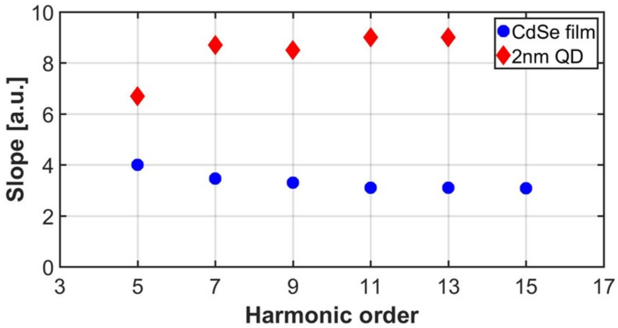

Figure 2: Slope of the intensity-dependent harmonic yield as a function of harmonic order.

We study influence of quantum confinement effects on extreme nonlinearities in solids resulting in high-order harmonic generation. In experiments, HHG was driven by a mid-infrared (MIR) laser source delivering 100 fs pulses at a central wavelength of 4.75 μm and at a repetition rate of 1 kHz. Micron-thick layers of CdSe QDs were prepared using drop cast method on a c-cut sapphire substrate.

Fig. 1 shows the experimentally obtained high-order harmonic spectra from CdSe QDs with different sizes and from a CdSe film as a reference. The shaded regions on the plot represent above band gap harmonics and the arrows mark the position of the bandgap for film, 8 nm, 4 nm, and 2 nm QDs. As follows from Fig.1, reduction in size of QDs leads to suppression of above bandgap harmonics. In addition, the harmonic yields as a function of the pump intensity were recorded. At highest pump intensities the yields show tendency to saturation, but for moderate intensities these dependencies in log-log scale can be well approximated by a linear function. The dependence of the corresponding slopes on harmonics order is shown in Fig. 2 and demonstrates much sharper dependence of harmonic yield on the pump intensity in QDs in comparison to the bulk film.

As a next step, we plan to investigate influence of quantum confinement effects on HHG in materials with different dimensionalities, namely nanowires (1D confinement along the radius) and 2D stacked materials.

References

[1] C. R. McDonald *et al.*, Phys. Rev. Lett. **119**, 183902 (2017).

* harshitha.nandiga.gopalakrishna@uni-jena.de

XUV coherence tomography driven by laser plasma sources

J. Reinhard*[1,2], S. Fuchs[1,2], S. Skruszewicz[1,2], F. Wiesner[1,2], M. Wünsche[1,2], J. J. Abel[2], J. Nathanael[1,2], C. Rödel[1,2], and G. G. Paulus[1,2]

[1]Helmholtz Institute Jena, Fröbelstieg 3, 07743 Jena, Germany; [2]Institute of Optics and Quantum Electronics, Friedrich Schiller University Jena, Germany

We report on the extension of XUV Coherence Tomography (XCT) into the soft x-ray range by using a laser-plasma source. The source has already been build and tested and shows broadband soft x-ray spectra, which are well suited for XCT. The decreased wavelength will lead to an improved depth resolution and high label-free material-specific contrast.

XUV Coherence Tomography (XCT) is a non-destructive three-dimensional imaging technique with nanoscale resolution. It can efficiently utilize broad bandwidth extreme ultraviolet (XUV) radiation from laser-based XUV sources like high harmonics. The depth structure of a sample is obtained by measuring the spectrum of the light backscattered from the sample superimposed with light reflected at the surface (common-path interferometric design) and a subsequent Fourier transform [1]. XCT has applicational potential e.g. in the inspection of semiconductors and lithographic or in solid state interface physics.

The common-path interferometric XCT setup is technologically attractive but has a characteristic disadvantage: The reconstruction only yields the autocorrelation of the sample's depth structure rather than the actual structure and, accordingly, the phase information is lost. However, with our stable one-dimensional phase retrieval algorithm (PR-XCT) we can reconstruct the actual sample structure from its autocorrelation [1]. Furthermore, detailed and accurate phase information strongly enhances the spectroscopic potential provided by the atomics inner-shell resonances in the XUV spectral region. With its inherently broadband spectroscopic approach and together with the recovered spectral phase, PR-XCT is a well suited tool to exploit material contrast. We could show, that depth-resolved material information can be accessed by XCT [2] and that label-free element specific-identification of buried structures within a nanometer depth resolution is possible.

Many elements have their specific inner shell resonances in the soft x-ray wavelength range. However, our high harmonic source is limited to approx. 12 nm. Therefore, we started the development of a laser-plasma soft x-ray source to perform XCT. A nanosecond laser pulse with high pulse energy is focused into a gas jet. The plasma can emit narrow bandwidth radiation as well as broad bandwidth radiation depending on the gas. Figure 1 a) shows the implementation of a gas-puff target we obtained within a collaboration with the University of Warsaw. In part b) first measured spectra for nitrogen and krypton are shown. The latter one is well suited for XCT. In a collaborative effort we will soon be able to perform XCT in the soft x-ray range and to exploit the high material contrast in this range [3].

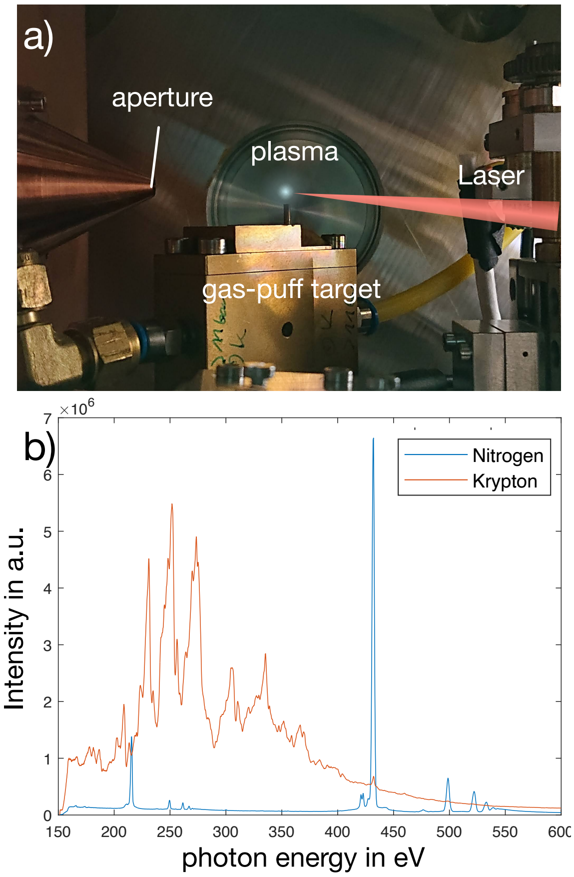

Figure 1: Laser plasma source for XCT: a) A well-confined gas jet is emitted from the gas-puff target and hit with a 10 ns laser pulse with a pulse energy of ≈2 J. The plasma radiates soft x-ray light in the full solid angle. Only a small fraction of the light will be refocused through an aperture to the actual sample. b) Two soft x-ray spectra are shown (nitrogen and krypton). The bandwidth of the krypton spectrum is well suited for XCT.

The authors acknowledge funding from the Thüringer Aufbaubank (2015FGR0094, 2018FGR0080) , the DFG (Beethoven 2 Lab-XCT) and the Helmholtz excellence network (ExNet).

References

[1] S. Fuchs *et al.*, Optica **4**, 8 (2017).

[2] F. Wiesner *et al.*, Optica **8**, 2 (2021).

[3] S. Skruszewicz *et al.*, Appl. Phys. B **127**, 4 (2021).

* julius.reinhard@uni-jena.de

Ptychographic Imaging of Soft X-ray Laser Plasma Amplification

F. Tuitje*[1,2], T. Helk[1,2], J. Gautier[3], F. Tissandier[3], J.-P. Goddet[3], E. Oliva[4,5], A. Guggenmos[6], U. Kleineberg[6], S. Sebban[3], C. Spielmann[1,2], and M. Zürch[1,2,7]

[1]Institute for Optics and Quantum Electronics Jena, Abbe Center of Photonics, Germany; [2]Helmholtz Institute Jena, Germany; [3]Laboratoire d'optique appliquée, ENSTA-ParisTech, 91762 Palaiseau, France; [4]Departamento de Ingeniería Energética, ETSI Industriales, Universidad Politécnica de Madrid, Spain; [5]Instituto de Fusión Nuclear, Universidad Politécnica de Madrid, Spain; [6]Ludwig-Maximilians-Universität München, Germany; [7]University of California at Berkeley, Department of Chemistry, USA

Using shorter wavelength light sources is a straightforward approach for improving spatial resolution in imaging. Table-top soft X-ray lasers (SXRL) offer a photon flux per pulse that allows for single shot imaging and near wavelength-limited resolution. In an SXRL, a high-energy pump pulse ionizes a solid or a gas until it reaches a nickel-like atomic configuration constituting a three-level lasing scheme. It has been recently shown that a SXRL operating in an amplified spontaneous emission (ASE) scheme exhibits low transverse coherence limiting the applicability for coherent imaging applications [1]. By seeding a SXRL with a highly coherent pulse generated by High Harmonic Generation (HHG) a higher photon flux and shorter pulse duration in the order of a few hundred femtoseconds was achieved [2] turning the SXRL into a laser plasma amplifier for the HHG radiation. We investigate the wavefront properties of a high-harmonic-seeded SXRL using a 2 J Ti:sapphire laser system depending on the arrival time of the seed pulse. The laser ionizes and inverts krypton atoms producing Kr^{8+} ions in a 5 mm long plasma waveguide emitting at 32.8 nm. For imaging the output of the laser plasma amplifier in amplitude and phase, we image a micron scale sample using ptychography (Fig. 1).

We find that HHG seeding results in excellent spatial coherence properties, while a high degree of temporal coherence is maintained through the narrow-band amplification. Further, we find that the time delay dependence between the pump and seed pulses causes significant reshaping of the amplified laser beam hinting at a seed-plasma interaction that is confirmed by model calculations. Finally, we successfully employ the characterized and optimized HHG-seeded SXRL for single shot coherent diffraction imaging which demonstrates the outstanding capabilities for ultrafast nanoscale imaging [3].

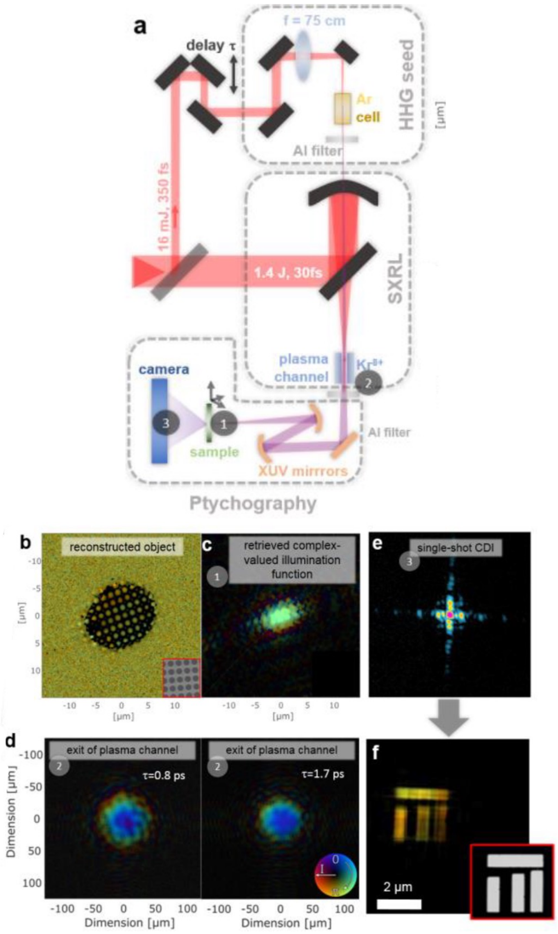

Figure 1: (a) Experimental scheme for ptychographic characterizing the beam of a HHG-seeded SXRL in amplitude and phase and single shot ultrafast imaging [3[. (b) Reconstruction of a microscopic object imaged using ptychography. The inset shows a SEM image of the used sample. (c) Reconstructed complex-valued illumination function at the sample. (d) Examples of measured complex-valued SXRL beam profiles at the exit of the plasma channel for two different time delays between SXRL pump and HHG seed as indicated. (e) Measured single shot coherent diffraction pattern. (e) Reconstruction of the object with ∼100 nm resolution. The inset shows SEM image of the sample used for single shot measurements. All panels except (e) show complex-valued spatial representations where the amplitude and phase are encoded by brightness and hue as indicated in right panel in (d).

References

[1] M. Zürch *et al.*, Scientific Reports **7**, 5314 (2017).

[2] A. Depresseux *et al.*, Nature Photonics **9**, 817 (2015).

[3] F. Tuitje, P. Martínez Gil, T. Helk *et al.*, Light Sci. Appl. **9**, 187 (2020).

* frederik.tuitje@uni-jena.de

A highly sensitive imaging polarimeter in the x-ray regime

Benjamin Grabiger*[1,2], Berit Marx-Glowna[2], Ingo Uschmann[1,2], Robert Loetzsch[1,2], Gerhard G. Paulus[1,2], and Kai S. Schulze[1,2]

[1]Institut für Optik und Quantenelektronik, Friedrich-Schiller-Universität Jena, Max-Wien-Platz 1, D-07743 Jena, Germany; [2]Helmholtz-Institut Jena, Fröbelstieg 3, D-07743 Jena, Germany

In the x-ray regime, polarization analysis plays a pivotal role in the investigation of the magnetic and electronic structure of materials. So far, those experiments have all been done at large-scale facilities like synchrotrons or free-electron lasers. They also rarely use any spatial resolution to accompany the sensitivity to polarization changes. Here we demonstrate, that we can transfer the successful x-ray polarimetry to small-scale facilities and establish experiments that can thrive with the higher flexibility and more available beamtime of small-scale facilities. We achieved a polarization purity of 8×10^{-8} with the combination of a microfocus rotating anode, collimating multilayer mirrors and two germanium polarizer crystals. We added to this polarimeter a 2D-detector and achieved a spatial resolution of 200 µm to investigate the micro-crystalline structure of beryllium sheets, commonly used as focusing lenses in the x-ray regime. The results are important for the development of x-ray optical instruments that combine high spatial resolution and high sensitivity to polarization changes.

X-ray polarimetry is a technique established at synchrotrons to investigate materials and their crystalline, electronic and magnetic structure. The polarization purity for such experiments, and thus the sensitivity to polarization changes, is usually in the order of 10^{-9} to 10^{-10}. At small-scale facilities, polarimetry is very rarely pursued due to the much smaller intensities and a more divergent beam. The best polarization purity reached so far was in the order of 10^{-5} by Schulze et al. in Jena [2].

We developed a polarimeter at a small-scale facility, combining a microfocus rotating anode, collimating multilayer mirrors and two germanium polarizer crystals. The polarimeter reaches a polarization puritiy of 8×10^{-8} and thus improves on the previous achieved values by more than two orders of magnitude. This high-precision polarimeter, which is unique at a low-scale facility, is capable of detecting a rotation of the polarization plane of $6''$ or an ellipticity in the order of 10^{-7} [1] and thus allowing high-precision polarimetry that was previously only available at synchrotrons or free-electron lasers.

The potential of today's x-ray lenses to magnify features in the 100 nm range [3] makes the combination of polarimeters and x-ray lenses interesting for material characterization. For this reason, it is important to know if and how the lens material itself influences the polarization.
Therefore, in a first step to achieve spatial resolution, we installed an areal detector with a 13.5 µm pixel size behind the analyzer crystal of our polarimeter. The spatial resolution is limited in the order of 200 µm due to the divergence of the x-ray beam. However, even with this spatial resolution, we can characterize the typical lens material, beryllium, and determine its effect on the polarization purity of the polarimeter. Figure 1 shows for two different grades of beryllium, that beryllium is significantly altering the polarization of the x-ray beam and decreases the sensitivity of the polarimeter by more than one order of magnitude.

* benjamin.grabiger@uni-jena.de

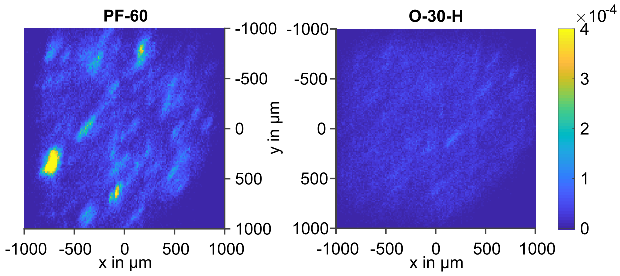

Figure 1: Polarization sensitive imaging of two beryllium samples with a CCD detector, one pixel is 13.5 µm × 13.5 µm in size. The colorbar shows flipped photons per second and pixel in a linear scale. Measuring time was three days. O-30-H is the typical lens material.

The polycrystalline nature of beryllium exhibits strong birefringence in the x-ray beam, that leads to these polarization changes. Therefore, beryllium should be avoided as material for optical elements within a high-precision polarimeter. Alternative ways to focus x-rays are necessary to realize a polarization microscope with sub-micron resolution. Possible are for example Kirkpatrick-Baez mirrors or the use of other materials for x-ray lenses. For the x-ray lenses, there are two options, either single-crystal material, e.g. diamond, with a precise crystal orientation and alignment of each lens to avoid birefringence or a material with an amorphous structure to avoid polarization changing effects altogether, e.g. glassy carbon and SU-8 polymer.

We gratefully acknowledge funding by the Deutsche Forschungsgemeinschaft (416700351) within the Research Unit FOR2783/1, by the Bundesministerium für Bildung und Forschung (05K16SJ2) and by the European Social Fund and the Free State of Thuringia (2017FGR0074).

References

[1] B. Grabiger *et al.*, Appl. Phys. Lett. **117**, 201102 (2020).

[2] K. S. Schulze *et al.*, Appl. Phys. Lett. **104**, 151110 (2014).

[3] C. G. Schroer *et al.*, Appl. Phys. Lett. **82**, 1485 (2003).

Disentangling x-ray dichroism and birefringence via high-purity polarimetry

Annika T. Schmitt *[1,2], Yves Joly[3], Kai S. Schulze[1,2], Berit Marx-Glowna[1,2], Ingo Uschmann[1,2], Benjamin Grabiger[1,2], Hendrik Bernhardt[1,2], Robert Loetzsch[1,2], Amélie Juhin[4], Jérôme Debray[3], Hans-Christian Wille[5], Hasan Yavaş[5,6], Gerhard G. Paulus[1,2], and Ralf Röhlsberger[1,2,5]

[1]Friedrich-Schiller-Universität Jena, Germany; [2]Helmholtz Institute Jena, Fröbelstieg 3, 07743 Jena, Germany; [3]Universite Grenoble Alps, CNRS, Grenoble, France; [4]Sorbonne Universite, Paris, France; [5]DESY, Hamburg, Germany; [6]SLAC, Stanford, USA

High-brilliance synchrotron radiation sources have opened new avenues for X-ray polarization analysis that go far beyond conventional polarimetry in the optical domain. With linear X-ray polarizers in a crossed setting polarization extinction ratios down to 10^{-10} can be achieved. This renders the method sensitive to probe tiniest optical anisotropies. Here we show that high-purity polarimetry can be employed to reveal electronic anisotropies in condensed matter systems with utmost sensitivity and spectral resolution. Taking CuO and La_2CuO_4 as benchmark systems, we present a full characterization of the polarization changes across the Cu K-absorption edge and their separation into dichroic and birefringent contributions.

While we receive visual information about our world through color and brightness of light, a less “obvious” property of light is its polarization. The polarization of light can change (e.g., rotate) when light is scattered by a material. The polarization change of the light contains valuable information about the properties of the illuminated material. For example, it allows insights about the preferred orientation of electrons in atoms (orbitals) and the directions along which electrons can move in a material. Such preferred directions are called anisotropies and often form the basis for specific properties of modern functional materials, e.g. directed current transport, magnetic alignment of nanostructures, optical birefringence etc.

In the experiment reported here we describe a new way to detect polarization changes of X-rays to investigate anisotropies in the electronic properties of materials with high sensitivity [1]. The samples studied were the metal oxides CuO and La_2CuO_4. These are starting materials for high-temperature superconductors, in which the electrons in the orbitals of the copper atom play a major role in superconductivity.

The key to the new measurement method is a technique that has been under development in Jena for many years, namely precision polarimetry with X-rays: If X-ray light is allowed to reflect several times at an angle of incidence of 45 degrees on a perfect single crystal of silicon, then this light is almost completely linearly polarized after reflection, i.e. it oscillates practically exclusively in one plane. Scattering of this light by an optically active material causes deviations from this perfection, which become apparent in a slight rotation of the plane of oscillation of the light. This rotation of polarization can be detected by reflecting the scattered light off a second, identical crystal whose reflection plane is rotated 90 degrees with respect to the first crystal. Due to the high perfection of silicon crystals, sensitivities in the range of 10^{-9} can be achieved.

Two optical effects contribute to the rotation of the polarization: the selective attenuation of the light by the sample (dichroism), and the direction-dependent refraction of the light (birefringence) in the material.

In this experiment, performed at the synchrotron radiation source PETRA III at DESY in Hamburg, we could separate the contributions of these two effects and attribute them to the interaction of the X-ray light with specific orbitals of the copper atom in the materials studied, see Fig.1. This provides a highly sensitive method for tracking down the electronic anisotropies in complex materials and investigating the role they play, for example, in novel forms of superconductivity, magnetism and optical properties.

Further development of the method promises to increase the detection sensitivity by a factor of 1000 to one in a trillion (10^{-12}). This could even make it possible to detect the optical birefringence of the vacuum, an effect that was predicted by Heisenberg and Euler as early as 1936, but which has so far eluded experimental proof. A corresponding experiment at the European X-ray laser is currently in preparation. If a dichroism of the vacuum were also detected in such an experiment, this could be a direct indication of particles beyond the Standard Model.

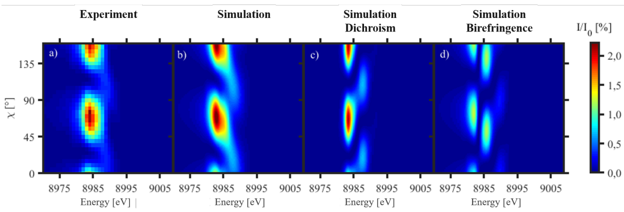

Figure 1: Comparison of measured data with calculated spectra of x-ray dichroism and birefringence of CuO for different azimuthal sample orientations χ.

The authors acknowledge funding from the European Social Fund (2017FGR0074), the Bundesministerium für Bildung und Forschung (05K16SJ2) and the Deutsche Forschungsgemeinschaft (416700351).

References

[1] A. T. Schmitt *et al.*, accepted for publication in Optica (2020)

* annika.schmitt@uni-jena.de

Laser Photodetachment of Negative Ions for Element Selective Suppression of Isobars in Accelerator Mass Spectrometry

Oliver Forstner*[1,2]

[1]Helmholtz Institute Jena, Fröbelstieg 3, 07743 Jena, Germany; [2]Friedrich–Schiller–University Jena, Max–Wien–Platz 1, 07743 Jena, Germany

Laser photodetachment of negative ions is a very promising method for introducing an element sensitive suppression of isobars in high sensitive mass spectrometry. However, being a non–resonant process one has to deal with low cross–sections of the photon–ion interaction. To overcome this the ion beam has to be slowed down to thermal energies in a radio frequency quadrupole ion cooler. Due to the lack of spectroscopic data especially of molecular negative ions, an experimental program for acquiring photodetachment data is underway at the low–energy electrostatic storage ring at the Goethe–University Frankfurt. Negative ions of helium and oxygen could be successfully stored in the ring and a laser setup is currently under construction. Spectroscopic information of radioactive ions could for the first time be acquired at the facility ISOLDE at CERN. Notably the electron affinity of the rarest naturally occurring element on earth, astatine, could be measured for the first time.

In the framework of the BMBF funded joint project 05K2019 – LISELatDREAMS, a radio–frequency ion beam cooler is currently being set-up at the FSU Jena. At a later stage of the project the LISEL cooler (Low–energy Isobar SEparation by Lases) will be transferred to the HZDR and installed at the DREAMS (DREsden AMS) accelerator mass spectrometry facility. Together with a tuneable, high–repetitive high–power Ti:sapphire laser system developped by the project partner at the University of Mainz, an element–selective suppression of isobars by laser photodetachment will be possible. This allows the measurement of new isotopes at DREAMS and will extend the current application spectrum.

In view of the hurdles due to SARS-CoV-2 a new laboratory space in the basement of the Max–Wien–Platz 1 could be occupied and the construction of the LISEL cooler started. Until the end of 2020 the vacuum chambers and pumping system was installed and leak testing could be performed. The newly developed control system based on an industry standard PLC system by BECKHOFF was ready for operation (see Fig. 1).

The main goal of this project is to clean isobars from a keV–energies negative ion beam by laser photdetachment. To achieve this goal knowledge about the electron affinities (EA) of the atomic and molecular isobaric system is needed. The method is only applicable to systems where the EA of the ion of interest is larger than the unwanted ion. Unfortunately, sufficient spectroscopic information of negative ions is not always available. Notably of molecular negative ions experimental data is insufficient. The storage of molecular negative ions in an electrostatic low–energy storage ring can help by allowing to study the ions in its rotational ground state. An initiative to measure EAs of molecular ions was started at the Frankfurt Low–energy Storage Ring FLSR at the Goethe–University Frankfurt. The storage of the anions He^-, O^- and OH^- could successfully be achieved [1]. The installation of a laser system for in–flight photodetachment experiments is currently ongoing in collaboration with the project–partner from the University of Mainz.

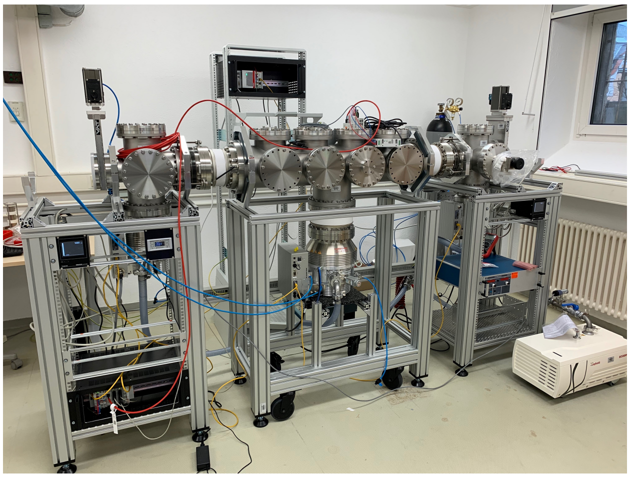

Figure 1: Image showing the LISEL cooler setup end of 2020 under vacuum and leak tested.

Together with partners from the University of Mainz and University of Gothenburg a program for measuring EAs of radioactive negative ions could be started at the radioactive ion beam facility ISOLDE at CERN. With the ion $^{128}I^-$ the EA of a radioactive ion could be measured for the first time. Furthermore, the EA of astatine, the rarest naturally occurring element on earth, has been determined experimentally for the first time. The results of this study were presented in the journal Nature Communications in 2020 [2].

This project is supported by funding from the German Ministry of Science BMBF, joint project 05K2019 – LISELatDREAMS.

References

[1] O. Forstner *et al.*, Hyp. Int. **241**, 53 (2020).

[2] D. Leimbach *et al.*, Nat. Comm. **11**, 3824 (2020).

* o.forstner@hi-jena.gsi.de

Mid-infrared laser-pulse-driven ground-state dissociation of the Helium hydride molecular ion

Philipp Wustelt[1,2], Bo Ying[1,2], Florian Oppermann[3], Saurabh Mhatre[4], Matthias Kübel[1,2], A. Max Sayler[1,2,5], Manfred Lein[3], Stefanie Gräfe[4], and Gerhard G. Paulus*[1,2]

[1]Helmholtz Institute Jena, Fröbelstieg 3, 07743 Jena, Germany; [2]Institute of Optics and Quantum Electronics, Friedrich Schiller University Jena, D-07743 Jena, Germany; [3]Institut für Theoretische Physik, Leibniz Universität Hannover, Appelstraße 2, 30167 Hannover; [4]Institute of Physical Chemistry, Friedrich Schiller University Jena, Helmholtzweg 4, 07743 Jena, Germany; [5]Benedictine College, Atchison, KS, USA

Utilizing a diatomic prototype molecular system, HeH^+, we show that mid-infrared laser pulses can drive the nuclear motion in the anharmonic potential of the electronic ground state, increasing its energy above the potential barrier and facilitating dissociation of a diatomic molecule by purely vibrational excitation.

The vibrational motion of molecules is a fundamental example of an anharmonic oscillator. When light couples directly to the vibrational degrees of freedom of the molecule, absorption of photons can transfer population from lower to higher vibrational bound or even continuum states, while remaining on the same electronic state [1] (see Fig. 1). The ground electronic surface is of enormous general importance for chemical transformations which are predominantly carried out on the ground state.

We report a direct measurement of molecular photodissociation of the HeH^+ molecule induced by purely vibrational excitation [2]. Efficient dissociation requires matching the periodicity of the driving force to the eigenfrequency of the system, which is 11.5 fs for HeH^+. Experimentally, this is realized by combining a molecular ion beam target for coincidence 3D momentum spectroscopy and mid-infrared laser pulses produced by an optical parametric amplifier. The dissociation yield for different periodicities of the driving laser is displayed in Fig. 2. The observations can be adequately described by the intuitive model of a driven anharmonic oscillator. The uneven spacing of vibrational states in the anharmonic potential results in a characteristic wavelength dependence of the dissociation probability [3].

We compared the wavelength-dependent response of the helium hydride molecular cation to both classical and quantum mechanical calculations. We find excellent agreement, which shows that the results can be interpreted applying the anharmonic oscillator analogies and removes any uncertainties through electronic excitation. Additionally, we examine the measured momenta of the fragments after dissociation. This allows us to identify the different dissociation pathways starting from different vibrational states.

Our study provides insight into the rich dynamics of anharmonic quantum oscillator systems and laser-controlled ground-state chemistry.

The authors acknowledge funding from the Deutsche Forschungsgemeinschaft (Priority program 1840, Quantum Dynamics in Tailored Intense Fields).

* gerhard.paulus@uni-jena.de

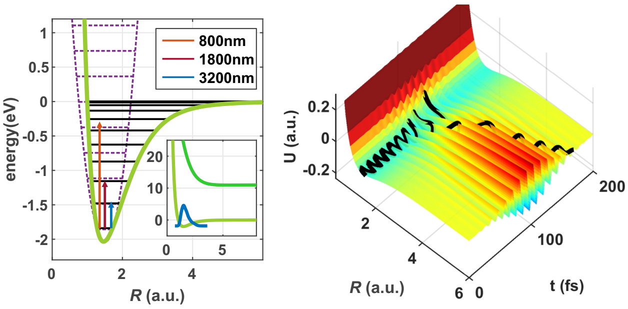

Figure 1: Laser-driven anharmonic oscillator: (a) The ground state ($X^1\Sigma^+$) of HeH^+(solid green) and the vibrational levels of the anharmonic potential of HeH^+ are compared to a harmonic potential (dashed purple). MIR photons can couple these states as consequence of the permanent dipole moment of HeH^+. The inset displays the electronic ground state and first excited state. (b) Classical trajectory model for laser-induced dissociation of HeH^+. Shown are the effective potential and the resulting motion on $X^1\Sigma^+$ for a laser field with 3.2 μm (30 TW/cm^2).

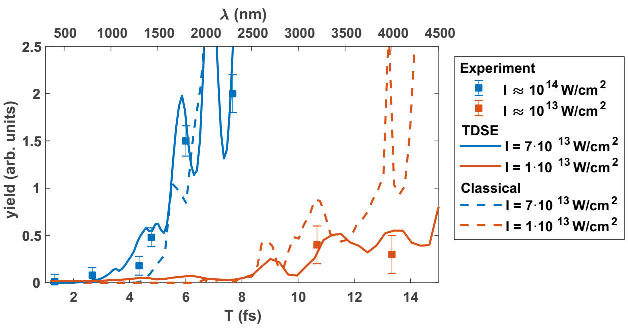

Figure 2: Frequency-dependent response of HeH^+: (a) Yield for the dissociation as function of the periodicity of the driving field and laser wavelength (upper abscissa). Measured results are displayed together with one-dimensional TDSE- and classical simulations.

References

[1] S. Chelkowski *et al.*, Phys. Rev. Lett. **65**, 2355 (1990).

[2] P. Wustelt *et al.*, Phys. Rev. Let. **121**, 073203 (2018).

[3] D. Ursrey *et al.*, Phys. Rev. A **85**, 023429 (2012).

High brightness ion sources for laser-induced ionization of metal and metalloid ions

F. Machalett*[1,2], B. Ying[1,2], P. Wustelt[1,2], V. Huth[2], L. Bischoff[3], N. Klingner[3], M. Kübel[1,2], A. M. Sayler[1,2,4], T. Stöhlker[1,2], and G. G. Paulus[1,2]

[1]Helmholtz Institute Jena, Fröbelstieg 3, D-07743 Jena, Germany; [2]Institute of Optics and Quantum Electronics, Friedrich Schiller University Jena, D-07743 Jena, Germany; [3]Helmholtz-Zentrum Dresden-Rossendorf, Bautzner Landstraße 400, D-01328 Dresden, Germany; [4]Benedictine College, Atchison, KS, USA

Gold and silicon ions emitted from high brightness liquid metal ion sources (LMIS) are used as ionic targets for strong field laser interaction with femtosecond laser beams. Field ionization processes in the field emission source at electrostatic fields of some 10 V/nm allow the generation of various metallic and metalloid ion beams with charge states such as Au^{2+} and Si^{2+}. Studying the ionization in strong femtosecond laser fields with intensities of up to 10^{16} W/cm^2, we observed for these elements charge states of up to Au^{11+} and Si^{4+}.

The application of ionic laser targets offers the opportunity to investigate interesting fundamental systems of light-matter interaction, such as He^+, H_2^+ [1] and molecules that only arise in the ion source, e.g. HeH^+ [2]. In this work we generated ion beam targets for the investigation of strong-field laser interactions with metal and metalloid ions. To increase the density of these targets we adapted a high-brightness liquid metal ion source (LMIS), originally applied in focused ion beam systems [3, 4], to an ion system for 3D coincidence momentum spectroscopy. The ions are emitted from a low melting liquid Au-Si eutectic alloy and are generated by electrostatic field evaporation and field ionization. Using an $E \times B$ filter in the beamline, several different ion species could be detected: Si^+, Si^{2+}, Au^+, Au^{2+}, Au_2^+, Au_3^+ and Au_3^{2+}. The monoatomic and noble metal molecular ions are now available to carry out studies on the ultrafast laser-induced fragmentation and ionization.

We investigated the ultrafast laser-induced ionization resulting in higher charge states after the multiple ionization of Au^+ and Si^{2+} ions. Laser intensities of up to 10^{16} W/cm^2 allow the tenfold ionization of the Au^+-ions and triple ionization of Si^{2+}-ions (see Fig. 1). These results can be explained by examining the charge-state depending electron configurations and their ionization potentials.

In addition, we applied two-color sculpted laser fields to control the double ionization process on the attosecond time scale. The observed momentum distributions depend strongly on the relative phase of the two-color laser field. This allows us to confirm the resolution of the recoil ion momenta for the detection of heavy atoms.

Our results demonstrate that the manifold of emerged experimental techniques of attosecond physics can be extended to the until now rarely explored range of various metal and metalloid targets and beyond.

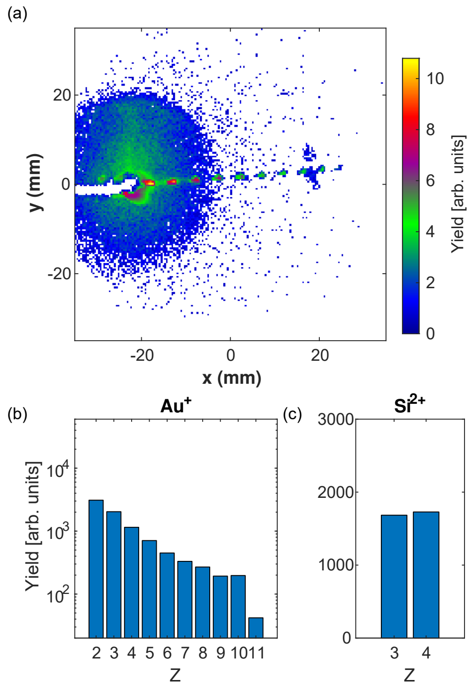

Figure 1: Multiple ionization of singly charged gold and doubly charged silicon ions: (a) Position-resolved detection of the laser-induced higher charge states after multiple ionization of Au^+ at an intensity of $3{\cdot}10^{16}$ W/cm^2. Different charge states are separated by horizontal and vertical electric fields after the laser interaction. The Au^+-beam is blocked by a Faraday cup before the detector. The structure around the Faraday cup is produced by fragments from gold molecules. (b) and (c) relative yields of different charge states for Au and Si respectively.

The authors acknowledge funding from the Deutsche Forschungsgemeinschaft (Priority program 1840, Quantum Dynamics in Tailored Intense Fields).

References

[1] T. Rathje *et al.*, Phys. Rev. Lett. **11**, 093002 (2013).

[2] P. Wustelt *et al.*, Phys. Rev. Lett. **121**, 073203 (2018).

[3] F. Machalett and P. Seidel, Focused Ion Beams and Some Selected Applications, EAP, Wiley (2019).

[4] L. Bischoff *et al.*, Appl. Phys. Rev. **3**, 021101 (2016).

* frank.machalett@uni-jena.de

Measurement of preplasma properties at the PHELIX facility

J. Hornung*[1,2,3], S. Roeder[2], J. Sieber[2,4], H. Nazary[2,4], V. Bagnoud[2], and M. Zepf[1,3]

[1]Helmholtz Institute Jena, Fröbelstieg 3, 07743 Jena, Germany; [2]GSI Helmholtzzentrum für Schwerionenforschung GmbH, Planckstraße 1, 64291 Darmstadt, Germany; [3]Friedrich-Schiller-Universität, Fürstengraben 1, 07743 Jena, Germany; [4]Technische Universität Darmstadt, Karolinenplatz 5, 64289 Darmstadt, Germany

We performed an experimental campaign at the PHELIX system at GSI to study the properties of relativistic plasmas using time-resolved reflection spectroscopy, which correlates the spectral modulation of the reflected laser pulse with the plasma scale length. To further control the interaction conditions, we implemented a plasma mirror to enhance the temporal contrast and tuned the preplasma expansion using a controlled prepulse. The created plasma was measured using side-view interferometry, which enabled the calculation of the spatial electron density distribution.

The state and properties of the plasma pre-expansion, induced by the imperfect temporal pulse profile picoseconds prior to the laser-peak intensity, remains a large uncertainty in laser-plasma interaction experiments. A measurement of the preplasma properties is a challenging task, especially if the scale length of the plasma density distribution is in the sub-micrometer range. In this regime, time-resolved reflection spectroscopy represents a promising method to determine the preplasma properties, which relies on measuring the reflected laser pulse during the interaction in a time-resolved manner. To study this method, we performed an experiment at the PHELIX laser system at GSI in Darmstadt. A schematic of the setup is visible in Fig. 1, showing the incoming laser beam, which has been focused onto a micrometer-thick target, using a F/1.4 off-axis parabola. To enhance the temporal contrast of the laser pulse we implemented a plasma mirror (PM) in the focusing beam, which results in a reduced preplasma expansion.

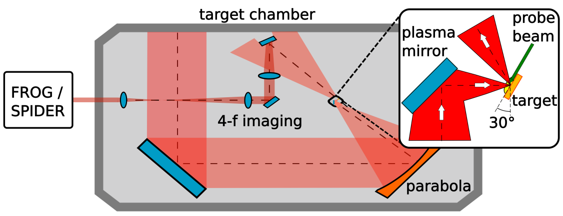

Figure 1: Experimental setup at the PHELIX system, including the plasma mirror setup (inlet) and the diagnostic beamline.

As a comparison, the PM was replaced by a mirror with a high-reflective coating to achieve a lower contrast, resulting in a stronger preplasma expansion. During the interaction, a part of the laser pulse is reflected at the critical density position, which is picked off and imaged onto the time-resolved diagnostics. These diagnostic based on "Frequency-Resolved Optical Gating" (FROG) and "Spectral Phase Interferometry for Direct Electric field Reconstruction" (SPIDER), which have been built and commissioned at our facility [1, 2], are able to measure the spectral change of the laser pulse throughout the interaction. This information can be used to gain insight into the movement of the critical density surface. Depending on the temporal contrast, both diagnostics showed a strong difference in the spectral-temporal behavior of the reflected laser pulse. The spectrum is strongly red-shifted in the presence of a more extended preplasma with a longer density scale length, whereas the spectrum is completely blue-shifted after the interaction if the PM is used.

To further vary the preplasma conditions and reach scale lengths above 1 µm, we introduced a controlled prepulse with a peak-intensity in the range of 10^{14} W/cm^2. The resulting density distribution of the preplasma was measured using side-view interferometry. The schematic setup is shown in Fig. 2, in which a frequency doubled beam was used to probe the plasma.

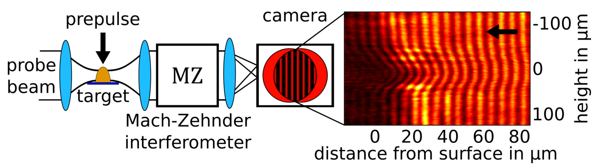

Figure 2: Setup of the side-view interferometry used to measure the preplasma expansion, created by a controlled prepulse. The black arrow indicates the incoming prepulse.

The resulting measurement, shown on the right-hand side, was used to determine the corresponding density distribution. This enables the possibility to use such a prepulse in further experimental campaigns to generate a controlled preplasma and therefore improve the study of the plasma conditions using time-resolved reflection spectroscopy.

Funding Acknowledgements: *This work has been carried out within the framework of the EUROfusion consortium and has received funding from the Euratom research and training programme 2014-2018 and 2019-2020 under grant agreement No 633053. The views and opinions expressed herein do not necessarily reflect those of the European Commission.*

References

[1] F. Wagner *et al.*, Rev. Sci. Instrum. **88**, 023503 (2017).

[2] S. Roeder, "Design of a SPIDER for time-resolved plasma characterization", Master thesis, TU Darmstadt, (2020).

* j.hornung@gsi.de

Two novel maXs detector systems for the SPARC collaboration

G. Weber*[1,2], P. Pfäfflein[1,3], F. Kröger[1,3], M. O. Herdrich[1,3], A. Fleischmann[4], D. Hengstler[4], S. Allgeier[4], M. Friedrich[4], P. Kuntz[4], C. Enss[4], and Th. Stöhlker[1,2,3]

[1]HI Jena; [2]GSI; [3]IOQ, FSU Jena; [4]KIP, RKU Heidelberg

Low-temperature x-ray detectors based on the metallic magnetic calorimeter (MMC) technology combine a broad spectral acceptance together with an energy resolution comparable to that of crystal spectrometers and an excellent signal linearity. After several years of development within the SPARC collaboration two systems based on the maXs (Microcalorimeter Arrays for High-Resolution X-Ray Spectroscopy) detector design are now available for precision x-ray spectroscopy.

Micro-calorimeters are low-temperature detectors which convert the energy of an incident particle into a temperature rise of a small absorber which is then measured, e.g. as a change in magnetization for the case of MMC detectors [1]. These detectors work at typical temperatures below 50 mK, where the relevant material properties like magnetization and heat capacity are very sensitive to small changes in temperature. In recent years, the maXs detector design was developed to meet the specific requirements of the precision x-ray spectroscopy program of SPARC [2, 3]. This detector system now features 64 pixels of MMCs that are read out via 32 SQUIDs. The area and thickness of the absorbers can be optimized for specific photon energies and desired spectral resolutions, with the caveat that increasing the absorber volume in general results in a reduced spectral resolution. There now exists a broad range of already tested absorber designs, ranging from the maXs-10 ($\Delta E \approx 2$ eV FWHM for photon energies up to 10 keV) to the maXs-200 ($\Delta E \approx 50$ eV FWHM for energies up to 200 keV).

After several iterations of test measurments and subsequent detector optimization, including adaptation of the readout electronics to the experimental environment of GSI, two maXs detector systems are now ready to be used in precision x-ray spectroscopy measurements. The first of these measurements will be experiment E138 '1s Lamb shift in U^{91+}', that is scheduled for the first half of 2021. In this report, we present a brief overview of both systems.

The first detector system is based on a Bluefors multiple-purpose cryostat that is equipped with an arm of about 60 cm length. At the end of the arm the detector array can be mounted in two different positions: along the axis of the detector arm or under 90° to it. This design enables a high degree of flexibility in positioning the detector, in particular when it is not possible to place the bulky cryostat, weighting about 350 kg, in close range to the photon source.

The second detector system features the so-called MiniMix cryostat that was developed as a very compact cryostat dedicated for the maXs detector system. This development was conducted together with Entropy Crygenics GmbH and in a reduction of a factor 4 in volume and a factor 2 in costs compared to the aforementioned system that employs the more versatile Bluefors cryostat. The second system is compact enough that the cryostat can be placed next to the photon source, thus the absorber array can be mounted inside the cryostat housing and a detector arm is not necessary.

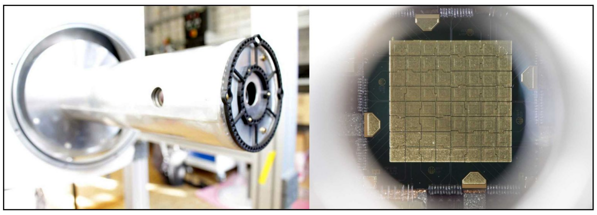

Figure 1: Left: Multiple-purpose cryostat from the company Bluefors equipped with an arm, that allows for two different orientations of the maXs detector head. Right: Photograph of the 64-pixel absorber array mounted at the end of the arm.

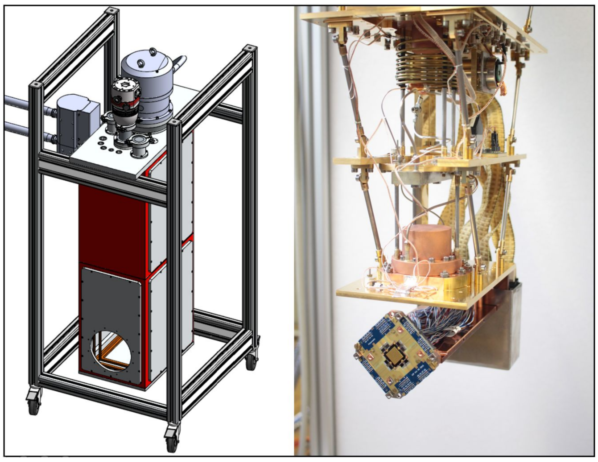

Figure 2: Left: Dedicated cryostat for the maXs detector system, developed together with the company Entropy Cryogenics. Right: Detector platform to be mounted inside the cryostat.

The authors acknowledge funding from TAB and the EU via project 2016 FGI 0017 and 2016 FGI 0037 as well as from BMBF via Verbundforschung 05P2018.

References

[1] C. Enss *et al.*, J. Low. Temp. Phys. **121**, 137 (2000).

[2] C. Pies *et al.*, Journal Low Temp. Phys. **167**, 269 (2012).

[3] S. Kraft-Bermuth *et al.*, Atoms **2018**, 59 (2018).

* g.weber@hi-jena.gsi.de

Determination of the 1s-Lamb-shift of Xe^{53+} using a maXs-200 low-temperature x-ray detector

M. O. Herdrich*[1,2,3], D. Hengstler[4], M. Keller[4], J. Geist[4], A. Fleischmann[4], C. Enss[4], T. Gassner[1,2], G. Weber[1,2], and Th. Stöhlker[1,2,3]

[1]HI Jena, Jena; [2]GSI, Darmstadt; [3]IOQ, Jena; [4]KIP, Heidelberg

Recently an experiment was conducted at the ESR storage ring of GSI aiming on the study of the x-ray emission of Xe^{54+} ions colliding with Xe atoms. The resulting x-ray radiation was recorded using a high-resolution spectrometer based on metallic magnetic calorimeter (MMC) technology. An analysis of the measured spectrum was performed in order to determine the 1s-Lamb-shift of Xe.

Cryogenic MMCs like the maXs-series detectors developed within the SPARC collaboration by the group of C. Enss at the university of Heidelberg have proven to be a valuable tool for high precision spectroscopy in atomic physics experiments. Due to their unique working principles they combine the benefits of a broad spectral acceptance with a high energy resolution of up to $E/\Delta E > 3000$ [1]. During the course of the last years, multiple experiments were performed at the ESR storage ring at GSI Darmstadt where several maXs-detectors have been deployed to record the x-ray emissions resulting from ion-atom-collisions at the ESR's internal gas-target. Because of the development of new data analysis algorithms in the past few years, data taken at the ESR in 2014 has recently been reanalyzed in order to determine the 1s-Lamb-Shift of hydrogen-like Xenon.

The experiment was conducted in April 2014 (see also [3], and [2]). A beam of Xe^{54+} ions at $50\,\mathrm{MeV/u}$ beam energy was overlapped with a Xe gas-jet and the resulting x-ray emission was observed through the $60°$ view port of the target chamber using a maXs-200 type detector. The recorded spectrum can be seen in Fig. 1. The instrumental resolution of the detector was $77\,\mathrm{eV}$ FWHM at $60\,\mathrm{keV}$ photon energy.

Due to the high atomic number of both the projectile and target as well as the low collision energy the exchange of K- and L-shell electrons between the two happens adiabatically. Subsequent, characteristic x-ray emissions stemming from the relaxation of excited states produced by the charge transfer can be observed. Besides the x-ray photons emitted from the ionized target atoms, spectral lines from several transitions into the K-shell in different charge states of the projectile ions are visible. A linear least square fit was performed correlating the transition energies of the most prominent Ly-α and -β lines with the binding energies of their initial excited states taken from theory [4]. Note, by applying this procedure the ground-state energy for $^{132}Xe^{53+}$ was determined whereby the Doppler-correction was taken into account by inclusion of the various ground

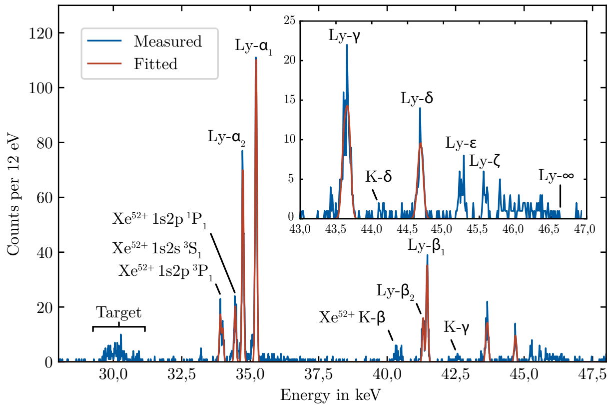

Figure 1: The plot shows the x-ray spectrum produced by the collision between Xe^{54+} ions at $50\,\mathrm{MeV/u}$ and a Xe gas-jet. It was recorded with a maXs-200 detector placed at the $60°$ view port of the ESR's internal gas-target. Displayed is the measured spectrum overlayed with the peak fits of several Lyman- and K-lines of Xe^{53+} and Xe^{52+} projectile ions.

state transitions observed. By comparing this experimental result with the prediction of the Dirac theory we find a 1s-Lamb-shift value for Xe^{53+} of $E_{LS} = 46.80\,\mathrm{eV} \pm 2.77\,\mathrm{eV}$ (preliminary results). This result is in excellent agreement with the theoretical prediction of 47.09 eV [4, 5] as well as with the result of a similar experimental study obtained by the application of a micro-calorimeter at the Livermore EBIT ion source [6].

The first proof-of-principle measurements at the GSI accelerator facility proof that maXs-type detector are able to provide an energy resolution that is almost one order of magnitude better compared to conventional semiconductor detectors. Thus, these instruments are perfectly suited for x-ray precision spectroscopy studies within the scientific program of the SPARC collaboration.

We acknowledge financial support by the European Union and the federal state of Thuringia via Thüringer Aufbaubank within the ESF project (2018 FGR 0080).

References

[1] S. Kempf *et al.*, Supercond. Sci. Technol. **28** (2015).

[2] D. Hengstler *et al.*, Phys. Scr. **T166** (2015).

[3] S. Kraft-Bermuth *et al.*, Atoms **6** (2018).

[4] P. Indelicato, p.c. (2020).

[5] V. A. Yerokhin *et al.*, J. Phys. Chem. Ref. Data **44** (2015).

[6] D. B. Thorn *et al.*, J. Phys. Rev. Lett. **103** (2009).

*m.o.herdrich@hi-jena.gsi.de

Direct Measurements of Laser Energy Absorption Under Relativistic Interaction of Femtosecond Laser Pulses with Nanowire Targets

M. S. Blümcke[1], E. Eftekhari-Zadeh*[1], Z. Samsonova[1], R. Loetzsch[1,2], I. Uschmann[1,2], M. Zapf[2], C. Ronning[3], O. N. Rosmej[4], D. Kartashov[1], and C. Spielmann[1,2]

[1]Institute of Optics and Quantum Electronics, Max-Wien-Platz 1, 07743 Jena, Germany; [2]Helmholtz Institute Jena, Fröbelstieg 3, 07743 Jena, Germany; [3]Institute of Solid State Physics, Helmholtzweg 3, 07743 Jena, Germany; [4]Helmholtzzentrum GSI-Darmstadt, Planckstr. 1, 64291 Darmstadt, Germany

It was shown recently that nanowire geometry of a solid target enables so-called volumetric heating in relativistic laser-solid interaction, resulting in generation of high density and high temperature plasmas [1]. We report here comparative results on direct measurements of laser energy absorption for solid targets of different morphology, i.e. polished bulk samples versus vertically and randomly oriented nanowires (NWs), irradiated by relativistically intense ultra-short laser pulses.

The experiment was conducted at the JETi-40 laser system [FSU, IOQ Jena], delivering laser pulses with a pulse duration of 30 fs at 800 nm. Temporal ns to ps intensity contrast of the laser pulses down to $10^{-11} - 10^{-12}$ was achieved by frequency doubling the output radiation of the laser system in a type I KDP crystal. The optical absorption of the incident laser pulses of $\sim$40 fs duration with a central wavelength of 400 nm at intensities above 10^{10} W/cm^2 was determined using an integrating sphere. Nanowires made of ZnO were grown in a bottom-up approach using the vapor-liquid-solid (VLS) technique on a 500-µm thick silicon substrate. SEM image analysis of the NW targets shows that the randomly oriented NWs have an average length of (5.57 $\pm$ 0.38) µm and an average diameter of (224 $\pm$ 39) nm, while in the case of vertically oriented NWs, the average length was (5.26 $\pm$ 0.38) µm and diameter was (778$\pm$77) nm. Polished flat ZnO samples with 500 µm thickness were used as reference targets for comparison.

The results of the total laser energy absorption of the ZnO targets with different morphologies as a function of the laser energy are shown in Fig. 1. Every point in this plot is a single laser shot. We demonstrate an almost 2-fold enhancement of absorption in both NW morphologies with an average of (79.5$\pm$1.9) % in comparison to the flat bulk sample of (45.8$\pm$1.9) %.

The observed substantially enhanced absorption in NWs is also confirmed by high-resolution X-ray emission spectroscopy. K-shell X-ray emission lines (Fig. 2) revealed that the He-like resonance line emission from highly ionized Zn (Zn^{28+}) is only present in the case of NWs, indicating the presence of a hot and dense plasma resulting from higher laser energy absorption in NWs. Our results can be used to benchmark theoretical models and numerical codes for the relativistic interaction of ultrashort laser pulses with nanowire targets.

* e.eftekharizadeh@uni-jena.de

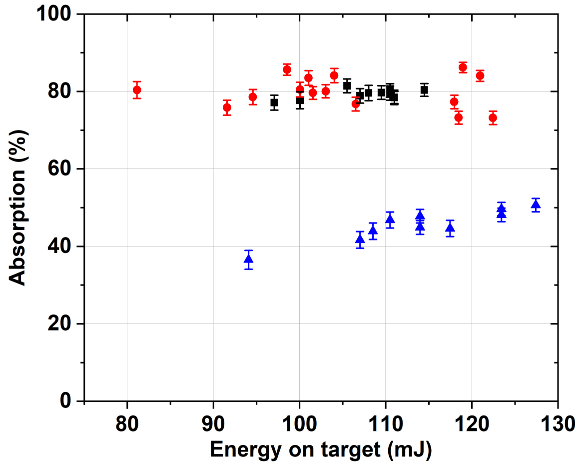

Figure 1: Laser energy absorption for polished targets (blue triangles), vertically (black squares), and randomly oriented (red circles) NWs at the incident laser intensity of $\geq 10^{19}$ W/cm^2.

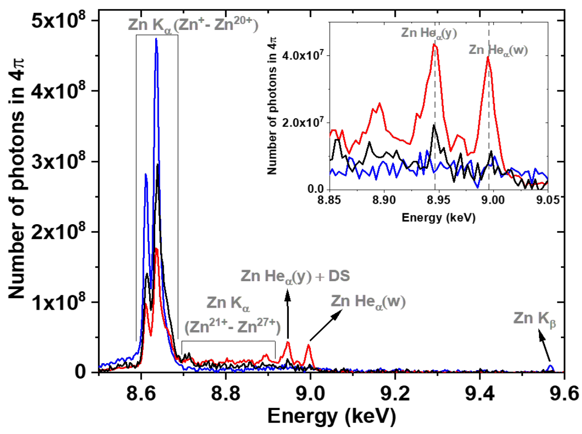

Figure 2: The X-ray emission spectra measured from the polished (solid blue line), randomly oriented NWs (solid red line), and vertically oriented NWs (solid black line) ZnO targets. The inset shows the zoomed spectral range of 8.8-9.1 keV in the vicinity of He-like K-shell emission lines.

References

[1] M. A. Purvis *et al.*, Nature Photonics **7**, 796 (2013).

Thermal load on BNA crystal during THz generation with NIR laser pulses

Y. Li*[1], L. Du[1], F. Roeder[1], L. J. Jahn [1], and A. Gopal[1,2]

[1]Institut für Optik und Quantenelektronik, Max-Wien-Platz 1, 07743 Jena, Germany; [2]Helmholtz Institute Jena, Fröbelstieg 3, 07743 Jena, Germany

We investigated the thermal load on the organic crystal BNA during THz radiation generation with 800 nm laser pulses delivered at 1 kHz repetition rate. We measured the thermal load by imaging the crystal with a thermal camera and quantifying heating and cooling times for three different substrate materials.

For many real-life applications, compact THz systems operating with high average power driven by table top laser systems are required. The best organic crystal based THz sources driven by $800\,\mathrm{nm}$ lasers employ BNA crystals for terahertz generation [1]. However until now the repetition rate of the laser system pumping those crystals were kept to $100\,\mathrm{Hz}$ to limit the thermal load on the crystal for optimum operation conditions [2]. This provided high peak power but a low average power. In order to increase the average power the thermal load on the organic crystal needs to be reduced. However, organic crystals employed for THz generation have very low heat capacity and thermal conductivity and many are novel materials still lacking complete characterization. From laser physics it is known that bonding the crystals onto substrates with higher thermal conductivity can dissipate the heat and thereby lower the thermal load for enabling their use at high average powers of the laser pulse. As a continuation of our earlier studies we investigated the thermal load on BNA crystal at kHz repetition rates to probe their potential to deliver high average powers. To this extent we investigated three substrate materials, glass, sapphire and diamond respectively and recorded at the rise in temperature of the crystal for increasing laser fluences as shown in Figure 1.

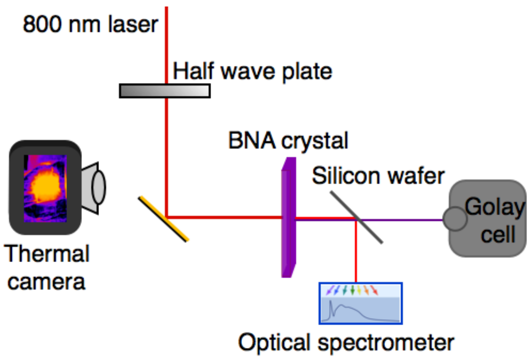

Figure 1: Schematic of the experimental set up.

At first, we compared the generated THz yield from three different samples. Figure 2a shows the THz yield as a function of input laser power. It suggests that the THz yield

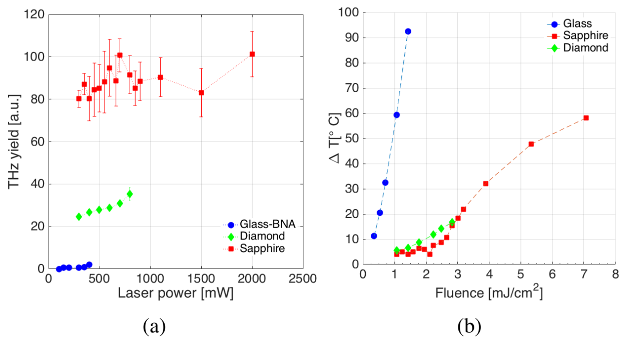

Figure 2: a) THz yield is presented as a function of input laser power. b) Rise in temperature at the center of the crystal.

from the BNA crystal mounted on sapphire substrate is more than four times higher than diamond substrate and an order of magnitude higher than glass substrate for same input laser power. Also at this repetition rate, the THz generation process saturates faster than low repetition rates [1]. It is also evident that sapphire and diamond substrates can withstand higher laser fluence compared to glass before thermal damages become visible. Figure 2b presents the rise in the peak temperature at the centre of the crystal for increasing laser power. Even below $1.4\,\mathrm{mJ/cm^2}$ or below $400\,\mathrm{mW}$, the crystal temperature reaches melting point for glass substrate while sapphire and diamond bonded crystals remain close to room temperatures. It can also be seen that despite the low temperatures compared to diamond, THz yield from sapphire bonded BNA crystal is higher.
We have presented here a preliminary study on the influence of three well known substrate materials for bonding BNA crystals to generate THz radiation at high average powers of the pump lasers. Even with a low laser fluence like $350\,\mathrm{mW}$ the temperature of the BNA crystal bonded onto the glass substrate rises by $60°\mathrm{C}$ while the one employing sapphire and diamond rises less than $10°\mathrm{C}$. Already with 400mW input laser power causes a temperature rise above $90°\mathrm{C}$ bringing it close to the melting point eventually resulting in complete melting of the substrate. Among the three substrates sapphire has the lowest thermal load and the highest THz yield.

References

[1] F. Roeder *et al.*, Opt. Express **28**, 36274 (2020).

[2] M. Jazbinsek *et al.*, Appl. Sci. **9**, 882 (2019).

*y.li@uni-jena.de

Complex refractive index measurements of optical materials using single-shot THz spectroscopy

L. Du*[1], F. Roeder[1], Y. Li[1], and A. Gopal[1,2]

[1]Institut für Optik und Quantenelektronik, Max-Wien-Platz 1, 07743 Jena, Germany; [2]Helmholtz Institute Jena, Fröbelstieg 3, 07743 Jena, Germany

A single shot THz detection system has been developed and installed at the JETI 40 laser system for linear and nonlinear spectroscopic and imaging applications. The scheme was employed to characterize a new THz source and to improve the laser to THz conversion efficiency by a factor of 4. Subsequently they were employed to measure the complex refractive index of window materials in the THz range.

In the last decades THz radiation has attracted huge interest due to the availability of compact, broadband and tunable sources enabling real life applications. Compact systems based on organic crystals accelerated this growth thanks to their simple experimental schemes and phase matching at commonly available laser wavelengths. With the increase in THz pulse energy it is also important to understand the optical properties of materials in the THz range for efficient beam control and guiding. In fact, previous studies have shown that current THz sources can create intense pulses which can induce optical nonlinearities in the medium as they propagate through it [1, 2].

For material characterization conventional time domain spectrometer (TDS) either in the reflection or transmission mode is employed. In a TDS system terahertz and short optical pulses enters collinearly in an electro-optic crystal and sampling technique is employed to read out the THz pulse. At high energies single-shot spatial encoding technique to obtain the complex THz field. We employed this single-shot spectroscopy to detect the THz pulses and characterize different window materials.

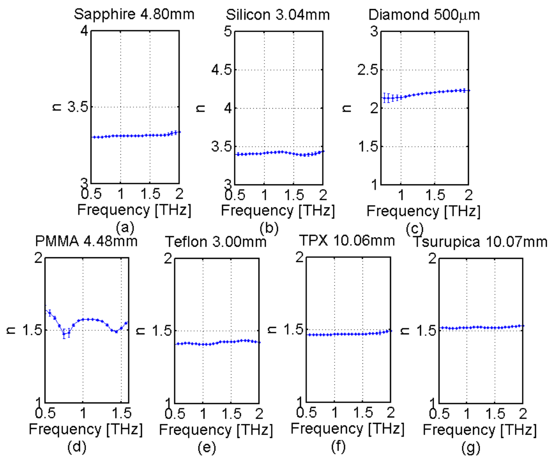

Figure 1: Spectrally resolved refractive indices of the window materials.

We generated THz radiation by shining 800 nm laser pulses from the JETI laser onto BNA crystal mounted on sapphire substrate. At first the THz radiation was characterized without the sample ($\tilde{E}_{ref}$). Thereafter free standing windows were placed in the collimated THz beam path and the complex electric field of the transmitted THz pulse ($\tilde{E}_{ref}$) was measured. The refractive index and the absorption coefficient were extracted using

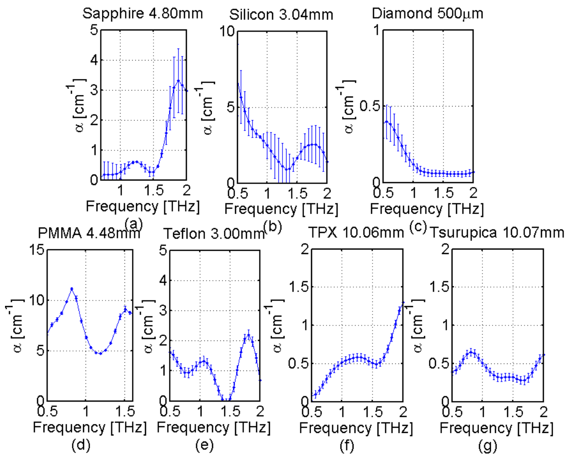

Figure 2: Spectrally resolved absorption coefficient of the window materials.

$$\tilde{E}_{sample}/\tilde{E}_{ref} = e^{\frac{-\alpha}{2}d+ik[(n-1)d-\Delta z]}\,, \qquad (1)$$

where α is the absorption coefficient and d is the sample thickness. Using the extracted refractive index and absorption coefficient α, the dielectric constants were calculated. The refractive indices and absorption coefficient measured are close to the reference data obtained using EO sampling schemes, thereby demonstrating the suitability of single-shot spectroscopy for material characterization [3].

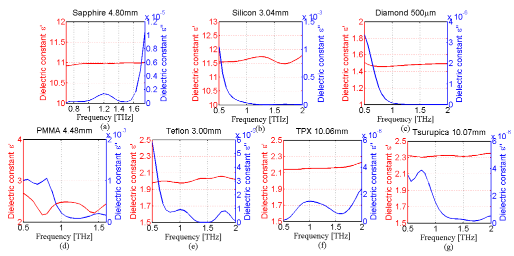

Figure 3: The real and imaginary components of the dielectric constants of the window materials.

References

[1] A. Woldegeorgis *et al.*, J Infrared Milli Terahz Waves **39**, 667 (2018).

[2] M. Sajadi *et al.*, Opt. Express **23**, 28985 (2015).

[3] L. Du *et al.*, submitted to J Infrared Milli Terahz Waves.

* lufan.du@uni-jena.de

Interaction of FEL-Radiation with Stored Ions in a Penning Trap

M. Kiffer*[1], S. Ringleb[1], N. Stallkamp[1,3], B. Arndt[5], S. Kumar[4], G. G. Paulus[1,2], W. Quint[3,6], B. Reich[6], Th. Stöhlker[1,2,3], and M. Vogel[3]

[1]Friedrich-Schiller-Universität, Jena; [2]Helmholtz Institute Jena; [3]GSI, Darmstadt; [4]Inter-University Accelerator Centre, New Delhi; [5]Goethe-Universität, Frankfurt; [6]Ruprecht Karls-Universität, Heidelberg

The goal of the High-Intensity-Laser-Ion-Trap-Experiment (HILITE) is to investigate the interaction of stored highly-charged ions with high-energy or high-intensity radiation. We will review the recent experiment at FLASH, present the results and give an outlook to planned modifications based on the experience at FLASH.

The development of the free-electron laser allows the creation of intense laser beams with photon energies in the XUV to X-ray regime. This opens the possibilities for laser experiments with highly charged ions. In particular, the inner shells like the K- or L-shell can be accessed. The HILITE Penning trap setup is designed to prepare a pure target of highly charged ions in a defined state [1].

In spring we have performed our first beam time at the FLASH2 free-electron laser at DESY in Hamburg. The goal of this beam time has been to measure two-photon ionisation of hydrogen-like C^{5+} and lithium-like O^{5+}. Both species offer a single active electron that can be addressed by both two- and three-photon ionisation, depending on the applied photon energy. The ions have been created in an EBIT that is part of the transportable setup. After creation the ions have been decelerated and stored in the trap. The alignment of the laser beam with the ion cloud has been performed using the measurement of the one-photon ionisation of C^{2+}.

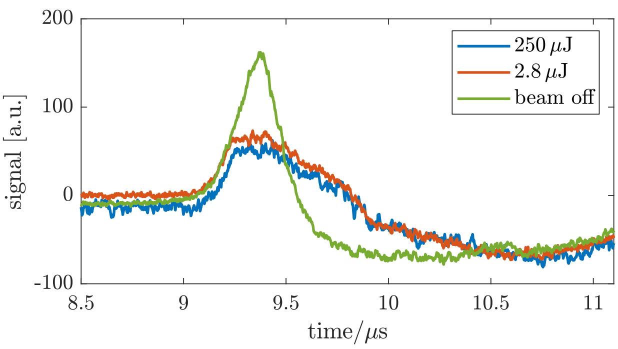

Figure 1: Measurement of the ionisation of stored C^{2+}. The green curve shows the signal without irradiation. Blue and red show the signal after irradiation with 400 laser pulses for two different total pulse energies. For both signals the measured background signal was subtracted. The loss of signal proves that C^{2+} was ionised and overlap was achieved.

One can see in figure 1 that the FLASH2 beam has had a significant impact on the stored ion cloud. The signal has been much lower which means that the C^{2+}-ions have been ionised. This indicates that an overlap between beam and ion cloud has been achieved. The higher charge state could not be detected.

Due to unexpected bad vacuum conditions (1×10^{-8} mbar instead of 1×10^{-10} mbar) the lifetime of the stored ions has been two orders of magnitude to short. Hence, the lifetime of highly charged ions has been of the order of one second and they could not be stored and irradiated for a long time. Additionally, the amount of background ions due to background laser ionisation has been increased due to the high pressure. This has led to significant overlap between background ions and ions of interest. Thereby we could not verify any multi-photon ionisation process of C^{5+} and O^{5+}.

In order to decrease the amount of residual gas from the ambient, we have included apertures with a diameter of 4 mm on either side of the trap which is sufficiently large to focus the FEL inside the trap centre. These apertures can be seen in figure 2. We have been able to trap ions with these new apertures successfully.

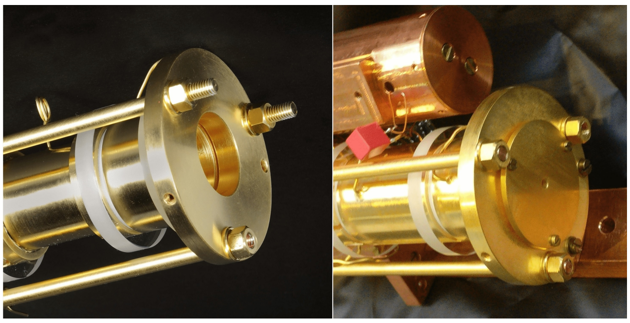

Figure 2: Picture of the trap without (left) and with the apertures (right). The apertures are used to improve the vacuum conditions in the trap.

For future experiments with strongly-focussed laser beams we have developed a new trap with an aperture of 4 mm and an overall length of only 67 mm. Performed simulations shows a good performance in ion capture capability. This system is currently under construction and will be used in spring 2022 for our second beam time at the JETi laser facility in Jena. During this beam time we will focus on the interaction of high-intensity laser beams with stored ions.

References

[1] S. Ringleb *et al.*, Phys. Scr. **2015**, 014067 (2015).

*markus.kiffer@uni-jena.de

Resonant photoexcitation experiments with PolarX-EBIT at synchrotron light sources

S. Bernitt*[1,2,3], S. Kühn[2], R. Steinbrügge[4], M. Togawa[2], C. Shah[5,2], P. Micke[6], J. Stierhof[7], M. Leutenegger[5], N. Hell[8], J. R. Crespo López-Urrutia[2], and Th. Stöhlker[1,3]

[1]HI Jena, Fröbelstieg 3, 07743 Jena, Germany; [2]MPI für Kernphysik, Saupfercheckweg 1, 69117 Heidelberg, Germany; [3]IOQ, Friedrich-Schiller-Universität Jena, Max-Wien-Platz 1, 07743 Jena, Germany; [4]DESY, Notkestraße 85, 22607 Hamburg, Germany; [5]NASA GSFC, 8800 Greenbelt Road, Greenbelt, Maryland 20771, USA; [6]PTB, Bundesallee 100, 38116 Braunschweig, Germany; [7]Dr.-Karl-Remeis-Sternwarte and ECAP, Sternwartstraße 7, 96049 Bamberg, Germany; [8]LLNL, 7000 East Avenue, Livermore, California 94550, USA

The resonant excitation of electronic transitions in trapped highly charged ions with x-ray photon beams was studied in multiple experiments with the compact electron beam ion trap PolarX-EBIT at beamlines P01 and P04 of the PETRA III synchrotron light source.

The PolarX-EBIT is equipped with a novel off-axis electron gun, which provides the monoenergetic electron beam used for ionization and trapping of highly charged ions, while allowing the synchrotron photon beam to pass through the apparatus. The beam is axially overlapped with the prolate cloud of trapped ions [1], as illustrated in figure 1. By recording x-ray fluorescence spectra from the ions for different synchrotron photon energies, it is possible to measure transition energies, relative rates, and line shapes with high accuracy. This has applications in fundamental atomic physics [2] and laboratory astrophysics.

Earlier experiments provided atomic data for high charge states of oxygen, which revealed a systematic shift of the K-shell Rydberg spectrum of molecular O_2 compared to previous literature values [3]. This has demonstrated how electronic transitions in few-electron ions can serve as accurate, reproducible, and widely employable x-ray energy references. Experiments at beamlines P04 and P01 were carried out to further explore this field of application. At P01, repeated measurements of $1s$-$3p$ transitions in different charge states of Krypton, performed simultaneously with measurements of the nuclear ^{57}Fe Mössbauer transition in a separate setup using the same photon beam, revealed long-term instabilites of the P01 monochromator, which for now limit the accuracy of spectroscopic measurements. This also led to the reevaluation of data from previous measurements.

The ratio of oscillator strengths of two key soft x-ray $2p$-$3d$ transitions, called 3C and 3D, in Fe^{16+} ions has consistently exhibited a disagreement between astrophysical observations and laboratory measurements on one side, and theory on the other. This problem was exacerbated by a recent measurement with PolarX-EBIT [4]. New experiments were conducted at P04, after technical upgrades and implementing new measurement schemes, which allowed to reach count rates, signal-to-background ratios, and resolving powers sufficient to directly measure the natural linewidths of 3C and 3D. Data analysis is still ongoing, but preliminary results already uncovered previously unknown systematic effects, which could reconcile experiment and theory.

*s.bernitt@hi-jena.gsi.de

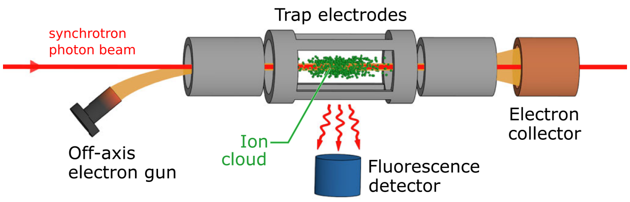

Figure 1: Setup for spectroscopy with trapped ions by detection of resonantly excited fluorescence.

In another experiment, synchrotron photons were used to probe the populations of neon and iron ions in high charge states, distinguishing between ions in the ground state and various excited metastable states. These metastable states were populated via electron impact. The well-defined conditions in the EBIT make these measurements a valuable benchmark for atomic structure theory and plasma models.

Additionally, the PolarX-EBIT has been equipped with new ion optics elements. Ions can now be extracted from the trap and detected with a channeltron, without obstructing the beam axis. First test measurements were successful. In the future, this will make the detection of resonant photoionization processes possible, expanding the capabilities of PolarX-EBIT to provide atomic data for x-ray astrophysics.

The PolarX-EBIT was funded by BMBF through project 05K13SJ2 and was supported by MPG and PTB. Part of this work was performed by LLNL contributors under contract DE-AC52-07NA27344 and was supported by NASA grants to LLNL.

References

[1] P. Micke *et al.*, Rev. Sci. Instrum. **89**, 063109 (2018).

[2] M. Togawa *et al.*, Phys. Rev. A **102**, 052831 (2020).

[3] M. Leutenegger *et al.*, Phys. Rev. Lett. **125**, 243001 (2020).

[4] S. Kühn *et al.*, Phys. Rev. Lett. **124**, 225001 (2020).

S-EBIT: Status Report

T. Morgenroth*[1,2,3], S. Trotsenko[1,2], R. Schuch[4], and T. Stöhlker[1,2,3]

[1]Helmholtz Institute Jena, Fröbelstieg 3, 07743 Jena, Germany; [2]GSI Helmholtzzentrum für Schwerionenforschung GmbH, Planckstraße 1, 64291 Darmstadt, Germany; [3]Friedrich-Schiller-Universität Jena, Fürstengraben 1, 07743 Jena, Germany; [4]University of Stockholm, Frescativägen, 114 19 Stockholm, Sweden

The S-EBIT II is a part of the HI-Jena S-EBIT facility. It contains two liquid-helium free, cryogenic electron beam ion traps, based on the Stockholm EBIT [1]. The S-EBIT facility provides ions and photons for SPARC/FAIR and HI-Jena R&D projects and experiments. Here, the S-EBIT II is being commissioned with the goal of reaching the highest charge states of high-Z ions.

The support frame of the S-EBIT II was completly renewed in order to provide sufficient maintenance access and therefore prevent a high risk in damaging sensitive parts, which had to be disassembled to reach the inner parts. The EBIT is now mounted on two different rail systems, which grants access to either the main chamber or one of the two side towers, containing the electron gun and the collector, whithout the need of disassembling the EBIT completely (compare Fig. 1).

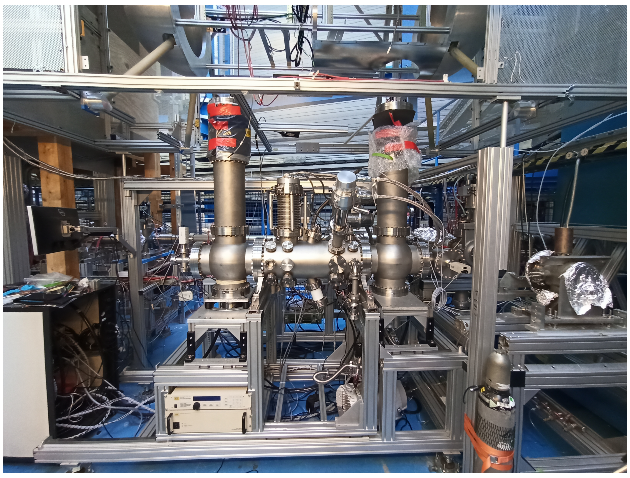

Figure 1: S-EBIT II Setup with the new support frame. The left tower includes the electron gun, the right tower the electron collector. The intermediate main chamber includes multiple view ports around the ion trap region.

During previous magnet tests, our high temperature superconductors (HTS) could not sustain the highest currents when the magnet was operating at its limits. In order to prevent possible breakdowns, a second coldhead was integrated into the system that provided additional cooling power at the temperature shield as well as at the HTS. The internal connection between the coldhead and the temperature shield, as can be seen in Fig. 2, is done by coupling a multiple layer copper ribbons, which on one hand provides a good thermal connection and at the same time vibrationally decouples the coldhead from the internal setup, which is of a very high importance for the future experiments with ion laser interaction inside the EBIT, where overlapping the beams has to be effectively provided. In addition, all electrical cppper connection wires to the 4K stage were exchanges with manganin wires in order to minimize the thermal load onto the superconducting magnet and thus enabling a very reliable operation of the EBIT.

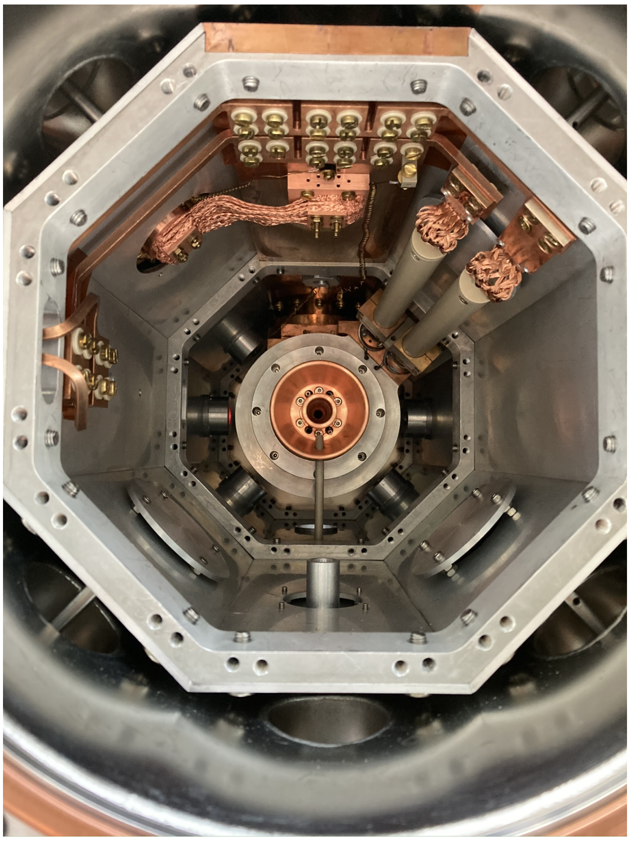

Figure 2: View inside of the S-EBIT II temperature shield. On top is the connection between the newly installed coldhead and the temperature shield with multiple layer copper ribbons.

In a close collaboration with the electrical departement of GSI, the safety systems for the high-voltage cage of the S-EBIT II have been successfully installed and commissioned. Currently, the power supplies and the controll modules for the electron gun and collector are being installed for further commissioning.

*t.morgenroth@hi-jena.gsi.de

References

[1] R, Schuch et al., JINST5, C12018 (2010).

First DR experiments at CRYRING@ESR

E. B. Menz*[1,2], M. Lestinsky[2], S. Fuchs[3], W. Biela-Nowaczyk[4], A. Borovik, Jr.[3], C. Brandau[1,3], S. Schippers[3], and Th. Stöhlker[1,2]

[1]Helmholtz Institute Jena, Fröbelstieg 3, 07743 Jena, Germany; [2]GSI Helmholtzzentrum für Schwerionenforschung, 64291 Darmstadt, Germany; [3]I. Physikalisches Institut, Justus Liebig University Giessen, 35390 Germany; [4]Jagiellonian University, Institute of Physics, Poland

In 2020 the first DR measurements were performed at CRYRING@ESR since its move from Stockholm. The experiments were conducted in merged-beam configuration in the CRYRING electron cooler where the new setup includes two particle detectors for counting of recombination products with different mass-to-charge ratios and a dedicated data acquisition system.

Dielectronic recombination (DR) is an established method for probing the energy levels of deeply bound electrons. It facilitates spectroscopy of heavy, highly-charged ions (HCIs) that provide access to effects like strong-field QED, hyperfine interactions and isotopic shifts. In addition DR experiments yield absolute rate coefficients which are vital for determining the charge state balance in plasma modelling. During its Stockholm years, CRYRING and its electron cooler hosted many DR experiments which greatly benefitted from the excellent vacuum conditions and ultracold electron beam [1]. In Darmstadt, the GSI accelerator complex is able to provide intense beams of previously inaccessible ion species which we will use to continue this tradition of DR measurement with ultra-high precision.

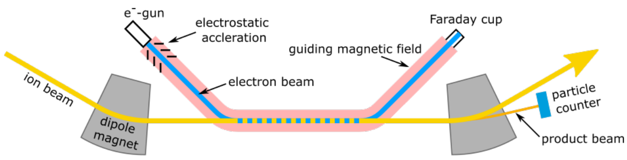

Figure 1: Experiment setup at the electron cooler.

In merged-beam DR experiments the electron cooler is used both to reduce the momentum spread of the ion beam (”cooling”) and as an electron target. For the measurement the electron energy is detuned from the cooling value by changing the acceleration voltage. In this way an energy range in the ions centre-of-mass system can be scanned and the downcharged ions produced in collisions at variable relative collision energy are detected with a particle counter installed behind the next downstream dipole magnet (see Fig. 1). Both the detuning and the data acquisition were synchronously controlled by a dedicated setup.
Besides injection from the GSI accelerator chain, a local injector can supply a range of ion species from a local source for both testing and experiments. After the installation of a new ECR ion source, Ne^{7+} was chosen for tests of the DR measurement setup prior to scheduled experiments to improve our understanding of the electron beam temperatures of the electron cooler and to commission our experiment controls. Ne^{7+} is a Li-like system with low-energy DR resonances associated with 2s → 2p core excitations. Data for this system is available both from AUTOSTRUCTURE calculations and from a previous measurement in Stockholm using the same electron cooler [2]. A YAP:Ce scintillation detector was used for the Ne^{7+} test run took place in May 2020 and provided benchmark data for the overall system performance. It also demonstrated an undegraded resolution compared to the previous measurement. This not only confirms that electron beam production at the cooler is intact after the move from Stockholm, but also proofs that our new experiment electronics are capable of delivering high-resolution DR spectroscopy, a comparison of our results with the data from [2] is shown in Fig. 2.
In preparation for experiments on HCIs, Pb^{78+} ions were injected via the full accelerator chain and stored as well as cooled successfully. During this test run a Rinn-type channel electron detector [3] for counting heavy, highly-charged recombination products was tested for the first time.
The activities of the past year have shown the readiness of both CRYRING@ESR and of our DR setup and we are looking forward to future DR beamtimes ranging from spectroscopy of highly charged ions to studies of astrophysically relevant systems, including three scheduled experiments (E131, E140 and E153).

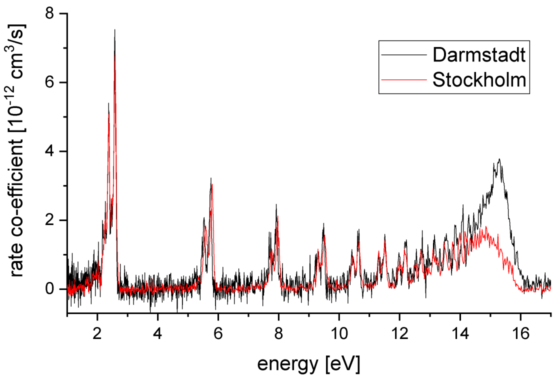

Figure 2: Comparison between the Ne^{7+} DR measurements performed at CRYRING in Stockholm and at GSI.

References

[1] S. Schippers *et al*, Nucl. Instrum. Methods **305** (2015)
[2] S. Boehm *et al*, Astronomy & Astrophysics **437** (2005)
[3] K. Rinn *et al*, Rev. Sci. Instrum. **53** (1982)

* e.menz@hi-jena.gsi.de

Preparation of the 1s Lamb shift measurement in U^{91+}: Data Acquisition and Online Analysis

F. M. Kröger*[1,2,3], G. Weber[1,3], B. Löher[3], U. Spillmann[3], S. Linev[3], J. Adamczewski-Musch[3], and Th. Stöhlker[1,2,3]

[1]HI Jena, Germany; [2]IOQ Jena, FSU Jena, Germany; [3]GSI, Germany

We report on the preparation of the data acquisition system for experiment E138 "1s Lamb shift in U^{91+}" as well as on the development of a tool for visualization and remote monitoring of live experimental data.

The goal of the upcoming experiment is the measurement of the 1s Lamb shift in hydrogen-like uranium with a precision of 1 eV or better to be able for the first time to test second-order quantum electrodynamic (QED) contributions in the regime of extreme field strengths. To this purpose we will employ novel low-temperature detectors of the maXs-type [1], which in the energy range of interest ($\approx$ 100 keV) are able to provide an improvement in spectroscopic resolution of about one order of magnitude compared to standard semiconductor x-ray detectors.

However, to reach the high resolution it is necessary to perform an offline analysis involving sophisticated pulse shape algorithms and various corrections to the detector signals. This requires to read out and store the complete trace of the detector pulses instead of relying on the output of analog electronics or simple pulse shape analysis at the frontend electronics for signal processing as was done in previous experiments. To this purpose we set up a new DAQ system (see figure 1 for the schematic working principle) based on SIS3316 16-bit digitizers that we integrated in the MBS-based data acquisition (DAQ) infrastructure of GSI [2]. After the digitized pulses are read out, subsequent analysis of the raw data is performed both in a live mode with fast algorithms and also in offline mode with more sophisticated analysis routines.

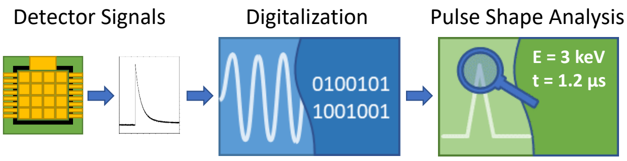

Figure 1: Schematic working principle of the DAQ. The data processing of the raw pulse in terms of energy and time information is all performed by software.

For the upcoming experiment we also plan to exploit for the first time the time resolution of the maXs detectors to enable x-ray spectroscopy in coincidence with the detection of charge-changed ions by a particle detector downstream of the interaction region. This measurement technique is well established with conventional semiconductor detectors and the associated common DAQ systems, but was never demonstrated for the novel maXs detector. To this purpose we will also digitize the particle detector signal and analyse it together with the maXs pulses. For this task our DAQ system is designed around four SIS3316 16-bit digitizer from Struck Innovative Systeme [3]. These versatile VME-based cards provide high resolution digitizer/ADC chips and have 16 analog input connectors each, so that two modules with a total of 32 channels will be dedicated to one of the maXs detectors, as its 64 pixels are sharing in pairs one output cable (using either positive or negative signals per pixel). The sampling rate per channel is 125 Megasamples per second.

In addition, we report on the development and implementation of an web-based visualization tool to display live experimental data (by Linev, Adamschewski-Musch, Spillmann) [4]. This tool, which was mainly motivated by the exceptional situation for travel and on-site participation in experiments at GSI due to the pandemic, will enable remote monitoring of measurements as well as a fast dissemination of experimental data within the SPARC collaboration. Using the THttpServer class allows to provide remote http access to running ROOT-based applications. It is based on Civetweb embeddable http server and provides direct access to all objects registered to the server. The support of FastCGI allows to integrate it with standard web servers like Apache or lighttpd. A generic user interface was implemented using JavaScript ROOT, so that one can display and monitor objects available on http server with any modern web browser. The use of THttpServer in the framework of the GSI data analysis program go4 [5] to monitor and modify analysis objects will allow to configure and control our go4 analysis remotely during the experiment via http.

The authors acknowledge funding from TAB and the EU via project 2016 FGI 0017 and 2016 FGI 0037 as well as from BMBF via Verbundforschung 05P2018.

References

[1] C. Pies *et al.*, Journal Low Temp. Phys. **167**, 269 (2012).

[2] N. Kurz and J. Adamschewski-Muschm, `https://www.gsi.de/en/work/research/experiment_electronics/data_processing/data_acquisition/mbs` (as of 2021).

[3] `https://www.struck.de/sis3316.html` (as of 2021).

[4] S. Linev, B. Bellenot, `https://jsroot.gsi.de/`, (as of 2021).

[5] J. Adamschewski-Musch, S. Linev, `https://www.gsi.de/en/work/research/experiment_electronics/data_processing/data_analysis/the_go4_home_page`, (as of 2021).

* felix.kroeger@uni-jena.de

Preparation of the 1s Lamb shift measurement in U^{91+}: Experimental setup

P. Pfäfflein*[1,3], G. Weber[1,2], F. M. Kröger[1,3], M. O. Herdrich[1,3], T. Köhler[3], A. Fleischmann[4], D. Hengstler[4], and Th. Stöhlker[1,2,3]

[1]HI Jena; [2]GSI, Darmstadt; [3]IOQ, FSU Jena; [4]KIP, RKU Heidelberg

The upcoming investigation of the 1s Lamb shift in U^{91+} at the CRYRING@ESR will use two maXs-type detectors for x-ray spectroscopy, that outperform conventional semiconductor detectors by an order of magnitude in terms of spectral resolution. However, the low working temperature of about 20 mK requires a cumbersome cryogenic infrastructure that results in a heavy weights of up to 500 kg per detector. We report on the experimental setup including dedicated support structures for fine positioning of the detectors in front of the view ports.

Spectroscopy of the light emitted by electronic transitions of few-electron ions along the isoelectronic sequence is a well established method for probing our understanding of the atomic energy levels. Of particular interest is the 1s Lamb shift of hydrogenlike high-Z ions as it provides insights into bound-state quantum electrodynamics in the presence of extreme field strengths. For the highest stable element, the 1s Lamb shift is of the order of 464 eV with second-order QED corrections being predicted to contribute about 1.4 eV [1]. This is significantly below the uncertainty range of 4.6 eV of most precise measurement that was performed using standard Ge(i) x-ray detectors for spectroscopy of the Lyman transitions of U^{91+} at the ESR electron cooler [2]. The upcoming experiment E138, which will be performed by the SPARC collarboration, adapts the setup of the previous measurement to the experimental environment at the electron cooler of CRYRING@ESR (see fig. 1), while exploiting the superior spectral resolution of the metallic magnetic calorimeters of the maXs-type [3] to improve the experimental accuracy down to the < 1 eV range.

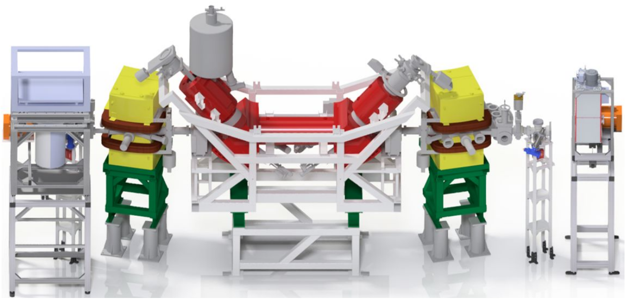

Figure 1: 3D drawing of the experimental setup at the 0° and 180° view ports of the electron cooler of CRYRING@ESR.

For exact and reproducibly positioning of the heavy cryostats of up to 500 kg, two dedicated support structures were built and tested. These allow x-y-z positioning of the maXs detectors and in addition quick switching between this detector system and conventional Ge(i) detectors that are placed on the same support (see left side of fig. 2). This enables remote switching between large-area Ge(i) detectors and their capability to provide online spectra and the maXs detector which offer superior resolution but require extensive data post processing. The first test of the entire assembly has been performed in August 2020 in Jena (right side of fig. 2). Lead shielding bricks have been used to simulate the weight of the cryostat. The tests were sucessful, so the design proved its ability to carry and 3D position the detector using ball screws driven by stepper motors. Both support frames have been shipped to GSI.

Figure 2: Left: 3D model of the support strucutre with maXs detector and conventional Ge(i) detector. Right: Detector assembly with lead bricks to simulate the weight of the detector.

We acknowledge financial support by the EU and the state of Thuringia via TAB within the ESF project (2015 FGR 0094) as well as by BMBF for APPA R&D, project number 05P19SJFAA.

References

[1] V. A. Yerokhin and V. M. Shabaev, J. Phys. Chem. Ref. Data **44**, 033103 (2015).

[2] A. Gumberidze *et al.*, Phys. Rev. Lett. **94**, 223001 (2005).

[3] S. Kraft-Bermuth *et al.*, Atoms **2018**, 59 (2018).

* p.pfaefflein@hi-jena.gsi.de

Accurate modeling of radiative recombination into high-Z ions at the CRYRING@ESR electron cooler

Binghui Zhu*[1], Günter Weber[2], and Thomas Stöhlker[2]

[1]Helmholtz Institute Jena, Fröbelstieg 3, 07743 Jena, Germany; [2]Friedrich-Schiller-Universität Jena, Institut für Optik und Quantenelektronik, Jena, 07743, Germany; [3]GSI Helmholtzzentrum für Schwerionenforschung GmbH, Darmstadt, 64291, Germany

We present detailed collisional radiative recombination (RR) modelling to enable a detailed understanding of the x-ray spectra of highly charged Uranium ions observed at the electron cooler of CRYRING at a beam energy of 10 MeV/u. The spectra permit the identification of spectral lines from H-like ions, leading to the re-interpretation of the previously known Lyman and Balmer lines originated from the prevailing cascade feeding up to higher Rydberg state, and reveal the subtle features in the x-ray spectrum arising from the importance of forbidden transitions between excited states.

Highly charged ions of heavy elements represent a crucial field of atomic physics that offers numerous challenges from both theoretical and practical viewpoints. Their basic atomic characteristics, such as energy levels and radiative transition probabilities, are dominantly influenced by relativistic effects or even by quantum-electrodynamics (QED) in the extremely strong field regime, which often bring about new spectral patterns that are remarkably different from the spectra of light elements [1]. To be more specific, the forbidden radiative transitions in such system are enhanced by many orders of magnitude relative to "allowed" electric-dipole transitions whereas the total angular momenta are dominated by spin-orbit coupling.

Of particular interest are the heaviest Uranium species selected as candidates to probe uniquely our understanding of atomic structure. The radiative recombination processes in the collision of cold heavy ions, injected from ESR into CRYRING decelerated down to 10 MeV/u, with free electron occur in the cooler region. The cooler electron beam usually is described in terms of an anisotropic Maxwell-Boltzmann distribution with transversal temperature several meV and parallel temperature several tens-µeV, highlighting the well-controlled experimental conditions. As a consequence of the "cold" temperature conditions, a spectrum simulation/prediction has to consider recombination into excited projectile states with principal quantum numbers n of up to about $n = 200$ whereby the cutoff parameter is finally defined by the magnetic field settings of the dipole magnets of the storage ring.

As the electron beam has a velocity distribution, introducing an integrated quantity namely the rate coefficient instead of the radiative recombination cross section, defined for a fixed electron velocity, appears to be more reasonable. Since no existing database can provide the required extensive set of energy levels, transition probabilities, and radiative recombination cross sections for the relevant ions of Uranium, the input data for radiative recombination simulations need to be generated using accurate atomic code [2, 3]. The simulated spectral line profiles are approximated by a Gaussian function with a FWHM of 80 eV, keep pace with high resolution x-ray spectra of highly charged ions registered by microcalorimeter spectrometer. The (preliminary) x-ray spectrum associated with radiative recombination, consisting of Lyman transition lines together with intense state selective Balmer spectrum is depicted in Figure 1.

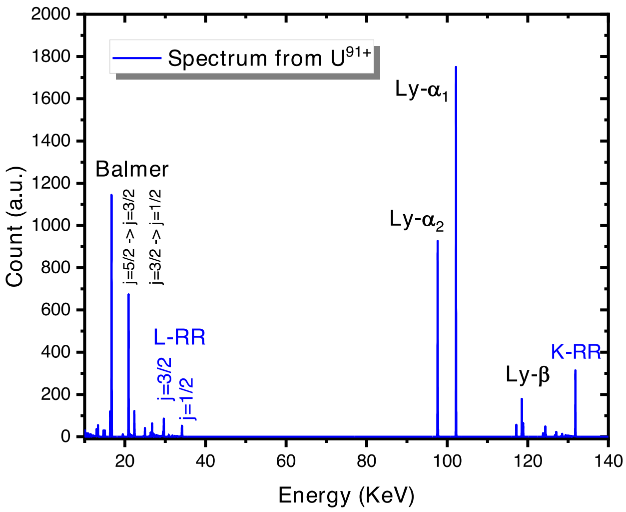

Figure 1: Calculated x-ray spectrum at C.M. system for $U^{92+} \to e^-$ collisions at 10 MeV/u.

Binghui Zhu as a recipient acknowledges CSC Doctoral Fellowship for 2018.9-2022.2.

References

[1] Th. Stöhlker *et al.*, Chapter 11 in "The Physics of Multiply and Highly Charged Ions", Springer (2003).

[2] M. F. Gu, Can. J. Phys. **86**, 675 (2008).

[3] P. J. Storey and D. G. Hummer, Comput. Phys. Commun. **66**, 129 (1991).

* b.zhu@hi-jena.gsi.de

Characterisation of the Breit-Wheeler pair detection system at Gemini

D. Hollatz*[1,2,3], F. Salgado[1,2,3], R. Watt[5], C. Colgan[5], G. M. Samarin[4], E. Gerstmayr[5], B. Kettle[5], S. P. Mangles[5], and M. Zepf[1,2,3]

[1]HI Jena; [2]GSI, Darmstadt; [3]IOQ, FSU Jena; [4]Queen's Univ. Belfast; [5]Imperial College London

We present recent results on the characterisation of the pair detection system for Breit-Wheeler (BW) experiments at Astra Gemini. The two-photon or linear Breit-Wheeler process $\gamma + \gamma \rightarrow e^- + e^+$ was first described in 1934 [1] as the collision of two photons to form an electron positron pair from quantum vacuum, which is not experimentally observed to this day. A series of experiments at Astra Gemini pursued this objective, which required a detection system for single electron positron pairs. We developed and tested such a system and present a measurement of the beam line transport efficiency of 14% for generated Breit-Wheeler pairs and update some results we presented last year.

Astra Gemini is a two beam titanium doped sapphire laser system with each arm delivering 12 J within 40 fs. One beam is focussed with an $f/40$ spherical mirror into a gas cell to accelerate electrons via laser wake field acceleration (LWFA) up to 700 MeV with 50 pC above 300 MeV. This beam propagates through a 1 mm thick Bismuth converter target to emit bremsstrahlung, which is further collimated by a 10 cm long hollow cylinder of solid Tantalum with a 1 mm inner radius. A 1 T strong, 40 cm long permanent dipole magnet deviates charged particles to provide a clean multi 100 MeV photon beam. The second laser beam is focussed with an $f/2$ off-axis parabolic mirror onto a solid Germanium target to create 1 to 2 keV X-ray cloud from M-L shell transitions at an energy conversion efficiency of a few percent. The γ-ray beam propagates through the X-ray cloud to form BW pairs with a dominant momentum in γ-ray direction at multi 100 MeV kinetic energy. Created pairs are separated from the γ-ray beam by a dipole magnet, called separator, and focussed by a second pair of dipoles, called collimator, on single particle detectors (SPD) that are shielded from both the LWFA electron and γ-ray beam dump. The combination of separator and collimator magnets is referred to as analyser magnet system (AMS) and is characterised by the amount of produced BW pairs that are guided to the SPDs. This pair transport efficiency is essential when comparing measured and predicted pair yield and is calculated in two major steps, calculating pair trajectories for different phase space coordinates with Radia and second, calculate the phase space distribution of produced pairs on this setup with Geant4 so that combining these two gives a transport efficiency for BW pairs. With the γ- and X-ray parameters achieved at Gemini, BW pairs have a circular source size of 5 mm radius and divergences up to 5 mrad of which 14% hit the detector. Most particles are lost due to the limited spectral acceptance window from 220 MeV to 380 MeV whereas the majority of pairs is produced below 200 MeV. Within the acceptance window, transmission efficiencies of 80% for certain energies are achieved as shown on Fig. 1. Guided pairs impact the SPDs, each composed of 15 by 20 CsI(Tl) scintillator crystals. The emitted light is recorded by a 4Picos ICCD from Stanford Computer Optics that achieves single photon sensitivity. As a unit, the SPD achieves single particle sensitivity for BW class electrons and positrons of a few 100 MeV energy. The SPDs were calibrated by inserting a PTFE target into the beam at the BW source point to produce a known Bethe-Heitler positron signal on the SPD which was directly correlated to the recorded yield on the ICCD. This allowed a background characterisation of the overall setup and combined with theoretical predictions of the expected pair yield, the signal-to-noise ratio (SNR) was determined. In the end, the detection system composed of AMS and SPDs lowered the detected background by 4 orders of magnitude while transmitting 14% of produced BW pairs, increasing the SNR by 3 orders of magnitude. The sensitivity was tested with a 25 μm Kapton target in the beam to produce a know pair source at a SNR of 0.3. For the full dataset, the confidence in a signal surplus due to the Kapton target is 99% based on Poisson statistics. The absolute yield was 0.19 ± 0.03 positrons per pC of reference LWFA beam, which is close to the predicted rate of $0.43^{+0.30}_{-0.19}$ positrons per pC reference LWFA beam.

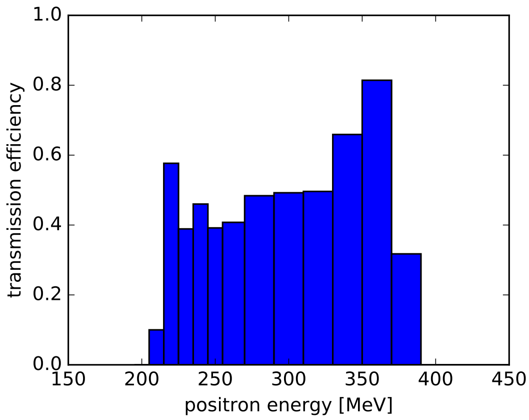

Figure 1: The transmission efficiency of the analyser magnet system for Breit-Wheeler class positrons.

References

[1] G. Breit and J. A. Wheeler, Phys. Rev. **46**, 1087 (1934).

* d.hollatz@gsi.de

Protective earth problems when using SQUIDs

V. Tympel*[1] and M. Stapelfeld[2]

[1]Helmholtz Institute Jena, Fröbelstieg 3, 07743 Jena, Germany; [2]Institute of Solid State Physics, FSU

The electrical protective earth (PE) conductor is an important safety feature for power lines. The PE use as grounding of interference filters of power supplies leads to high-frequency signals on PE lines. In the laboratory, this problem can be eliminated by batteries and separate measurement grounding. In field use, a connection between PE and measurement grounding is often unavoidable [1]. The use of extremely broadband sensors such as SQUID (superconducting quantum interference devices) used in a CCC (cryogenic current comparator) can even become impossible. This work shows the influence of power line filters and defined RF-interference by the example CCC and beam tube simulation in a shielded chamber.

The aim of the study was to quantify the possible influence on the SQUID parameters by RF-interference in a defined environment. Simulated interferences in the frequency range from 1 MHz (Agilent 3310A) to 1 GHz (Rohde & Schwarz SMR20) were coupled into the CCC via RF-cable and a piece of vacuum tube that passes through a CCC (Fig. 1). The setup was build up in a LHe bath cryostat and measured in an electrically and magnetically shielded chamber. With the exception of the SQUIDs and SQUID electronics, all electrical devices were outside the chamber.

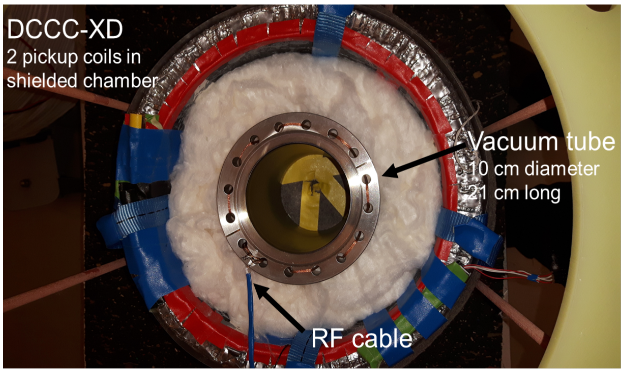

Figure 1: CCC pickup coils with tube in cryostat before LHe filling.

Even the completion of the wiring without switching on the generators was sufficient to render the SQUID unusable. Only after the introduction of a sheath current filter and a PE choke (Fig. 2) into the power supply line was it possible to stabilize the SQUID (Fig. 3).

An important parameter for system stability is the maximum SQUID voltage swing in a Phi0-period (typ. 50 μV). A swing reduction destabilizes the system in Flux-Locked Loop (FLL) mode. By coupling RF-voltage to the tube, it was always possible to reduce the SQUID voltage swing or to completely disable the SQUID. In the range between 200kHz and 90MHz, a voltage-frequency product of about 220 $\mu V_{rms} \times 1$ MHz was sufficient to achieve a halving of the voltage swing. This means that especially higher frequencies can interfere with the CCC system and should be avoided.

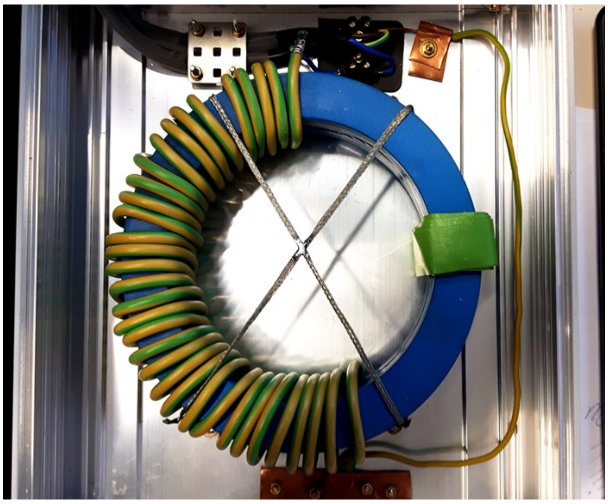

Figure 2: PE-choke with M616-02 ring core, inductance 70 mH @ 10 kHz, 15 mH @ 100 kHz.

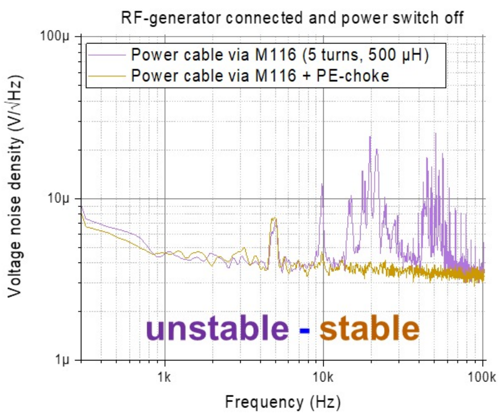

Figure 3: Correlation between SQUID noise density and stable SQUID FLL mode working.

The authors acknowledge funding from BMBF, project number 05P18SJRB1.

References

[1] https://www.nkl-emv.de

* v.tympel@hi-jena.gsi.de

First x-ray spectroscopy measurement at CRYRING@ESR

T.Over*[1], G. Weber[2,3], B. Zhu[1,3], Z. Andelkovic[2], R. Chen[2], D. Dmytriiev[2], O. Forstner[1,2,3], A. Gumberidze[2], C. Hahn[2], M. O. Herdrich[1,2,3], F. Herfurth[2], P.-M. Hillenbrand[2], A. Kalinin[3], Th. Köhler[1,2,3], F. M. Kröger[1,2,3], M. Lestinsky[2], Y. A. Litvinov[2], E. Menz[1,2,3], T. Morgenroth[2], N. Petridis[2], Ph. Pfäfflein[1,2,3], M. S. Sanjari[2], R. S. Sidhu[2], U. Spillmann[2], S. Trotsenko[2,3], L. Varga[2], and Th. Stöhlker[1,2,3]

[1]Friedrich-Schiller-Universität Jena, Institut für Optik und Quantenelektronik, Jena, 07743, Germany; [2]GSI Helmholtzzentrum für Schwerionenforschung GmbH, Darmstadt, 64291, Germany; [3]Helmholtz Institute Jena, Fröbelstieg 3, 07743 Jena, Germany

One of the frontiers of quantum electrodynamics (QED) is the study of electrons in extreme electromagnetic fields. Especially, the 1s Lamb shift in the heaviest stable hydrogen-like ions available in the laboratory, may serve as the ultimate testbed for rigorous experiments at high field strength. The coupling of the CRYRING and ESR storage rings, for the first time, enable state-of-the-art test of X-ray spectra registration from H-like Lead (Pb^{81+}) at electron cooler of CRYCRING, providing proof of the favorable conditions for planned spectroscopy precision study.

The aim of the planned experiment E138 is to measure the 1s Lamb shift in hydrogen-like uranium (U^{91+}) with an accuracy of better than 1 eV to test the non-perturbative bound-state QED on the level of 2nd order corrections. Recently, some significant parts of the experiment setup had been prepared and installed at the CRYRING electron cooler. In addition, several critical aspects regarding to accelerator settings were also successfully demonstrated in the commissioning beam time in May 2020. The bare lead ions (Pb^{82+}) were injected from ESR into CRYRING decelerated down to 10 MeV/u, which allowed us for a commissioning run for the aforementioned E138 experiment, as the beam lifetimes, ion trajectories and x-ray energies are expected to be quite similar as for U^{92+}. At the electron cooler, equipped with dedicated chambers for housing of the view ports for x-ray detection under 0° and 180° with respect to the ion beam axis, standard high-purity germanium x-ray detectors were mounted. In order to suppress the strong background of photons (bremsstrahlung) emitted from the electron beam, an ion detector (channel electron multiplier) was successfully operated downstream to the cooler, enabling to record x-rays in coincidence with recombined ions (Pb^{81+}) in the electron cooler section. Even though in this very first beam time with bare Pb^{82+} ions in CRYRING only a low intensity of max. 2×10^5 ions per injection was achieved, a few days of continuous operation were sufficient to accumulate meaningful spectral information when combining the signals in both x-ray detectors with the particle detector. The x-ray spectrum associated with radiative recombination observed at 0° at the electron cooler is shown in Fig. 1. Note, due to the exact 0° geometry, the tails of the Ly-α transition lines disappeared and intense Balmer radiation due to beryllium view-ports is clearly visible. For comparison, the x-ray spectrum observed in past studies at the electron cooler of the ESR with U^{91+} ions at the beam energy of 43 MeV/u is shown in addition [1].

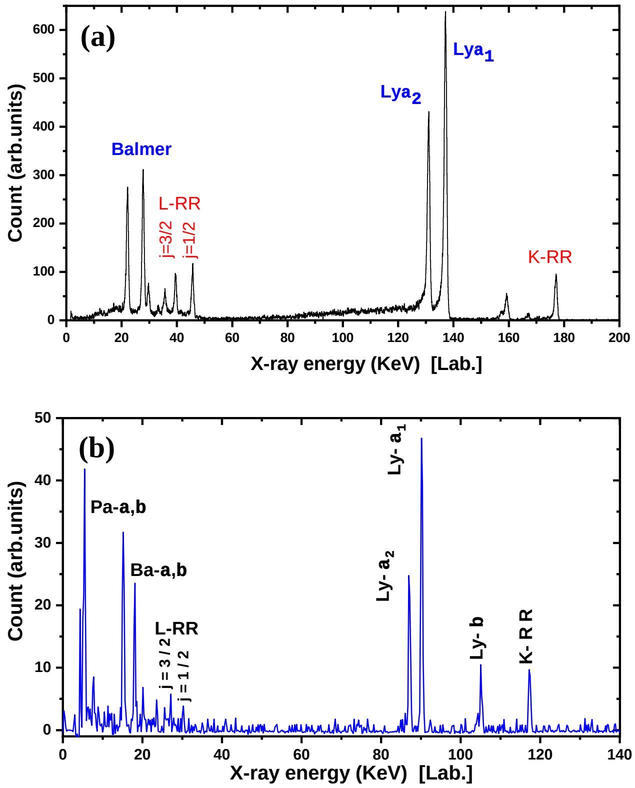

Figure 1: X-ray spectrum observed (a) at close to 0° for $U^{92+} \rightarrow e^-$ collisions at 43 MeV/u at ESR [1], and (b) at exactly 0° for $Pb^{82+} \rightarrow e^-$ collisions at 10 MeV/u.

This research has been conducted in the frame-work of the SPARC collaboration, experiment E138 of FAIR Phase-0 supported by GSI. It is further supported by the European Research Council (ERC) under the European Union's Horizon 2020 research by the innovation program (Grant No 682841 "ASTRUm"). We acknowledge substantial support by ErUM-FSP APPA (BMBF n° 05P19SJFAA) too.

References

[1] A Gumberidze *et al.*, Phys. Rev. Lett. **94**, 223001 (2005).

* tobias.over@uni-jena.de

Polarization transfer in Rayleigh scattering of hard x-rays out of the incident photon polarization plane

Wilko Middents*[1,2], Günter Weber[1,2,3], Marco Vockert[1,2], Uwe Spillmann[3], Philip Pfäfflein[1,2,3], Alexander Gumberidze[3], and Thomas Stöhlker[1,2,3]

[1]Helmholtz Institute Jena, Fröbelstieg 3, 07743 Jena, Germany; [2]IOQ Jena, Max-Wien-Platz 1, 07743 Jena, Germany; [3]GSI Darmstadt, Planckstraße 1, 64291 Darmstadt, Germany

Polarization experiments on elastic scattering of hard x-rays on atoms allows for a sensitive test of the underlying theory of quantum electrodynamics. In a beamtime during October 2020 at the synchrotron facility PETRA III we scattered an initially linearly polarized hard x-ray beam on a gold target and analyzed the polarization characteristics of the scattered beam both inside and out of the polarization plane of the incident beam.

Rayleigh scattering being the scattering of photons on bound electrons is the dominant process in elastic scattering of hard x-rays for photon energies in the keV regime up to $\hbar\omega \approx 1$ MeV. In the framework of quantum electrodynamics this process is described as the excitation of the bound electron into a virtual state, immediatly followed by deexcitation that leads to the emission of a photon with the same energy [1]. Momentum conservation requires that the momentum transfer during scattering is matched by the momentum of the bound electron. Thus for hard x-rays the electrons in higher shells contribute significantly only under small forward angles to the cross section, whereas for all other angles studies of Rayleigh scattering are probing almost exclusivley the K shell electrons. Theoretical calculations for a given target show that the polarization characteristics of the scattered beam strongly depend on the polarization characteristics of the incident beam and on the scattering geometry given by the scattering angle between incident and scattered photon ϑ and the azimuthal scattering angle φ between the polarization plane of the incident photon and the scattered photon [2].
A first experiment performed in 2014 analyzing Rayleigh scattering of a highly linear polarized incident beam for $\varphi = 0°$ already showed that while the polarization vector of the scattered beam stays oriented in the scattering plane, the degree of linear polarization strongly decreases for $\vartheta \to 90°$ well in accordance with theory for a slightly depolarized incident beam [3].

In October 2020 we extended on this study leaving the polarization plane of the incident beam, meaning $\varphi \neq 0°$, see Fig. 1 for a sketch of the experimental setup. Utilizing a position-sensitive 2D Si(Li) strip detector dedicated as Compton polarimeter [4] we analyzed the polarization characteristics of elastically scattered x-rays with a photon energy of 175 keV during one week of beamtime at beamline P07 of the PETRA III synchrotron facility of DESY, Hamburg. Fig. 2 (a) shows a Monte Carlo simulation of a characteristic polarization measurement taken during the

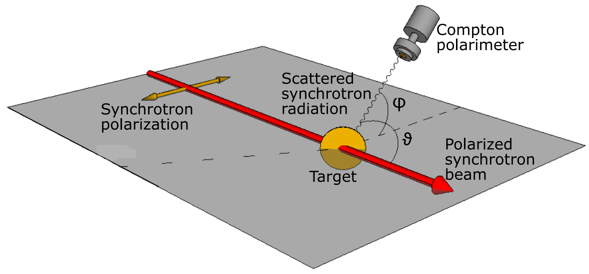

Figure 1: A sketch of the experimental setup. A linear polarized synchrotron beam with a photon energy of 175 keV is scattered on a thin gold target.

beamtime for $\vartheta = 88°$ and $\varphi = 45°$. The white dashed line shows the scattering plane and the red arrow marks the polarization of the Rayleigh scattered beam. As can be seen, the polarization is rotated to the scattering plane by the polarization angle χ when leaving the polarization plane of the incident beam. In fig. 2 (b) the actually measured polarization image under the same scattering position is shown. As expacted, the polarization vector is rotated under an angle χ to the scattering plane. However, the observed rotation as well as the measured degree of linear polarization strongly deviate from the theoretical prediction for the Rayleigh scattered beam.

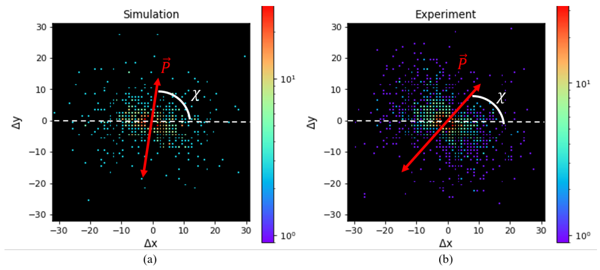

Figure 2: A characteristic polarization measurement with the Compton polarimeter, here for $\vartheta = 72°$ and $\varphi = 45°$. (a): Monte Carlo simulation, (b): Experiment.

The authors acknowledge funding from ErUM-FSP APPA (BMBF n° 05P19SJFAA).

References

[1] P. P. Kane *et al.*, Phys. Rep. **140**, 75 (1986).
[2] S. Strnat *et al.*, Phys. Rev. A **103**, 012801 (2021).
[3] K.-H. Blumenhagen *et al.*, New J. Phys. **18**, 103034 (2016).
[4] M. Vockert *et al.*, NIM B **408**, 313 (2017).

*wilko.middents@uni-jena.de

Detector Development for the Nonlinear Breit-Wheeler Experiment at CALA

F. Salgado*[1,2], A. Döpp[3], K. Grafenstein[3], Harsh[1,2], D. Hollatz[1,2], S. Karsch[3], and M. Zepf[1,2]

[1]Helmholtz-Institut Jena, Germany; [2]Institute of Optics and Quantum Electronics, Friedrich-Schiller-Universität Jena, Germany; [3]Ludwig-Maximilians-Universität München, Germany

Strong Field QED is a highly active area of research with untested fundamental phenomena such as vacuum pair production and non-linear QED phenomena becoming experimentally testable when the quantum parameter $\chi \sim 1$ [1]. Here we report the on development of a single-particle detection system with signal-to-noise ratio above unity for detecting single electron-positron pairs generated by the Breit-Wheeler process at the upcoming FOR2783 experiment which will be realized at the Centre for Advanced Laser Applications (CALA).

The experimental concept for the first detection of pairs from photon-photon interactions is based on an all optical set-up. In this concept, relativistic electron beams with energy of 2.5 GeV and a charge of 10 pC are produced by the laser wakefield accelerator (LWFA) and interact with a 50 µm tungsten target to produce bremsstrahlung γ-ray photons. The γ-photons propagate towards the interaction point (IP) where they collide with an optical laser beam with 43 J, pulse duration of 30 fs, central wavelength at 800 nm and, repetition rate of 0.1 Hz. The laser is focused using f/2 to < 2 µm focal spot parabola to reach intensities $> 10^{21}$ $\mathrm{Wcm^{-2}}$. The predicted pair yield is in the range 0.1-10 pairs per shot for the parameters of interest. Therefore, a detection system capable of detecting single-particles with a high signal-to-noise ration is essential for the success of the experiment.

The proposed e^+/e^- detection system is shown in Figure 1 and contains two LYSO screens and a Cherenkov calorimeter as part of the single-particle particle diagnostics.

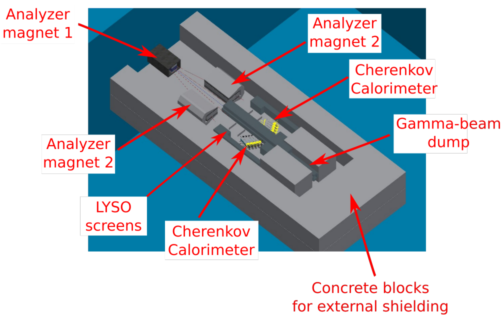

Figure 1: Detector region where the single-particle diagnostics, LYSO screens, and Cherenkov calorimeters detectors are placed.

The response of the detectors to diagnose single-particle hits were simulated using GEANT4, and the signal to noise-to-noise ratio (SNR) of a single detection channel of the Cherenkov calorimeter was estimated by comparing a full simulation of the backgrounds to the signal for a single GeV lepton. Figure 2 shows the number of Cherenkov photons obtained from the simulation for a single Cherenkov detection channel per incoming background particle energy. The background is composed solely of gamma-photons with energies at 3 MeV or lower which originate from multiple scattering of the primary particles.

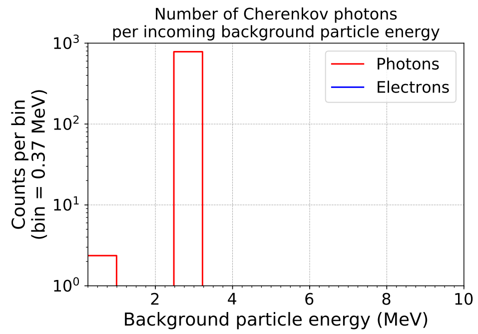

Figure 2: Signal due to background radiation in a single Cherenkov calorimeter channel. In total, about 786 background Cherenkov photons are expected per primary electron bunch.

A total of 786 photons are generated due to the background noise radiation for 10pC primary charge in the LWFA beam. Moreover, also using Monte-Carlo simulations, we obtained a single 1 GeV positron, which is typical of the energy range of the expected pairs, produces 4.9×10^4 Cherenkov photons at a detection channel. Therefore, the expected signal-to-noise ratio at a single detection channel is SNR $= 62$. We note that increasing the lWFA charge towards 1nC would linearly increase the background to levels comparable to that of a single 1 GeV positron.

In conclusion, the detector design coupled with GEANT 4 simulations predicts a signal to noise ratio of 62 for a single lepton incident on the detector. The signal to noise ratio for single signal leptons decreases with increasing primary beam charge in a single shot. This paves paving the way for the first observation of pairs from photon-photon collisions with moderate charge LWFA beams.

This research work was funded by DFG Research Group 2783 "Quantumvacuum".

References

[1] V. I. Ritus, J. Sov. Laser Res. **6**, 497 (1985).

[2] F. S. Englbrecht *et al.*, J. Radiol. Prot. **40**, 1048 (2020).

*felipe.salgado@uni-jena.de

Background Measurements for Photon-Photon Scattering Experiment

Pooyan Khademi*[1], Leonard Doyle[2], Peter Hilz[1], Jörg Schreiber[2], and Matt Zepf[1]

[1]Helmholtz Institute Jena, Fröbelstieg 3, 07743 Jena, Germany; [2]Ludwig-Maximilians-Universität München, Fakultät für Physik, Fakultät für Physik, 85748 Garching, Germany.

Experimental realization of photon-photon scattering from the quantum vacuum with High Intensity Lasers collisions requires an understanding of every single detected photon's origin. The background must be minimized. As a first step, we measured the scattered photons from modestly intense laser pulse propagating in vacuum to determine the initial level of backgrounds.

In the realm of quantum fields, the vacuum is filled with virtual electron-positron pair fluctuation. In presence of a strong EM-field the vacuum shows detectable signals (few scattered photons) of nonlinear behaviour[1], but the background (BG) generated by the intense laser $> 10^{19}$ photons poses a signifcant challenge. At JETi200 we took to take the first step to quantify the BG photons from rest gas and other scatter sources. A single laser pulse, 24 fs long with 175 mJ energy, was focused in vacuum with an F/1.5 off-axis parabolic mirror (OAP) down to 2.2 µm. The light from ambient sources (photons scattered from objects in the chamber) and Thomson scattered light was collected with a 20 × objective imaging the focus perpendicular to the propagation axis,with a single photon sensitive gated ICCD camera with QE of 16.6 % for 800 nm with gate time of 1 ns as detector. The gated imaging minimizes the time that the scattered photons can reach the detector and allows discrimination of background sources Photons scattered by electrons (Thomson Scattering) have a linear dependence on the vacuum pressure. Starting from atmospheric gas composition, the main contributor to the free electrons in high pressure is from Nitrogen. Our Laser pulse with $a_0 \approx 5$ is strong enough to strip at least 7 electrons from the Nitrogen. Furthermore, the chamber was flooded by Helium at low pressures (10^{-2} to 10^{-5}mbar) to test Helium dominant interaction conditions . The intense laser pulse fully ionizes the Helium substanially before the arrival of the peak of the pulses. Fig.1, shows the scattered photons for different pressures, from a $70 \times 70\mu m^2$ ROI around the focus. The number of scattered photons fits closely to estimates based on Thomson scattering calculations. The polarization defines the dipole oscillations i.e. electrons oscillations for V-pol is parallel to the objective and for H-pol is perpendicular to the objective. Fig.1 shows the difference in photon number for V and H-pol, with the difference between the two polarisations limited due to the collection of wide angular cone and the laser cone angle. Due to scattering into the collection light path within the chamber, Thomson photons from the focus are not the only photons reach the detector. This scattered light become the dominant source of BG at pressures ($< 10^{-5}$ mbar) and will be addressed in future experiments. Fig.2 shows the Thomson scattering BG. For a uniform electron density, the number of scattered photons should remain constant at each point along the laser axis with the reduced transverse size leading to an intensity peak at the focus Instead an intensity dip at focus is visible with a factor of ≈ 10 inferred for reduction of electron density at the focus, suggesting that ponderomotive 'vacuum cleaning' is highly effective. In conclusion, in a "Multi PW-beam experiments" with 3 orders of magnitude higher energy (175 J) in a ROI $< 7 \times 7\,\mu m^2$, the fs-gated detection and ponderomotive 'cleaning' at $< 10^{-9}$ mbar are promising to achieve sufficiently low BG for photon-photon scattering experiments.

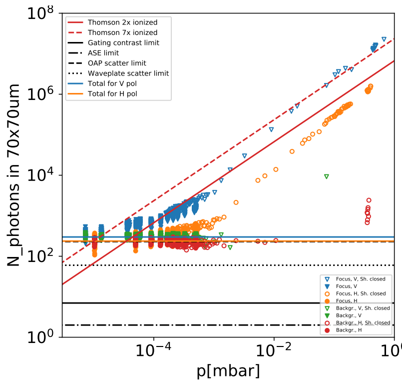

Figure 1: Pressure Dependency of Scattered Photon showing pressure dependent thomson scattering and direct scattering into beam path.

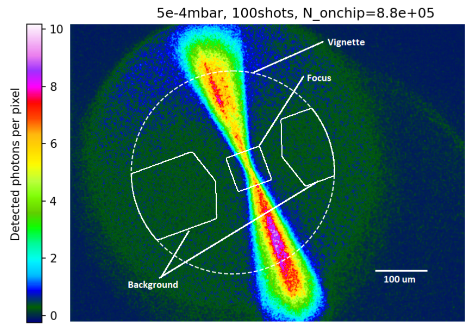

Figure 2: Thomson Scattering at 5×10^{-4} mbar. Note the intensity dip at focus due to ponderomotive e^--expulsion.

The authors acknowledge funding from DFG within the Research Unit FOR2783/1.

References

[1] F. Karbstein *et al.*, New J. Phys. **17**, 043060 (2015).

*p.khademi@hi-jena.gsi.de

The LUXE Experiment

M. Zepf*[1,2], D. Seipt[1], X. Huang[1,2,3], and the LUXE collaboration[4]

[1]Helmholtz Institute Jena, Fröbelstieg 3, 07743 Jena, Germany; [2]University of Jena, Max-Wien-Platz 1, 07743 Jena, Germany; [3]University of Freiburg, Freiburg, Germany; [4]full institution list on Conceptual Design Report

The LUXE experiment is an international collaboration aimed at performing precision strong field QED experiments using the 17.5 GeV electron beam of the European XFEL situated in Hamburg and an intense laser focused to intensities in the range of $10^{19} \ldots 10^{21}$ Wcm^{-2}. This allows the critical field of QED E_c to be reached and exceed in the centre of momentum frame of both electron-laser and γ-laser collisions. LUXE will be the first experiment capable of such γ-laser interactions at field strengths exceeding E_c and the first experiment for dedicated strong-field QED measurements.

The interaction of high energy particles (electrons and γ-rays) with an intense field allows the physics of strong field QED to be tested. The critical field of QED - the parameter which defines the strong field regime - $E_c = m_c^3/e\hbar \approx 10^{18}$V/m and corresponds to a field capable of performing the work of the rest mass energy of an electron over the Compton wavelength. The laser field is typically a factor of $\sim 10^4$ below the critical field in the laboratory frame. However in the boosted frame this is increased by the Lorenz-factor γ (in the case of electrons) allowing field in the rest frame to exceed the critical field and $\chi = \gamma E/E_c > 1$. Under these conditions pair creation from the quantum vacuum and non-linear coupling of the field to the particles can take place. Figure 2 shows the Feynmann diagramms of two of the processes of interest. The non-linear Breit-Wheeler effect, describes the direct production of matter pairs from the vacuum through the combination of multiple photons in the collision, allowing the interaction of fields with the quantum vacuum to be observed directly through the creation of lepton pairs. HI Jena is contributing to both the strong-field theory effort as well as the design of the laser system, IP and detectors.

An area of particular importance is the accurate determination of the interaction conditions and excellent statistics for precise comparison with theory. The location shown in figure 1 at the end of the XFEL accelerator allows continuous beam availablity during XFEL operation at a rate of 10Hz - providing the basis for excellent statics. The strong non-linearity of the processes requires the laser to be precisely characterised - with a shot-to-shot knowledge of the laser interaction intensity at focus $< 1\%$. This is significantly beyond what can be currently achieved with flash-lamp-pumped laser systems with the beam propagating in air and realistic levels of environmental vibration. The weak interaction even at these high intensities allows the laser to be transmitted essentially unperturbed (Fig. 3), allowing the laser interaction point to be precisely diagnosed after attenuation. The diagnostics currently being developed allow shot intensity tagging to with a goal of $\Delta I/I < 1\%$. Work is ongoing with the preparation of the TDR being undertaken currently.

*m.zepf@hi-jena.gsi.de

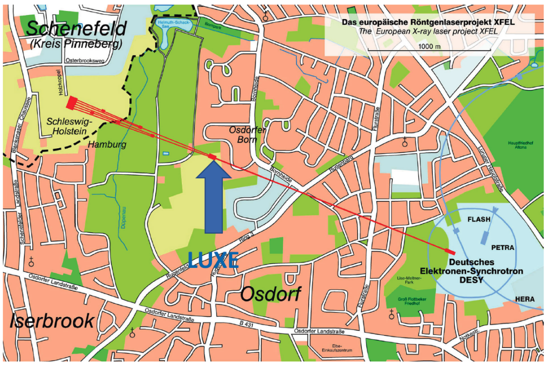

Figure 1: LUXE is situated at the end of XFEL accelerator section of the XFEL, where bunches at 10Hz will be available continuously for precision measurments.

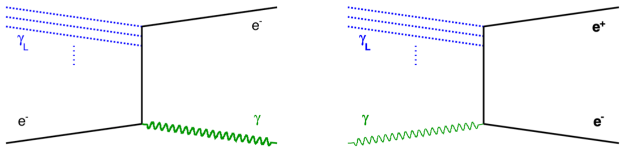

Figure 2: The LUXE experiment will make precision measurements of strong field QED phenomena reaching $\chi > 1$.

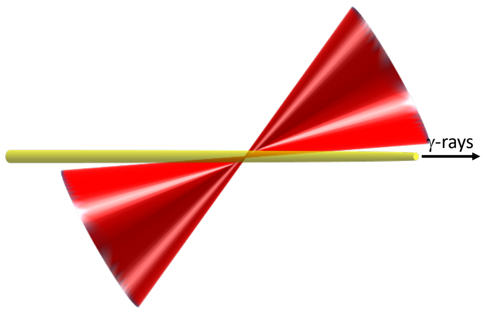

Figure 3: Conceptual Layout of the interaction point of the LUXE experiment. The laser is focused on the e-beam of γ-ray beam and recollimated for precision shot-to-shot diagnostic.

References

[1] LUXE Conceptual Design Report arXiv:2102.02032 (2021).

THEORY

High Harmonic Generation driven by elliptically polarized laser beams

Anne Weber*[1], Birger Böning[2,3], and Stephan Fritzsche[1,2,3]

[1]Theoretisch-Physikalisches Institut, Friedrich-Schiller-Universität Jena, Germany; [2]Helmholtz Institute Jena, Fröbelstieg 3, 07743 Jena, Germany; [3]GSI Helmholtzzentrum für Schwerionenforschung GmbH, Darmstadt, Germany

Single-atom high-order harmonic generation by a monochromatic laser field is considered in the strong-field approximation. By utilizing the semi-classical approach we determine the most relevant quantum orbits contributing to the harmonic spectrum. In addition to the intensity of the generated harmonic radiation, also its ellipticity is calculated, as well as the classical analog of the electron's trajectories which give insight about the origin of the harmonic radiation's characteristics.

High harmonic generation (HHG) on a microscopic scale can be viewed in terms of the well-known semi-classical three-step model: The intense laser field ionizes an atom, the liberated electron gets driven back to the parent ion and finally recombines by emitting a high energetic photon. Theoretically, the intensity of the q-th harmonic (with frequency q times the laser field frequency ω) is proportional to the T-matrix element as described in [1]. For the interaction of a periodic laser field and a hydrogen-like atom the T-matrix element is obtained by integrating over possible recombination times within one laser field cycle T: $\mathbf{T_q} = \int_0^T \mathrm{d}t\ \mathbf{d}(t)\mathrm{e}^{iq\omega}/T$, with the dipole moment $\mathbf{d}(t)$. The calculation of the latter involves the integration of Feynman's propagation factor over all ionization times. Due to the rapidly changing action in the exponent of the propagator one can apply the saddle point method, i.e. approximate the integral by summing over those values of the integrand, where the exponential phase term is stationary. Finding stationary points of the exponent results in solving a system of nonlinear saddle-point equations for complex sets of ionization time, recombination time and momentum $(t_i, t_r, \mathbf{p})$, respectively. The real parts of the times and momentum then trace out unique paths following Newtonian mechanics, so-called quantum orbits. Within each cycle of a monochromatic field two paths exist, that have slightly different travel times, referred to as short and long trajectory, respectively. Examples of those classical paths for various harmonic orders can be seen in Fig. 1. Now, summing up the contributing dipole moments yields the harmonic spectrum. In Fig. 2 the spectra for the slightly elliptical field is compared to a linearly polarized field.

Generally, a linearly polarized field will result in linearly polarized harmonics, whereas an elliptically polarized field produces elliptically polarized harmonic radiation. The harmonic intensity for the elliptical field is lower than for the linearly polarized field, because the traveling electron eventually misses the parent ion when the laser field changes direction. Because controllable ellipticity of harmonic radiation is highly desired for multiple applica-

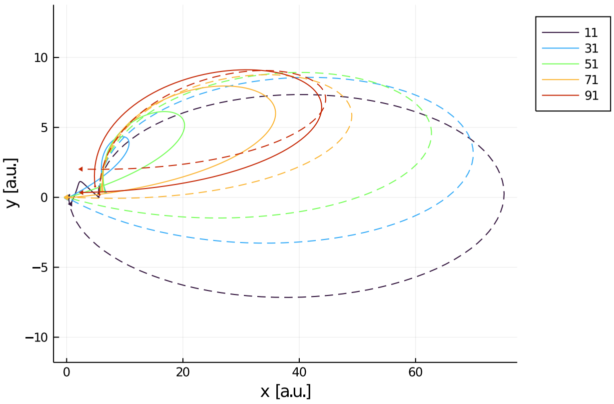

Figure 1: Classical trajectories of travelling electrons during the HHG process resulting in different harmonic orders, for Argon in a monochromatic slightly elliptical laser field ($\lambda = 800$ nm, $\varepsilon = 0.2$, peak intensity $I_0 = 5 \cdot 10^{14}$ W/cm^2). Dashed (solid) lines denote long (short) trajectories.

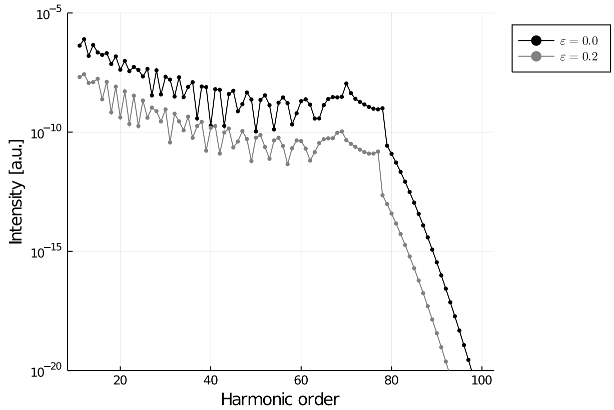

Figure 2: Spectrum of HHG by fields of slightly different ellipticity. The other parameters are the same as in Fig. 1.

tion purposes, recent publications investigate quantum orbits of HHG by bilinear (bicircular) two-color beams, as they also produce elliptical (circular) harmonics. To better understand the underlying processes and thereby enhance experimental reproducibility, we shall further apply the quantum orbit approach not only to two-color beams of same polarization, but also to bielliptical beams.

References

[1] D. B. Milošević and W. Becker, Phys. Rev. A **102**, 023107 (2020).

*a.weber@uni-jena.de

Control of photoelectron forward momentum in strong-field processes

Birger Böning*[1,2,3] and Stephan Fritzsche[1,2,3]

[1]Helmholtz Institute Jena, Fröbelstieg 3, 07743 Jena, Germany; [2]GSI Helmholtzzentrum für Schwerionenforschung GmbH, Darmstadt, Germany; [3]Theoretisch-Physikalisches Institut, Friedrich-Schiller-Universität Jena, Germany

Strong-field atomic processes like high-harmonic generation (HHG) and above-threshold ionization (ATI) are affected by the magnetic Lorentz force. For long-wavelength driving laser beams, electrons ejected from target atoms are driven along the beam axis, suppressing their rescattering with parent ions. We show that this suppression can be undone by controlling the photoelectron forward momentum with two identical driving laser beams that propagate under a small crossing angle. This setup might enable the efficient generation of x-ray high-harmonic radiation on the table-top.

If an intense laser beam irradiates an atomic gas target, the atoms are ionized and the ejected electrons propagate in the continuum. For appropriate laser parameters, the electrons are driven back to their parent ions and recombine or rescatter, leading to the emission of high-energetic radiation (HHG) or the observation of high-energetic photoelectrons (ATI). The cut-off energy $\hbar\omega_{\max}$ of the HHG spectrum increases with the ponderomotive energy $U_p \sim I\lambda^2$ where I and λ are the intensity and wavelength of the driving laser beam. However, if one tries to increase $\omega_{\max}$ by tuning the wavelength from the typical near-infrared towards the mid-infrared, a significant suppression of the intensity of the emitted high-harmonic radiation is observed. This suppression occurs since the ejected electrons are driven along the beam axis by the *magnetic* Lorentz force, thus missing the parent ion and preventing recombination.

In the past years, we have shown how the magnetic field can be included in the theoretical description of strong-field processes on the basis of the so-called strong-field approximation (SFA) [1]. For a single driving laser beam, this theory successfully reproduces the forward drift of photoelectrons in ATI. Recently, a simple setup was proposed to eliminate this forward drift at long driving wavelengths and to recover the HHG signal [2]. Here, a second laser beam is added to the first and both beams are identical in polarization, intensity and wavelength. However, their beam axes are aligned under a small crossing angle β and, as a result, the magnetic Lorentz force exerted on electrons in the continuum differs from the single-beam setup.

We used our reformulation of the SFA in order to analyze this setup in detail with respect to the forward momentum Δp_z of photoelectrons emitted in ATI [3]. The forward momentum is visible in the polar-angle distributions, displayed in Fig. 1: For a single beam that propagates along the horizontal $z-$axis ($\beta = 0$), two lobes are visible that are slightly tilted along this axis, corresponding to a momentum $\Delta p_z \approx 5 \times 10^{-3}$ a.u. If the second beam is added and the crossing angle β is increased, the lobes rotate counter-clockwise. Most importantly, an optimal crossing angle β_0 can be found for which $\Delta p_z = 0$ for electrons emitted in the upper half ($\Delta p_x > 0$). For this optimal crossing angle, therefore, half of the electrons return to their parent ions and recombine or rescatter, which leads to a significantly increased harmonic yield. Our detailed computations showed that such an optimal crossing angle can be found for all intensities and wavelengths of the driving laser beam.

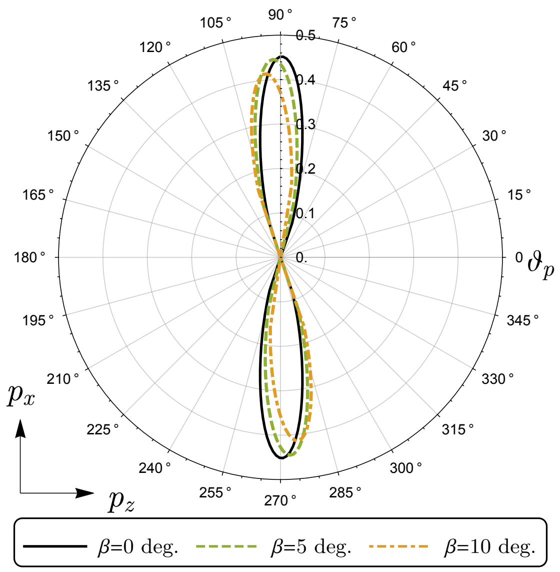

Figure 1: Photoelectrons polar-angle distributions with energy $E_p = 8.1$ eV $\approx 5.2\omega$ emitted in the ATI with two non-collinear laser beams ($I = 10^{14}$ W/cm^2, $\lambda = 800$ nm) for three values of the crossing angle β and for an argon target.

Thus, in practice, the forward momentum can be controlled for long-wavelength driving beams and high-harmonic radiation with energies in the x-ray domain might be generated with sufficient yields. In the future, we plan to explicitly compute these harmonic yields for the above beam setup within our SFA theory.

The authors acknowledge funding from the German Research Foundation (DFG, Deutsche Forschungsgemeinschaft) under the project number 440556973.

References

[1] E. Pisanty *et al.*, New J. Phys. **20**, 053036 (2018).

[2] B. Böning *et al.*, Phys. Rev. A **99**, 053404 (2019).

[3] B. Böning and S. Fritzsche, Phys. Rev. Lett., submitted (2021).

*b.n.boening@hi-jena.gsi.de

Torus Knot Angular Momentum in Twisted Attosecond Pulses from High Harmonic Generation

B. Minneker*[1,2,3], B. Böning[1,2,3], and S. Fritzsche[1,2,3]

[1]Theoretisch-Physikalisches Institut, Friedrich-Schiller-Universität Jena, Germany; [2]Helmholtz Institute Jena, Germany; [3]GSI Helmholtzzentrum für Schwerionenforschung GmbH, Germany

Bicircular bichromatic Laguerre-Gaussian beams have been found to possess torus knot angular momentum (TKAM), which is a new form of angular momentum. TKAM is conserved in nonlinear atomic processes such as high harmonic generation and can be classified by the time delay parameter τ and the coordination parameter γ. We derive a consistent geometric TKAM-model to classify τ and γ from the driving beam as well as the high harmonic radiation. We show the classification for a planar atomic gas target irradiated by bicircular Laguerre-Gaussian beams. Moreover, we demonstrate that besides γ, τ can be associated with a torus knot as well. Furthermore, we derive a geometric method that relates τ and γ to each other. Thus, the geometric TKAM-model characterizes the incoming and outgoing radiation.

In recent years, the interest in strong-field processes like strong-field ionization and high harmonic generation (HHG) increased. Within the ongoing progress of HHG in atomic gaseous targets, a broad range of tune-able parameters are available. Especially the angular momentum of the driving beam can be varied to tailor the high harmonic (HH) radiation effectively [1].

HHG with bicircular Laguerre-Gaussian (LG) driving beams reveal classification issues within angular momentum in general. Since the superimposed LG beams do not have the same orbital angular momentum ℓ (OAM) or frequency ω, these beams do not obey the dynamical symmetry transformations anymore. The angular momentum reveals to be ill-defined. The solution to this problem is a new form of angular momentum, the torus knot angular momentum [2].

$$\hat{J}_\gamma = \hat{L}_z + \gamma \hat{S}_z, \tag{1}$$

Here, $\hat{L}_z$ and $\hat{S}_z$ denote the projected orbital angular momentum and the projected spin angular momentum, respectively. The coordinated rotation parameter $\gamma = \frac{p_1\ell_2 - p_2\ell_1}{p_1+p_2}$ depends on the beam parameters ℓ_1, ℓ_2, ω_1 and ω_2 with $\omega_i = q_i\omega$. Therefore, ℓ_i are integer and q_i are positive integers. The associated dynamical symmetry reads than,

$$\mathbf{R}(\gamma\alpha)\mathbf{E}(\mathbf{R}(\alpha)\mathbf{r}, t) = \mathbf{E}(\mathbf{r}, t + \tau\alpha). \tag{2}$$

The coordination parameter γ is associated with a torus knot, displayed in Fig 1c. Fig.1a describes the evolution of the planar time-dependent electric field strength (blue Lissajous figures). Here, the azimuthal angle φ of the cylindrical coordinate system evolves on the straight black axes.

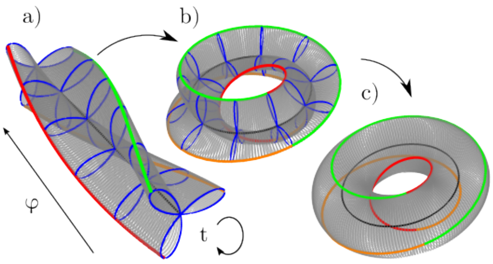

Figure 1: a) Evolution of the Lissajous figure with respect to the azimuthal angle φ of a driving beam with $\ell_1 = \ell_2 = 1$ and $\omega_1 = \omega_2/2 = \omega$, b) Closed curve formed by connecting the open ends, c) Intensity maxima on the surface of a torus. Torus knot of type (-1,3) which is associated to $\gamma = -\frac{1}{3}$

Fig.1b indicates how to connect the open ends of Fig.1a, which creates a torus knot that is directly related to γ. We demonstrate a similar method to classify the time delay parameter τ of the dynamical symmetry Eq.(2). In contrast to the torus knot of Fig.1c, the temporal dimension of the τ torus knot evolves on the straight black axes of Fig.1a. Thus, the azimuthal evolution is encoded in the curved dimension of Fig.1a. Both tori are constructed from the same quantity, namely the electric field maxima. It turns out that the order of operation to create the torus knot (time or azimuthal angle on the straight axes in Fig.1a) leads either to a τ torus knot or a γ torus knot. So, the electric field maxima of the diving beam uniquely define the coordination parameter γ and the time delay parameter τ. Since TKAM is a conserved quantity [3], we show that the above-applied method can also be applied to the high harmonic radiation. Further, both parameters can be associated with a torus knot, where the knots are constructed from the same field but differ in the order of operation to create them. The field is a two-dimensional (azimuthal and temporal) planar map of the electric field maxima. The curved dimension in Fig.1a occurs while using the boundary conditions to connect two ends of the planar map that results in a cylinder.

References

[1] W. Paufler *et al.*, Phys. Rev. A **98**, 011401 (2019)

[2] E. Pisanty *et al.*, Phys. Rev. Lett. **112**, 203201 (2019)

[3] E. Pisanty *et al.*, Nature Photonics **13**, 569-574 (2019)

*bjoern.minneker@uni-jena.de

Single- versus multi-cycle non-sequential double ionization of Ar

Fang Liu*[1,2] and Stephan Fritzsche[1,2,3]

[1]Helmholtz Institute Jena, Fröbelstieg 3, 07743 Jena, Germany; [2]Theoretisch-Physikalisches Institut, Friedrich-Schiller-Universität Jena, 07743 Jena, Germany; [3]GSI Helmholtzzentrum für Schwerionenforschung GmbH, Darmstadt, Germany

Using an improved quantitative rescattering (QRS) model, we calculate the correlated two-electron momentum distributions (CMDs) of nonsequential double ionization (NSDI) of Ar exposed to intense laser pulses with a wavelength of 790 nm at a peak intensity of 1.0×10^{14} W/cm^2. We analyze the drastic variations in the CMDs that were observed by Kübel *et al.* [1] in the transition from near-single-cycle to multi-cycle driving laser pulses. We find that the transition from near-single-cycle to multi-cycle driving laser pulses depends strongly on the details of the pulse envelope.

According to the QRS model [2] of NSDI, with the prepared parallel momentum distribution of the first returning electron after recollision and the parallel momentum distribution of the second electron tunnel-ionized from an excited state of the parent ion, respectively, the CMD for laser-induced electron impact excitation with subsequent tunneling ionization in the laser field with a peak intensity I is obtained as

$$D(p_\parallel^1, p_\parallel^2) = \int_{I_p^{(\mathrm{exc})}}^{\infty} dE_i\, D_{E_i,I}^{(\mathrm{RESI})}(p_\parallel^1, p_\parallel^2) W_I(E_r), \qquad (1)$$

where $W(k_r)$ is the RWP describing the momentum distribution of the returning electron with kinetic energy $E_r = k_r^2/2$. Using the QRS model [2], we computed the CMDs for NSDI of Ar in 790 nm laser pulses at a peak intensity of 1.0×10^{14} W/cm^2 with pulse durations of 4 fs, 8 fs, 16 fs, and 30 fs, respectively. And we present direct comparisons of our model results with the experimental results [1]. It can be seen from Fig. 1 that the QRS model well reproduces the overall pattern of the experimental findings.

In the present work, we focus on unveiling the mechanisms for the cross-shaped CMD for 4 fs and the collapse of the cross-shape in the CMD for 8 fs. Our study reveals that the strong backward scattering of the first returning electron from the parent ion, due to the low incident energy (the maximum energy of the returning electron is less than 20 eV), and the narrow parallel momentum distribution (the maximum value of the parallel momentum is about half of A_0) for the tunnel-ionized electron, owing to the restriction of the carrier envelope on the laser pulse, are responsible for forming the cross-shaped CMD or 4 fs.

We further find that the collapse of the cross shape when the pulse duration is increased to 8 fs results from the significant change in the temporal shape of the laser pulse. Since the consecutive local field maxima near the center of the pulse have almost the same absolute value for 8 fs laser pulses, no significant discrepancies exist between left-side and right-side recolliding wave packets, which are associated with tunnel-ionization of the first electron returning to the parent ion along $+\hat{z}$ and $-\hat{z}$ respectively. As a result, the magnitudes of the left-side and right-side CMDs are almost the same. More importantly, due to the same reason, the widths of the momentum distributions along $p_2^\parallel$ in the left-side and right-side CMDs also become comparative and are close to $2\,A_0$. The side-arm for 4 fs then turns out to be approximately a square-shape for 8 fs, leading to the collapse of the cross-shaped CMD.

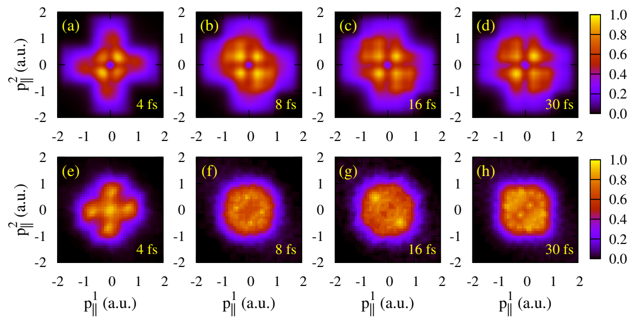

Figure 1: Normalized correlated two-electron momentum distribution $D(p_\parallel^1, p_\parallel^2)$ for NSDI of Ar in 790 nm laser pulses with a peak intensity of 1.0×10^{14} W/cm^2. The theoretical results (top row) and the experimental measurements [1] (bottom row) are compared for pulse durations of 4 fs (a,e), 8 fs (b,f), 16 fs (a,e), and 30 fs (a,e), respectively. The results for 4 fs and 8 fs are CEP-averaged.

This work was supported by the National Natural Science Foundation of China under Grant No. 11274219 and Guangdong Basic and Applied Basic Research Foundation, China, under Grant No. 2021A1515010047. T.M. was supported in part by the Japan Society for the Promotion of Science under Grants No. 19H00887 and 21K03417. K.B. was supported by the U.S. National Science Foundation under Grants No. PHY-1803844 and No. OAC-1834740, as well as the XSEDE Allocation No. PHY-090031. S.F. acknowledges funding by the Deutsche Forschungsgemeinschaft (DFG, German Research Foundation) under Project No. 440556973.

References

[1] M. Kübel *et at.*, New J. Phys. **16**, 033008 (2014).

[2] Z. Chen *et at.*, Phys. Rev. Lett. **79**, 033409 (2009).

* fangfangliu2020@gmail.com

Elliptical Dichroism in Biharmonic Ionization of Atoms

J. Hofbrucker*[1,2,3], A. V. Volotka[1,2], and S. Fritzsche[1,2,3]

[1]Helmholtz Institute Jena, Germany; [2]GSI, Darmstadt, Germany; [3]Friedrich-Schiller University Jena, Germany

In multiphoton ionization of atoms, elliptical dichroism may arise in the photoelectron angular distributions due to the interference of the possible ionization pathways. We here consider the interaction of atoms with an elliptically polarized biharmonic (ω + 2ω) field which simultaneously allows one- and two-photon ionization of the atoms. The interference between these two ionization pathways introduces contributions to the elliptical dichroism in addition to the dichroism that arises from the two-photon ionization alone. We show that these additional dichroism contributions can lead to a stronger dichroism in comparison to the one arising from two-photon ionization only. We present a relativistic analysis of the corresponding photoelectron angular distributions and discuss individual contributions to the dichroic phenomena. Detailed computations have been performed for biharmonic ionization of neutral helium atoms.

Biharmonic ionization of atoms is often used to refer to the photoionization by light beams that consists of two co-propagating components with frequencies which are integer multiples of some fundamental frequency ω, i.e. $n\omega + m\omega$. In biharmonic ionization, therefore, $n\omega$ and $m\omega$ multi-photon ionization may both result in the same final state of the photoelectron (and ion). The photoelectron angular distribution is then composed of the contributions of both ionization paths as well as their interference.

In our recent work [1], we showed that the angle-differential rate can be characterized by three contributions

$$\frac{dW}{d\Omega} = \frac{dW_{\text{sym}}}{d\Omega} + \frac{dW_{\text{dich}}}{d\Omega} + \frac{dW_{\text{asym}}}{d\Omega}. \tag{1}$$

We analyzed the contributions to the angular distribution of photoelectrons from the dichroic term $\frac{dW_{\text{dich}}}{d\Omega}$ in detail. In particular, we explained the origin of the dichroism and showed that the dichroism arising from the interference between the one- and two-photon ionization posses different rotational symmetries than the one arising from the two-photon ionization process [2]. Detailed computations have been carried out for the specific case of the ionization of neutral helium. We found that, in addition to the dependence of the angular distribution on the handedness of the elliptically polarized beam in pure two-color ionization, such a dichroism is also present in the biharmonic ionization. Most importantly, we showed that the dichroism can be enhanced by tuning the intensity of the second harmonic beam and the relative phase between the beams properly.

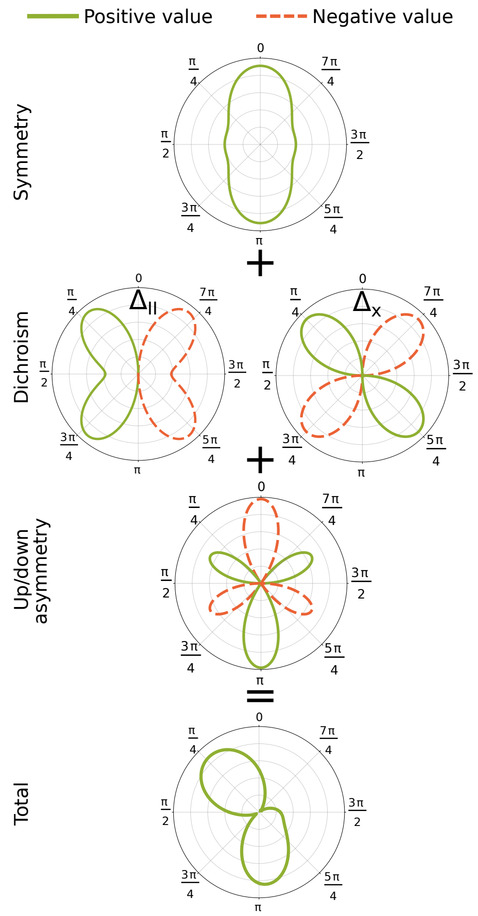

Figure 1: The angle-differential biharmonic ionization rate can split into symmetric, dichroic and asymmetric contributions. Contributions arising from interference between different ionization pathways can be either constructive (or positive, full green) and destructive (or negative, dashed red), while the symmetric and final distributions are always positive-valued. The dichroic contribution can be further split into two fundamentally different parts, one with one-fold rotational symmetry within the polarization plane (second line, left) and one with two-fold rotational symmetry (second line, right). The asymmetric term is shown in the third line. The total distribution (fourth row) results from the sum of all above contributions.

References

[1] J. Hofbrucker, B. N. Böning, A. V. Volotka, S. Fritzsche, submitted to Phys. Rev. A.

[2] J. Hofbrucker, A. V. Volotka, S. Fritzsche, Phys. Rev. Lett. **121**, 053401 (2018).

* j.hofbrucker@gsi.de

Quantum vacuum signatures in multicolor laser pulse collisions

Holger Gies[1,2], Felix Karbstein[1,2], and Leonhard Klar*[1,2]

[1]Helmholtz Institute Jena, Fröbelstieg 3, 07743 Jena, Germany; [2]Theoretisch-Physikalisches Institut, Abbe Center of Photonics, Friedrich-Schiller-Universität Jena,Max-Wien-Platz 1, 07743 Jena, Germany

Quantum vacuum fluctuations give rise to effective nonlinear interactions between electromagnetic fields. A prominent signature of quantum vacuum nonlinearities driven by macroscopic fields are signal photons differing in characteristic properties such as frequency and propagation direction from the driving fields. We devise a strategy for the efficient tracing of the various vacuum-fluctuation-mediated interaction processes in order to identify the most prospective signal photon channels. As an example, we study the collision of four optical laser pulses. We demonstrate how this information can be used to enhance the signal photon yield in laser pulse collisions for a given total laser energy.

The best tested quantum field theory is quantum electrodynamics. Nevertheless, it still predicts unobserved physics like the nonlinear interaction of strong electromagnetic fields mediated by quantum vacuum fluctuations. Formally, these interactions result from the one-loop Heisenberg-Euler effective Lagrangian and can be analyzed using the signal photon emission picture. They lead to signal photons encoding quantum vacum nonlinearities.

The basic idea is to look for these signal photons induced by several driving laser fields which differ in key properties from the photons constituting the latter. However, separating the typically small signal from the large background in general constitutes a major challenge. Aiming at a systematic enhancement of photonic quantum vacuum signals, a detailed knowledge about the microscopic origin of the prospective signal photon channels is indispensable. In Ref. [1], we demonstrated how their microscopic origin can be efficiently traced. Moreover, using a particular scenario envisioning the collision of several high-intensity laser pulses as an example, we have shown how this information can be used to enhance the signal photon yield for a given total laser energy.

To this end, we analytically decomposed the signal into so-called channels. These channels represent the influence of only three modes of the driving laser pulses, indicated by the indices $\ell = \{i, j, j\}$, on the signal. An illustrative example scenario envisions one $\omega_0 = 1.55\,\mathrm{eV}$ beam colliding with the apex of a regular pyramid formed by the beam axes of three additional laser beams with different frequencies ω_0, $2\omega_0$ and $4\omega_0$. The full density of signal photons $\rho(\varphi, \vartheta)$ with frequencies between $\mathrm{k_{min}}$ and $\mathrm{k_{max}}$ results from the signal photon density of the contributing channels $\rho_{\ell\ell'}(\varphi, \vartheta)$. By comparing these, it is possible to identify the origins of several promising signals. In Fig. 1 we depict the full signal photon density and highlight the signal with photon frequencies around $5\omega_0$ beyond the driving laser frequencies.

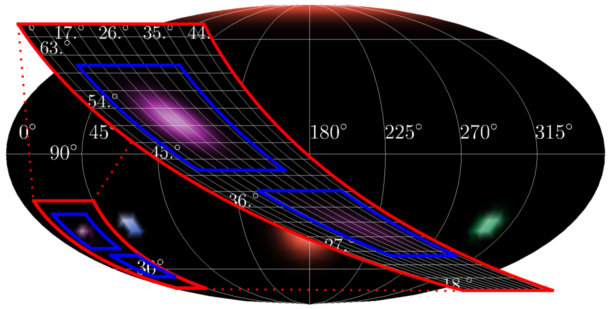

Figure 1: Mollweide plot (longitude φ, latitude ϑ) of the signal photon density signal photon density. We highlight the relevant angular domain (marked by a red frame) for scattered signal photon with energies in the regime $7.24\,\mathrm{eV}$ to $8.26\mathrm{eV}$; the linear violet color scale is normalized to its maximum in its frame. The other colors (red, green, blue) represent the frequencies ω_0, $2\omega_0$, $4\omega_0$.

Upon integration of the signal photon density over the two angular regimes highlighted in blue in Fig. 1, we obtain 2.3 (upper area) and 0.5 (lower area) signal photons per shot. Even in the frequency of the driving lasers we identify a scattering signal discernible from the background. We base our considerations on the availability of a single high-intensity laser of the ten petawatt class such as available at ELI-NP, see Ref. [2]. However, our results can straightforwardly be rescaled to other laser parameters.

Our method allows us to answer relevant questions, such as which laser beams participate in the formation of a given signal, and what is the specific interaction process inducing the latter. In addition, we have explicitly demonstrated how this information can be used to enhance the signal photon number in a given signal photon channel.

We are confident that the concepts outlined and applied in the present study will prove very useful in future attempts at optimizing photonic signatures of quantum vacuum nonlinearity for given experimental parameters and constraints.

The authors acknowledge funding from the DFG under Grant No. 416607684 and No. 416611371 within the Research Unit FOR2783/1.

References

[1] H. Gies, F. Karbstein, L. Klar, Phys. Rev. D **103**, 076009 (2021).

[2] ELI-NP: `https://www.eli-np.ro`

* `leonhard.klar@uni-jena.de`

Enhancing quantum vacuum signatures with tailored laser beams

Felix Karbstein*[1,2] and Elena A. Mosman[3]

[1]Helmholtz Institute Jena, Germany; [2]Theoretisch-Physikalisches Institut, FSU Jena, Germany; [3]National Research Tomsk Polytechnic University, Russia

We demonstrate that tailored laser beams provide a powerful means to make quantum vacuum signatures in strong electromagnetic fields accessible in experiment. Typical scenarios aiming at the detection of quantum vacuum nonlinearities at the high-intensity frontier envision the collision of focused laser pulses. The effective interaction of the driving fields mediated by vacuum fluctuations gives rise to signal photons encoding the signature of quantum vacuum nonlinearity. Isolating a small number of signal photons from the large background of the driving laser photons poses a major challenge. The main idea of the present work is to modify the far-field properties of a driving laser beam to exhibit a field-free hole in its center, thereby allowing for an essentially background free measurement of the signal scattered in the forward direction.

The advent of high-intensity laser facilities opens up the possibility of verifying QED vacuum nonlinearities in macroscopically controlled fields. All-optical signatures, i.e., effects driven by laser fields resulting in photonic signals, are the prime candidates for such discovery experiments. However, the large background of the driving laser photons typically constitutes a major obstacle in measuring the signal. In Ref. [1], we demonstrated that tailored laser beams featuring a peak in the focus where the interaction takes place, but a hole in the far field where the signal is measured allow to overcome these limitations.

To this end, we constructed a new class of beam solutions to the paraxial wave equation featuring a field-free hole in its transverse profile at a given longitudinal coordinate. More specifically, for this endeavor, we only considered a specific class of monochromatic laser fields of oscillation frequency ω, which are rotationally symmetric about the beam axis and are well-described by focused beam solutions of the paraxial wave equation: namely, linearly polarized laser fields without topological charge. These can be expressed as superposition of Laguerre-Gaussian $\mathrm{LG}_{p,l}$ modes with $l = 0$, but finite $p \in \mathbb{N}_0$.

Building on these results, we demonstrated the novel possibilities enabled by the use of beams featuring a peak in the focus but a hole in the far field for nonlinear QED experiments on the example of vacuum birefringence [2]. Replicating this scenario with probe beams featuring such properties seems particularly promising. In fact, it should facilitate an essentially background-free measurement of the signal photons scattered in the direction of the forward beam axis in a way not possible with conventional beams: while the focal spot of the probe photon field essentially

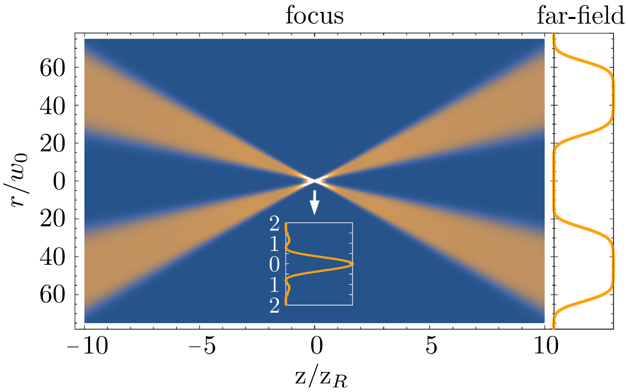

Figure 1: Laser intensity as function of the longitudinal coordinate z measured in units of the Rayleigh range z_R, and the radial distance r measured in units of the waist w_0. The inset shows the transverse focus profile; on the right we depict the far-field intensity profile.

does not differ from that of conventional beams, the driving probe photons are effectively diverted in the far field, leaving a field-free hole about the beam axis. On the other hand, the kinematics of the signal photons is determined by local properties of the driving fields in the interaction region about the beam focus, implying that the scattering phenomenon does not differ much from that induced by conventional beams. This results in signal photons quasi-elastically scattered in the direction of the beam axis. However, the hole in the far-field imprinted in the probe beam now allows for their unobstructed measurement.

Certainly, many other signatures of quantum vacuum nonlinearity can be critically enhanced by such tailored beams. This is especially true for scenarios based on the collision of high-intensity laser pulses, usually characterized by a paradox: while most signal photons arise from quasi-elastic scattering processes, for standard beams their measurement is typical obstructed by the background of the driving laser photons. Our study underpins that the use of tailored beams can change this and make quasi-elastically scattered signals experimentally accessible.

This work has been funded by the DFG under Grant No. 416607684 within the Research Unit FOR2783/1 and was supported by the DAAD "Mikhail Lomonosov" Program.

References

[1] F. Karbstein and E. A. Mosman, Phys. Rev. D **101**, 113002 (2020).

[2] J. S. Toll, Ph.D. thesis, Princeton University (1952).

*f.karbstein@hi-jena.gsi.de

Relativistic modified Bessel-Gaussian beam generation using plasma-based beam combination and guiding

B. Lei*[1], D. Seipt[1], M. Shi[1], B. Liu[1], J. Wang[2], M. Zepf[1], and S. Rykovanov[3]

[1]Helmholtz Institute Jena, Fröbelstieg 3, 07743 Jena, Germany; [2]SIOM, 201800 Shanghai, China ; [3]Skoltech CDISE, Moscow 121205, Russia

We theoretically and numerically demonstrate the generation of a relativistic modified Bessel-Gaussian optical beam (MBGB), an optical vortex beam (OVB),via plasma-based beam combining (PBC) in an underdense plasma channel. The plasma acts as laser-pulse-combiner by refractive guiding coupling, which results in the formation of a guided MBGB carrying large values of OAM. It is shown that the MBGB is stable in the plasma channel, allowing for in-situ applications in particle acceleration, extreme magnetic field generation, or novel radiation production. After leaving the plasma, the MBGB survives in vacuum for at least hundreds of femtoseconds. The tunability over the initial laser and plasma parameters enable the vortex beam to fit various applications.

We are proposing a new approach for generating relativistic OVB in a plasma from focused Gaussian beams, which promises high beam-quality for *in-situ* applications in the plasma. The method employs underdense micro-scale parabolic plasma channels, which have been widely used in plasma wakefield acceleration for stably guiding intense laser pulses well as for novel applications. It requires several intense Gaussian laser pulses equally arranged along a circle and obliquely injected into the plasma channel simultaneously. A schematic of the method with initially three Gaussian pulses is shown in Fig.1. Each of the Gaussians undergoes a helical centroid oscillation as

$$\boldsymbol{r} = \boldsymbol{\epsilon}\frac{r_{c0}}{2}e^{i\Omega_c\tau+i\psi} + c.c. \tag{1}$$

due to the transverse focusing force [1], if specific initial injection conditions are satisfied. Ω_c is the centroid oscillation frequency, r_{c0} is the oscillation amplitude, ψ is the transverse centroid tilt and the complex vector $\boldsymbol{\epsilon} = (1, \pm i)$. Being combined inside the plasma, the Gaussians are helically guided by optical refraction and together form a specific ultra-intense OVB, a modified Bessel Gaussian beam (MBGB), with normalized vector potential

$$\begin{aligned}\tilde{a}(r,\phi,\tau) &= \sum_{j=1}^{l}\tilde{a}_j(r,\phi,\tau)\\ &= C_0 l e^{-\frac{r^2}{w_0^2}}\sum_{n=-\infty}^{+\infty} I_{nl}\left(\frac{2r_{c0}r}{w_0^2}\right)e^{inl(\Omega_c\tau+\phi+\psi_0)}\end{aligned} \tag{2}$$

where the number of Gaussians l is chosen such that $l < 2\pi r_{c0}/w_0$ to avoid significant beam overlap and accompanying pulse-pulse interactions. $C_0 = a_0 e^{-r_{c0}^2/w_0^2}$, I_n are the modified Bessel functions of the first kind and ψ_0 represents the initial reference phase.

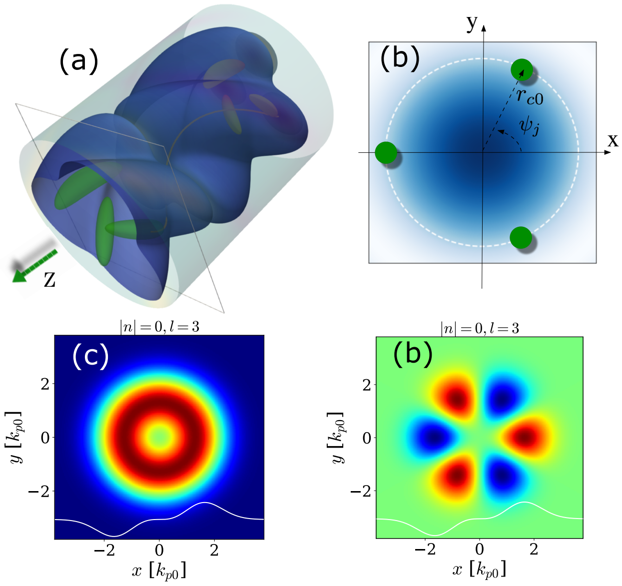

Figure 1: **(a)** Schematic of PBC scheme in parabolic plasma channel with three Gaussian pulses (green beamlets). Each pulse undergoes centroid oscillation around channel center along z-axis (green arrow) with a helical trajectory (orange line). A plasma wave is excited with twisted structure (blue surface). Electrons can be trapped and acclerated to form the structured beam (yellow beamlets at the back). **(b)** Transverse slice at the position indicated by the grey frame in (a). Transverse density gradient of the plasma channel is indicated by blue-white colour. **(c)-(d)** Numerical result of initial field structure of the first two sub vortex modes of the MBGB, $|n| = 0, 1$.

Such a vortex pulse enables various application in strong vortex field-plasma interaction, including particle acceleration, extreme magnetic field generation, electron vortex creation, radiation generation, and optical control of plasma wakefields.

This work was supported by the Helmholtz Association (Young Investigator's Group VH-NG-1037).

References

[1] S. G. Rykovanov *et al.*, Phys. Rev. Accel. Beams **19**, 090703 (2016).

*b.lei@hi-jena.gsi.de

Polarised QED Cascades

D. Seipt*[1,2], C. P. Ridgers[3], D. Del Sorbo[4], B. King[5], and A. G. R. Thomas[6]

[1]Helmholtz Institute Jena, Fröbelstieg 3, 07743 Jena, Germany; [2]GSI Helmholtzzentrum Darmstadt, Germany; [3]York Plasma Institute, UK; [4]SLAC National Accelerator Laboratory, USA; [5]University of Plymouth, UK; [6]CUOS, University of Michigan, USA.

We study the effect of particle polarization in the formation of QED cascades in ultra-high intensity laser fields. By including the spin and polarization of the electrons, positrons and photons in the strong-field QED processes of nonlinear Compton emission and pair production, we find that the growth rate of QED cascades are reduced, and the produced particles to be highly polarized. While the bulk of particles is polarized as expected from Sokolov-Ternov theory, the high-energy tails are polarized oppositely, which is a results of "spin-straggling".

One of the most striking predictions of strong-field QED was the formation of *avalanche*-like QED cascades [1] at laser intensities approaching 10^{24} W/cm^2. In these cascades, the prolific generation of high-energy photons and electron-positron pairs can convert an initially strong laser field into a hot and dense plasma of nearly solid density. Such cascades can be sustained in field configurations that allow an effective acceleration of leptons to $\chi_e \sim 1$ which then can emit photons with $\chi_\gamma \sim 1$ that can efficiently produce pairs. We address for the first time the effect of particle polarization on cascade formation [2].

The evolution of a cascade in a rotating electric field $\boldsymbol{E}(t)$ is modeled via a transport equation,

$$\left(\frac{\partial}{\partial t} + q\boldsymbol{E}(t)\cdot\nabla_{\boldsymbol{p}}\right) f_q^s(\boldsymbol{p},t) = \mathcal{C}_q^s[\{f_{q'}^{s'}\}]\,, \qquad (1)$$

for the one-particle distribution functions f_q^s, where the charge $q = 0, \pm 1$ distinguishes different particle species. In the rotating electric field, the existence of a global non-precessing spin basis perpendicular to the plane of the field to restrict the spin-polarization-dynamics to just two discrete states $s = \uparrow / \downarrow$ for leptons and $s = \parallel / \perp$ for the photons. Transitions between the different polarization states are possible only via the Boltzmann-type collision operators $\mathcal{C}_q^s$ which contain on the spin-and polarization resolved LCFA rates for nonlinear Compton scattering and nonlinear Breit-Wheeler pair production [3].

The classical advection in Eq. (1) is solved effectively using a semi-lagrangian algorithm since the characteristics are known analytically. Since ultrarelativistic particles emit collinearly, the simulation of quantum transitions is simplified by introducing $p = |\boldsymbol{p}|$ and $\varphi = \angle(\boldsymbol{E}(t), \boldsymbol{p})$, such that during the quantum step and only p changes for each $\varphi = const.$ independently.

In our simulations we found that the growth rate Γ of a polarized cascade is reduced compared to the case when

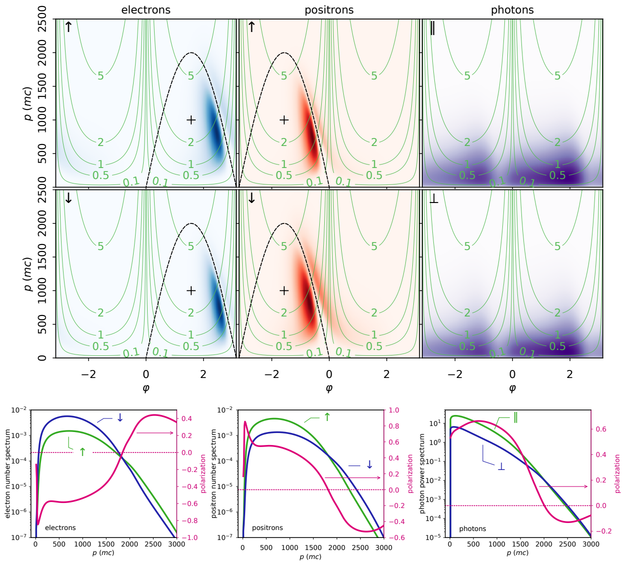

Figure 1: Upper: Distribution functions f_q^s for $a_0 = 1000$ and $\omega t = 10$. Green curves are χ isocontours. Lower: Spectra and corresponding degrees of polarization.

the particle polarization is neglected. For 800 nm lasers the maximum discrepancy was found to be 8% at around $a_0 = 600$. A much larger reduction of about 25 % was found for longer wavelengths [2]. Due to the exponentiation of the particle yield during cascade growth, $n \sim e^{\Gamma t}$, even a small reduction of Γ can reduce n by orders of magnitude.

Numerical results for the distribution functions f_q^s in the exponential growth phase of the cascade development are shown in Fig. 1. The spectra in the lower panels show that the bulk of electrons up to a momentum of $p \approx 2a_0$ are $\downarrow$-polarized (positrons $\uparrow$), as predicted by Sokolov-Ternov (S&T) theory. A factor of 4 times more $\parallel$-polarized photons are produced compared to $\perp$-polarized photons. In the high-energy tail above $p \gtrsim 2a_0$ the leptons are *polarized oppositely to S&T*. This effect cannot be explained alone by asymmetries in the pair production rates [3]. The majority of the anti-S&T behaviour is due to "spin-straggling", where the $\uparrow$-electrons are more likely to reach highest energies due to a lower probability of photon emission, i.e. spin-dependent quantum radiation reaction effects.

References

[1] A. R. Bell and J. G. Kirk, Phys. Rev. Lett. **101**, 200403 (2008).

[2] D. Seipt *et al.*, New J. Phys. **23**, 053025 (2021).

[3] D. Seipt and B. King, Phys. Rev. A **102**, 052805 (2020).

*d.seipt@hi-jena.gsi.de

Numerical Analysis of Poderomotive Scattering of Rarefied Xenon as a Means to Measure Relativistic Laser Strength in Focus

Thomas Teter*[1,2,3], Daniel Seipt[1,2], and Matt Zepf[1,2,3]

[1]Helmholtz Institute Jena, Germany; [2]GSI Darmstadt, Germany; [3]Friedrich-Schiller-Universität Jena, Germany

We examine the scattering of electrons sourced through ionization by relativistic laser pulses as a means to measure laser strength. For laser strengths between $a_0 = 5$ and 10, the energy levels of xenon correspond to peak field strengths. Using 3D EPOCH simulations, we find the angular spectra of electrons from rarefied gas and demonstrate the correlation between the rising edge of the spectrum and laser strength.

Relativistic laser facilities enabling strong-field QED experiments are increasing demand for high precision measurement of peak laser strength a_0 [1, 2]. One potential scheme for measuring the laser strength is examining the ponderomotive scattering of ionized electrons from rarefied gases. Previously, we had confirmed findings that heavier noble gases function well as scattering targets but saw a saturation trend of scattering angles for laser strengths above $a_0 \approx 6.8$ [3].

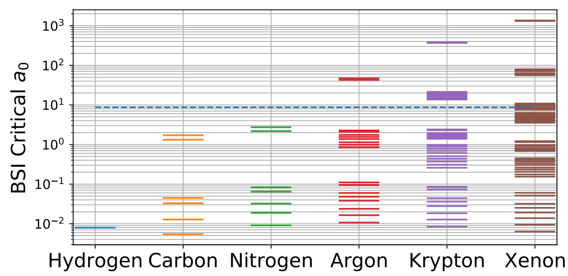

Figure 1: Laser strength a_0 associated with the barrier suppression ionization of a particular energy level for various elements in the relativistic regime. Blue dashed line is a laser peak strength of $a_0 = 8.76$.

Figure 1 shows how the laser strength corresponds to the energy levels of various gases in barrier suppression ionization. From the distribution of energy levels, we expect relevant Kr ionization to occur for a_0 between 1 and 3. Xe offers energy levels nearer to these higher laser strengths while lighter gases are fully ionized [4]. Using 3D EPOCH simulations, we investigate the ionization and subsequent ponderomotive scattering of electrons at various laser strengths. For $a_0 = 8.76$, Figure 2 shows the angular spectra of electrons for Kr and Xe. It is clear electrons from outer shells are scattered to larger angles θ which can be understood through the $\theta \approx \arctan 2/a_0$ relation. The Xe spectrum's prominent rising edge appears nearer to the predicted scattering angle for $a_0 = 8.76$ as its deeper energy levels have binding energies approximating that of the laser better than the closest levels of Kr.

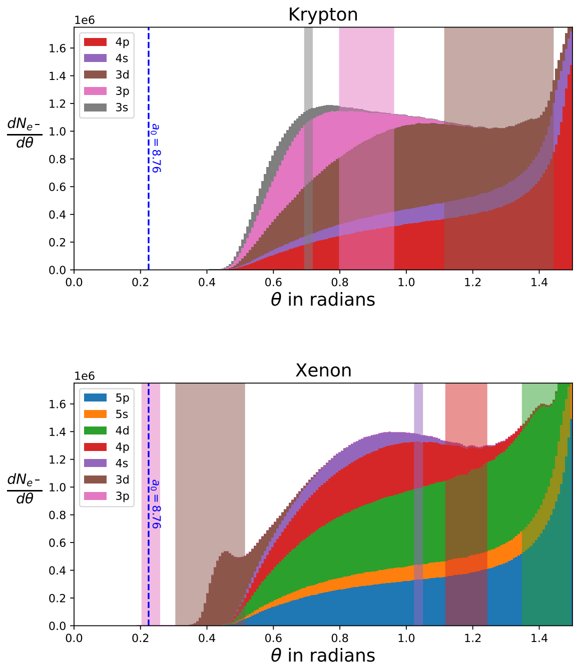

Figure 2: Numerical angular electron spectra for Kr and Xe scattered by a $\lambda = 800$ nm,$w_0 = 8\mu$m, $\tau = 27$ fs, and $a_0 = 8.76$ laser. Shaded regions are plane wave scattering angles corresponding the donor ionization shells. The blue line is the plane wave solution for the laser's a_0. The colored bars are electrons donated by particular energy levels.

Our results indicate the importance of choosing an appropriate gas target when attempting to measure laser strength through ponderomotive scattering. If (full) ionization of the target is achieved by lower intensity regions of the laser, the inverse tangent relation will greatly underestimate the peak laser strength as the dynamics cannot be modeled as a small correction applied to plane wave scattering. Our ongoing work includes investigating a generalization for how electrons born into the peak of a laser pulse deviate from plane wave scattering solutions.

References

[1] A. Blinne *et al.* Phys. Rev. D **99**, 17 (2019).

[2] H. Abramowicz *et al.* arXiv:2102.02032.

[3] M. Kalashnikov *et al.* Laser Part. Beams **33**, 361 (2015).

[4] A. Kramida *et al.* NIST Atomic Spectra Database (ver. 5.8), [Online]

* thomas.christopher.teter@uni-jena.de

Redefined vacuum approach and gauge-invariant subsets in two-photon-exchange diagrams for closed-shells system with a valence electron

R. N. Soguel*[1,2,3], A. V. Volotka[2, 3, 4], E. V. Tryapitsyna[5], D. A. Glazov[5], V. P. Kosheleva[1,2,3], and S. Fritzsche[1,2,3]

[1]Theoretisch-Physikalisches Institut, Friedrich-Schiller-Universität Jena, Germany; [2]Helmholtz Institute Jena, Germany; [3]GSI Helmholtzzentrum für Schwerionenforschung GmbH, Germany; [4]Department of Physics and Engineering, ITMO University, Russia; [5]Department of Physics, St. Petersburg State University, Russia

The two-photon-exchange diagrams for atoms with single valence electron are investigated. Calculation formulas are derived for an arbitrary state within the rigorous bound-state QED framework utilizing the redefined vacuum formalism. In contrast to other methods, the redefined vacuum approach enables the identification of eight gauge-invariant subsets and, thus, efficiently check the consistency of the obtained results. The gauge invariance of found subsets is demonstrated both analytically (for an arbitrary state) as well as numerically for $2s$, $2p_{1/2}$, and $2p_{3/2}$ valence electron in Li-like ions. Identifying gauge-invariant subsets in the framework of the proposed approach opens a way to tackle more complex diagrams, e.g., three-photon exchange, where the fragmentation on simpler subsets is crucial for its successful calculation.

The treatment of the interelectronic interaction remains a cornerstone for accurate theoretical predictions of the energy levels in many-electron atoms or ions. The relativistic many-body perturbation theory (MBPT) or configuration-interaction calculations usually treat the electron-electron interaction within the Breit approximation on the basis of the so-called *no-pair* Hamiltonian [1, 2]. However, the use of this approximation allows one to evaluate energy levels accurately only up to the order $(\alpha Z)^2$ in atomic units. Here, α is the fine structure constant and Z is the nuclear charge or *effective* charge in the case of the outer electrons. In order to account for higher-order effects, $O(\alpha^3 Z^3)$, one has to employ the bound-state quantum electrodynamics (QED) formalism.

Within the bound-state QED, the interelectronic interaction is usually treated perturbatively as an expansion over the number of exchanged photons. While the first-order contribution, that corresponds to the one-photon exchange, is relatively simple to deal with, most of the attention is paid to the next order, namely, the two-photon exchange. The two-photon exchange diagrams were first calculated in the milestone paper by Blundell et al. [3] for the ground state of He-like ions. The current experimental and theoretical developments recently reviewed by Indelicato [4] suggest the necessity to extend these computations also to other systems with more complicated electronic structures. An essential step towards this goal is to derive the computational formulas for the corresponding diagrams. All the derivations performed so far used zeroth-order many-electron wave-function constructed as a Slater determinant (or sum of Slater determinants) with all electrons involved [3, 5, 6]. Such a derivation becomes increasingly difficult for many-electron systems. The vacuum redefinition in QED, which is extensively used in MBPT to describe the states with many electrons involved, could be a path towards an extension of two-photon-exchange calculations to other ions and atoms.

The redefined vacuum approach within the bound-state QED is presented in detail in Ref. [7], where it is applied to the derivation of the one- and two-photon exchange corrections for atoms with one valence electron over closed-shells. The general formulae for the two-photon exchange correction are presented. The employment of the redefined vacuum approach allowed us to identify the gauge-invariant subsets at two- and three-electron diagrams and separate between the direct and exchange contributions at two-electron graphs. In total, we identified eight gauge-invariant subsets in the case of the original Furry picture. In the case of screening potential involved, additional three subsets are originated from the counterpotential diagrams. The gauge invariance of the identified subsets is verified analytically for three-electron terms and numerically for all of the subsets on the example of Li-like ions (see Tables in [7]). The possibility of checking the gauge invariance allows us to control the correctness of the derived expressions and verify the numerical calculations by comparing the results for each identified subset in different gauges. The presented redefined vacuum approach can be further employed for atoms with a more complicated electronic structure. Moreover, the identification of gauge-invariant contributions within this approach paves the way for calculating the higher-order corrections, which can be split into gauge-invariant subsets and tackled one after the other.

This work was supported by DFG (VO1707/1-3) and by RFBR (Grant No. 19-02-00974).

References

[1] R. N. Faustov, Theor. Math Phys. **3**, 478 (1970).

[2] J. Sucher, Phys. Rev. A **22**, 348 (1980).

[3] S. A. Blundell *et al*, Phys. Rev. A **48**, 2615 (1993).

[4] P. Indelicato, J. Phys. B **52**, 232001 (2019).

[5] V. M. Shabaev *et al*, *Phys. Rev. A* **49**, 4489 (1994).

[6] J. Sapirstein *et al*, Phys. Rev. A **91**, 062508 (2015).

[7] R. N. Soguel *et al*, Phys. Rev. A **103**, 042818 (2021).

*romain.soguel@uni-jena.de

G factor of lithiumlike silicon

V. P. Kosheleva[1,2], A. V. Volotka[3], D. A. Glazov[4], and S. Fritzsche[1,2]

[1]Helmholtz Institute Jena, 07743 Jena, Germany; [2]GSI Helmholtzzentrum für Schwerionenforschung GmbH, 64291 Darmstadt, Germany; [3]Department of Physics and Engineering, ITMO University, 197101 St. Petersburg, Russia; [4]Department of Physics, St. Petersburg State University, 199034 St. Petersburg, Russia

In the past decades, bound electron g factor of highly charged ions has been a subject of intense theoretical and experimental investigations. Nowadays, the bound electron g factor is measured with a relative accuracy of few parts 10^{-11} in H-like ions [1]. Present experimental techniques allow determining the value of g factor even in few-electron ions [2, 3] with unprecedented accuracy.

Due to such high accuracy which is achieved on the experimental as well as theoretical side the bound electron g factor provides an opportunity to probe various QED effects in strong electromagnetic field.

Just recently the experimental value of bound electron g factor in Li-like $^{28}\mathrm{Si}^{11+}$ was improved and currently it is the most accurate lithiumlike g factor [2] value. To match experimental precision, one should account for the various QED effects. Up to date the following progresses have been made in calculation of recoil [4, 5], screened QED [2, 6, 7], and interelectronic interaction [2, 6, 8] corrections. In recent theoretical calculation [2], the latter two corrections were evaluated within extended Furry picture formalism where the zeroth-order wave-functions are obtained from Dirac equation with effective screening potential. As a result, the obtained theoretical value of the g factor of $^{28}\mathrm{Si}^{11+}$ is $g_{\mathrm{th},2019} = 2.000\,889\,894\,4\,(34)$, what is 1.7σ from experimental value $g_{\mathrm{exp},2019} = 2.000\,889\,888\,450(139)$ [2].

In order to find out the source of this disagreement the screened and QED corrections to the bound electron g factor in $^{28}\mathrm{Si}^{11+}$ has been independently evaluated by Yerokhin and co-workers [7]. In this work, the calculations are performed in the usual Furry picture, i.e. based on the Dirac equation in Coulomb potential. In contrast to Ref. [2], the higher-order screening and multi-photon effects were calculated with the help of the NRQED (nonrelativistic quantum electrodynamics) approach. As a result, Yerokhin and co-workers have delivered a new theoretical value for the bound electron g factor $g_{\mathrm{th},2020} = 2.000\,889\,896\,3\,(15)$ which is still in agreement with Ref. [2] within the quoted error bars but disagrees by about 5σ with experiment.

To explain the disagreement between the theory and experiment established in Refs. [2, 7] we investigated in detail the two-photon exchange correction to the bound electron g factor of Li-like $^{28}\mathrm{Si}^{11+}$ ion. The calculations of this correction were performed in original as well as in extended Furry pictures. Also, we carefully analyse different ways of uncertainty estimation due to higher-order correlation effects. It was found that these higher-orders corrections are larger than estimations presented in Ref. [7]. As a result we deliver a new theoretical value (see Table 1) for the g factor $g_{\mathrm{th},2021} = 2.000\,889\,892\,2(34)$ of Li-like $^{28}\mathrm{Si}^{11+}$ which now is an agreement with the experimental result.

Table 1: Theoretical contribution to the ground-state g factor of Li-like $^{28}\mathrm{Si}^{11+}$. Preliminary results.

Effects		Reference
Dirac value (point nucleus)	$1.998\,254\,750\,7$	This work
QED, $\sim\alpha$	$0.002\,324\,043\,9$	[9, 10, 11]
QED, $\sim\alpha^2$	$-0.000\,003\,516\,6(3)$	[8, 12]
Interelectronic interaction	$0.000\,314\,809\,4(27)$	This work
Screened QED	$-0.000\,000\,241\,5(21)$	[2]
	$-0.000\,000\,236\,4(8)$	[7]
Finite nuclear size	$0.000\,000\,002\,6$	
Nuclear recoil	$0.000\,000\,043\,5$	[4, 5]
Total theory	$2.000\,889\,892\,0(34)$	This work
	$2.000\,889\,894\,4(34)$	[2]
	$2.000\,889\,896\,3(15)$	[7]
Measured g-factor	$2.000\,889\,888\,450(139)$	[2]

References

[1] S. Sturm, F. Köhler, J. Zatorski, A. Wagner, Z. Harman, G. Werth, W. Quint, C. H. Keitel, and K. Blaum, Nature **506**, 467 (2014).

[2] D. A. Glazov, F. Köhler-Langes, A. V. Volotka, K. Blaum, F. Heiße, G. Plunien, W. Quint, S. Rau, V. M. Shabaev, S. Sturm, G. Werth, Phys. Rev. Lett. **123**, 173001 (2019).

[3] I. Arapoglou, A. Egl, M. Höcker, T. Sailer, B. Tu, A. Weigel, R. Wolf, H. Cakir, V. A. Yerokhin, N. S. Oreshkina, et al., Phys. Rev. Lett. **122**, 253001 (2019).

[4] V. M. Shabaev, D. A. Glazov, A. V. Malyshev, and I. I. Tupitsyn, Phys. Rev. Lett. **119**, 263001 (2017).

[5] V. M. Shabaev, D. A. Glazov, A. V. Malyshev, and I. I. Tupitsyn, Phys. Rev. A **98**, 032512 (2018).

[6] A. V. Volotka, D. A. Glazov, V. M. Shabaev, I. I. Tupitsyn, and G. Plunien, Phys. Rev. Lett. **112**, 253004 (2014).

[7] V. A. Yerokhin, K. Pachucki, M. Puchalski, C. H. Keitel, and Z. Harman, Phys. Rev. A **102**, 022815 (2020).

[8] V. A. Yerokhin, K. Pachucki, M. Puchalski, Z. Harman, and C. H. Keitel, Phys. Rev. A **95**, 062511 (2017).

[9] D. A. Glazov, V. M. Shabaev, I. I. Tupitsyn, A. V. Volotka, V. A. Yerokhin, G. Plunien, and G. Soff, Phys. Rev. A **70**, 062104 (2004).

[10] R. N. Lee, A. I. Milstein, I. S. Terekhov, and S. G. Karshenboim, Phys. Rev. A **71**, 052501 (2005).

[11] V. A. Yerokhin and Z. Harman, Phys. Rev. A **95**, 060501(R) (2017).

[12] A. Czarnecki, M. Dowling, J. Piclum, and R. Szafron, Phys. Rev. Lett. **120**, 043203 (2018).

Enhanced entanglement from Ince-Gaussian pump beams in the spontaneous parametric down-conversion

Baghdasaryan Baghdasaryan*[1,2,3] and Stephan Fritzsche[1,3,4]

[1]Helmholtz Institute Jena, Germany; [2]Fraunhofer Institute for Applied Optics and Precision Engineering IOF, Germany; [3]Theoretisch-Physikalisches Institut, Friedrich-Schiller-Universität Jena, Germany; [4]Abbe Center of Photonics

In SPDC a nonlinear crystal is pumped with a laser to create entangled pairs of photons whose efficient control plays an essential role in various applications of quantum information processing. In particular, the amount of entanglement has been successfully controlled by adjusting the spatial structure of the incident pump field. Here, we theoretically analyzed how the entanglement of the down-converted two-photon state can be further enhanced by using Ince-Gaussian beams with well-defined *ellipticity* ϵ, i.e. solutions of the paraxial wave equation in elliptical coordinates. These spatially-structured beams are quite universal as they include both, the Laguerre-Gaussian beams for $\epsilon \to 0$ as well as the Hermite-Gaussian beams for $\epsilon \to \infty$. We demonstrated that the entanglement of the generated photon pairs in SPDC can be maximized by a proper choice of ϵ and that such an enhanced entanglement can be observed experimentally in terms of the Schmidt number.

The down-converted photons from SPDC can be entangled in either their time-bins, polarization, orbital angular momentum (OAM) or with regard to their radial wave vector [1], in dependence of how the set-up (geometry) is selected in a given experiment. It is therefore natural to ask how the state of the down-converted photons can be manipulated in order to enhance their entanglement. Apart from adjusting the properties of the crystal [1], the spatial structure of the incident pump beam can shape the two-photon state. For instance, an exponential pump beam has been used in order to flatten the OAM spectrum (spiral bandwidth) or a superposition of LG beams to generate a complete high-dimensional Bell basis.

In this work, we followed the last line and analyzed how the pump beam can be controlled in order to improve the entanglement of the generated two-photon state. Along this line, previous works have considered as a pump beam, for instance, the paraxial Hermite-Gaussian (HG) beams, Laguerre-Gaussian (LG) beams or superposition of LG and HG beams. HG and LG beams are well known as exact solutions for the free-space paraxial wave equation (PWE) in Cartesian and cylindrical coordinates. We instead considered a more general paraxial pump field, also known as Ince-Gaussian (IG) beam.

IG beams represent the exact, complete, and orthogonal solutions of the PWE in *elliptical* coordinates. Therefore, their transverse field distribution possess an inherent elliptical symmetry. Experimentally, the IG beams appear naturally as transverse eigenmodes of stable resonators but have been generated as well by means of liquid crystals.

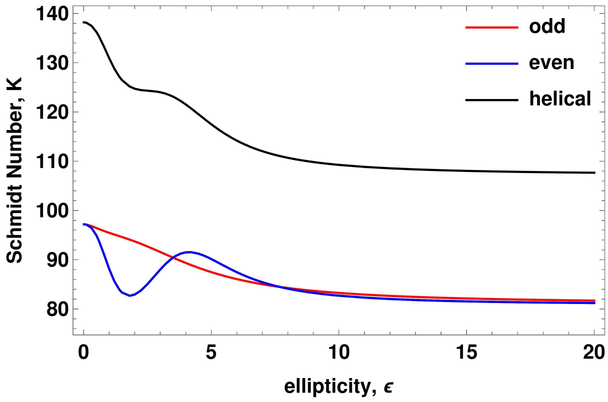

Figure 1: Dependence of the Schmidt number on the ellipticity of the incident IG beam. Odd, even and helical IG pump beams are denoted by red, dashed blue and black lines, respectively.

We explored the state of SPDC photons for different Ince-Gaussian (IG) pump beams and their different limits. Figure 1 shows the dependence of the Schmidt number on the ellipticity, when the pump beam is an IG and where beam widths of pump and down-converted beams are chosen to be equal. The proper choice of the kind (odd, even or helical) and ellipticity can maximize the amount of entanglement.

Our goal was to investigate the SPDC process for general paraxial pump fields, the (so-called) IG beam from which both, the paraxial LG are obtained for a zero ellipticity $\varepsilon \to 0$ as well as the HG beams for $\varepsilon \to \infty$. The shape of the pump beam is easily controlled using the ellipticity parameter. We showed how the entanglement of the SPDC two-photon states can be maximized by a proper choice of the ellipticity ε. We also show how the Schmidt number as an observable of such SPDC experiments can be utilized to better understand the amount of (generated) entanglement. The smooth transition of IG beams into LG beams has been analyzed in terms of the spiral bandwidth and the conservation (rule) of the OAM in the SPDC process.

References

[1] B. Baghdasaryan, B. Böning, W. Paufler, and S. Fritzsche Phys. Rev. A, **99**, 023403 (2019).

* baghdasar.baghdasaryan@uni-jena.de

Driven spin-chains as high-quality quantum routers

D. Wanisch*[1,2,3] and S. Fritzsche[1,2,3]

[1]Theoretisch-Physikalisches Institut, Friedrich-Schiller-Universität Jena, Germany; [2]Helmholtz Institute Jena, Germany; [3]GSI Helmholtzzentrum für Schwerionenforschung GmbH, Germany

Systems of trapped atomic ions are promising candidates for future quantum technologies, and the efficient simulation of quantum systems. In particular, models of interacting spin-1/2 degrees of freedom (qubits) can be efficiently implemented and simulated on these platforms. Here, we propose a setup, based on a periodically driven spin-chain, that can realize a high-quality quantum router. We present two protocols that can either generate highly entangled two-qubit states, or transfer single-qubit states with high fidelity over an arbitrary distance. Besides, we can execute several protocols at the same time, and store quantum states on the spin-chain. Our protocols exploit the effect of coherent destruction of tunneling to control, which spins on the chain couple to each other. This control is acquired by suitably shaping the external driving field. Our setup is scalable, robust against errors, and may be of practical use for future quantum information technologies.

The generation of entanglement and the transfer of quantum states over distance are two essential tasks for quantum information processing. A few years ago, Bose proposed to use an interacting network of spins to acquire these tasks [1]. That is, state transfer and entanglement generation are achieved by time-evolution under an appropriate Hamiltonian. The spin-network shall, therefore, serve as a transmission channel for quantum information. However, if the couplings among spins have a 'natural' form, the complexity of the system's dynamics grows with its size, and the quality of these tasks decreases accordingly. By quality, is meant how close the outcome of a given protocol is to the known optimum. To achieve the latter, the network, therefore, has to be tuned in a certain way.

$$\begin{aligned} \mathcal{H}(t) &= \mathcal{H}_0(t) + \mathcal{H}_\mathrm{I} , \\ \mathcal{H}_0(t) &= \sum_m f_m(t)\, S_m^z , \\ \mathcal{H}_\mathrm{I} &= -\frac{1}{2}\sum_{m,n} J_{mn}\left(S_m^+ S_n^- + S_m^- S_n^+\right) \end{aligned} \tag{1}$$

In this work, we consider a chain of spins that interact pairwise via an exchange coupling of the XY-type. The chain is subject to a driving field, which is periodic in time, see Eq. (1). Adjusting the local amplitudes of this field, and choosing the driving frequency sufficiently large (high-frequency limit), allows for complete control, whether two spins couple to each other or not. One can then use this control to decouple a sub-system of spins from the rest of the chain. The values of the respective couplings can be arbitrary as long as they are finite and much smaller than the driving frequency. Moreover, the distance between these two spins can be arbitrarily long, and their coupling strength determines the required time for the protocols to complete. Additionally, we can store a transferred state or an entangled pair on the chain. The protocols only require individual control over the two participating spins and are, therefore, well suited to be scaled up. Our analysis shows, the protocols are robust concerning potential errors in their setup. Furthermore, we can use the spin-chain to carry out multiple protocols at the same time. Our setup, hence, realizes a high-quality quantum router [2] and might serve as a fundamental building block of future quantum information devices that can route entanglement and quantum states between remote locations efficiently and robustly.

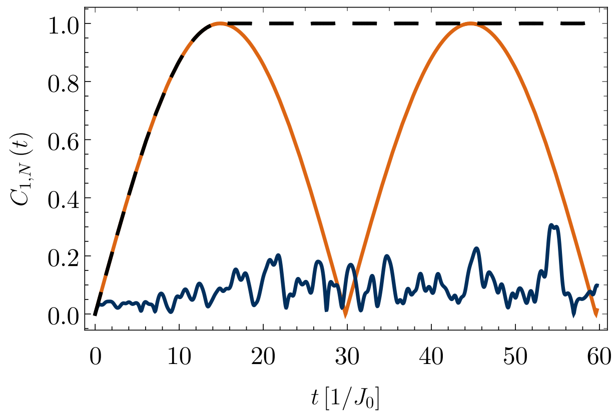

Figure 1: Time-evolution of the concurrence as a measure of entanglement between the edge-spins of a chain of length $N = 20$. Blue represents no periodic driving and orange represents the high-frequency limit. The dashed line shows the time evolution in the high-frequency limit when the field amplitude of one of the target-spins is changed, to store the entangled pair on the chain.

More details regarding this work can be found in [3].

References

[1] S. Bose, Phys. Rev. Lett. **91**, 207901 (2003).

[2] P. J. Pemberton-Ross and A. Kay, Phys. Rev. Lett., **106**, 020503 (2011).

[3] D. Wanisch and S. Fritzsche, Phys. Rev. A **102**, 032624 (2020).

* darvin.wanisch@uni-jena.de

PUBLICATIONS

V. P. Kosheleva, V. A. Zaytsev, R. A. Mueller, A. Surzhykov, and S. Fritzsche
Resonant two-photon ionization of atoms by twisted and plane-wave light
Physical Review A **102**, 063115 (2020).

F. Tuitje, P. Martinez Gil, T. Helk, J. Gautier, F. Tissandier, J.-P. Goddet, A. Guggenmos, U. Kleineberg, S. Sebban, E. Oliva, C. Spielmann, and M. Zuerch
Nonlinear ionization dynamics of hot dense plasma observed in a laser-plasma amplifier
Light: Science & Applications **9**, 187 (2020).

L. Stoyanov, M. Zhekova, A. Stefanov, I. Stefanov, G. G. Paulus, and A. Dreischuh
Zeroth- and first-order long range non-diffracting Gauss-Bessel beams generated by annihilating multiple-charged optical vortices
Scientific Reports **10**, 21981 (2020).

I. Tamer, M. Hornung, L. Lukas, M. Hellwing, S. Keppler, R. Van Hull, J. Hein, M. Zepf, and M. C. Kaluza
Characterization and application of nonlinear plastic materials for post-CPA pulse compression
Optics Letters **45**, 6575 (2020).

J. Wang, S. V. Bulanov, M. Chen, B. Lei, Y. Zhang, R. Zagidullin, V. Zorina, W. Yu, Y. Leng, R. Li, M. Zepf, and S. G. Rykovanov
Relativistic slingshot: A source for single circularly polarized attosecond x-ray pulses
Physical Review E **102**, 061201 (2020).

G. Torgrimsson
Nonlinear photon trident versus double Compton scattering and resummation of one-step terms
Physical Review D **102**, 116008 (2020).

M. A. Leutenegger, S. Kuehn, P. Micke, R. Steinbrugge, J. Stierhof, C. Shah, N. Hell, M. Bissinger, M. Hirsch, R. Ballhausen, M. Lang, C. Graefe, S. Wipf, R. Cumbee, G. L. Betancourt-Martinez, S. Park, V. A. Yerokhin, A. Surzhykov, W. C. Stolte, J. Niskanen, M. Chung, F. S. Porter, T. Stöhlker, T. Pfeifer, J. Wilms, G. V. Brown, J. R. C. López-Urrutia, and S. Bernitt
High-Precision Determination of Oxygen K-α Transition Energy Excludes Incongruent Motion of Interstellar Oxygen
Physical Review Letters **125**, 243001 (2020).

A. Steinkopff, C. Jauregui, C. Aleshire, A. Klenke, and J. Limpert
Impact of thermo-optical effects in coherently combined multicore fiber amplifiers
Optics Express **28**, 38093 (2020).

T. M. Ostermayr, C. Kreuzer, F. S. Englbrecht, J. Gebhard, J. Hartmann, A. Huebl, D. Haffa, P. Hilz, K. Parodi, J. Wenz, M. E. Donovan, G. Dyer, E. Gaul, J. Gordon, M. Martinez, E. Mccary, M. Spinks, G. Tiwari, B. M. Hegelich, and J. Schreiber
Laser-driven x-ray and proton micro-source and application to simultaneous single-shot bi-modal radiographic imaging
Nature Communications **11**, 6174 (2020).

R. W. Assmann, M. K. Weikum, T. Akhter, D. Alesini, A. S. Alexandrova, M. P. Anania, et. al.
EuPRAXIA Conceptual Design Report
European Physical Journal: Special Topics **229**, 3675 (2020).

E. Shestaev, S. Haedrich, N. Walther, T. Eidam, A. Klenke, Seres, Z. Bengery, P. Jojart, Z. Varallyay, A. Borzsonyi, and J. Limpert
Carrier-envelope offset stable, coherently combined ytterbium-doped fiber CPA delivering 1 kW of average power
Optics Letters **45**, 6350 (2020).

Y. M. Xing, J. Glorius, L. Varga, L. Bott, C. Brandau, B. Brueckner, R. J. Chen, X. Chen, S. Dababneh, T. Davinson, P. Erbacher, S. Fiebiger, T. Gassner, K. Goebel, M. Groothuis, A. Gumberidze, G. Gyurky, M. Heil, R. Hess, R. Hensch, P. Hillmann, P. -M. Hillenbrand, O. Hinrichs, B. Jurado, T. Kausch, A. Khodaparast, T. Kisselbach, N. Klapper, C. Kozhuharov, D. Kurtulgil, G. Lane, C. Langer, C. Lederer-Woods, M. Lestinsky, S. Litvinov, Y. A. Litvinov, B. Loeher, N. Petridis, U. Popp, M. Reed, R. Reifarth, M. S. Sanjari, H. Simon, Z. Slavkovska, U. Spillmann, M. Steck, T. Stoehlker, J. Stumm, T. Szucs, T. T. Nguyen, A. T. Zadeh, B. Thomas, S. Y. Torilov, H. Toernqvist, C. Trageser, S. Trotsenko, M. Volknandt, M. Wang, M. Weigand, C. Wolf, P. J. Woods, Y. H. Zhang, and X. H. Zhou
Determination of luminosity for in-ring reactions: A new approach for the low-energy domain
Nuclear Instruments & Methods In Physics Research Section A: Accelerators Spectrometers Detectors And Associated Equipment **982**, 164367 (2020).

M. Togawa, S. Kuehn, C. Shah, P. Amaro, R. Steinbruegge, J. Stierhof, N. Hell, M. Rosner, K. Fujii, M. Bissinger, R. Ballhausen, M. Hoesch, J. Seltmann, S. Park, F. Grilo, F. S. Porter, J. P. Santos, M. Chung, T. Stöhlker, J. Wilms, T. Pfeifer, G. V. Brown, M. A. Leutenegger, S. Bernitt, and J. R. Crespo López-Urrutia
Observation of strong two-electron-one-photon transitions in few-electron ions
Physical Review A **102**, 052831 (2020).

F. Roeder, M. Shalaby, B. Beleites, F. Ronneberger, and A. Gopal
THz generation by optical rectification of intense near-infrared pulses in organic crystal BNA
Optics Express **28**, 36274 (2020).

B. Grabiger, B. Marx-Glowna, I. Uschmann, R. Loetzsch, G. G. Paulus, and K. S. Schulze
A highly sensitive imaging polarimeter in the x-ray regime
Applied Physics Letters **117**, 201102 (2020).

S. Panahiyan and S. Fritzsche
Controllable simulation of topological phases and edge states with quantum walk
Physics Letters A **384**, 126828 (2020).

C. Grebing, M. Mueller, J. Buldt, H. Stark, and J. Limpert
Kilowatt-average-power compression of millijoule pulses in a gas-filled multi-pass cell
Optics Letters **45**, 6250 (2020).

B. Baghdasaryan and S. Fritzsche
Enhanced entanglement from Ince-Gaussian pump beams in spontaneous parametric down-conversion
Physical Review A **102**, 052412 (2020).

G. Torgrimsson
Nonlinear trident in the high-energy limit: Nonlocality, Coulomb field, and resummations
Physical Review D **102**, 096008 (2020).

B. Boening and S. Fritzsche
Partial-wave representation of the strong-field approximation
Physical Review A **102**, 053108 (2020).

D. Seipt and B. King
Spin- and polarization-dependent locally-constant-field-approximation rates for nonlinear Compton and Breit-Wheeler processes
Physical Review A **102**, 052805 (2020).

J. Deprince, M. A. Bautista, S. Fritzsche, J. A. Garcia, T. R. Kallman, C. Mendoza, P. Palmeri, and P. Quinet
Plasma environment effects on K lines of astrophysical interest IV. IPs, K thresholds, radiative rates, and Auger widths in Fe ii-Fe viii
Astronomy & Astrophysics **643**, A57 (2020).

Y. X. Geng, D. Wu, W. Yu, Z. M. Sheng, S. Fritzsche, Q. Liao, M. J. Wu, X. H. Xu, D. Y. Li, W. J. Ma, H. Y. Lu, Y. Y. Zhao, X. T. He, J. E. Chen, C. Lin, and X. Q. Yan
Proton beams from intense laser-solid interaction: Effects of the target materials
Matter And Radiation At Extremes **5**, 064402 (2020).

F. M. Kroeger, G. Weber, M. O. Herdrich, J. Glorius, C. Langer, Z. Slavkovska, L. Bott, C. Brandau, B. Brueckner, K. Blaum, X. Chen, S. Dababneh, T. Davinson, P. Erbacher, S. Fiebiger, T. Gassner, K. Goebel, M. Groothuis, A. Gumberidze, G. Gyurky, S. Hagmann, C. Hahn, M. Heil, R. Hess, R. Hensch, P. Hillmann, P-M Hillenbrand, O. Hinrichs, B. Jurado, T. Kausch, A. Khodaparast, T. Kisselbach, N. Klapper, C. Kozhuharov, D. Kurtulgil, G. Lane, C. Lederer-Woods, M. Lestinsky, S. Litvinov, Y. A. Litvinov, B. Loeher, F. Nolden, N. Petridis, U. Popp, M. Reed, R. Reifarth, M. S. Sanjari, H. Simon, U. Spillmann, M. Steck, J. Stumm, T. Szuecs, T. T. Nguyen, A. T. Zadeh, B. Thomas, S. Y. Torilov, H. Tornqvist, C. Trageser, S. Trotsenko, M. Volknandt, M. Weigand, C. Wolf, P. J. Woods, V. P. Shevelko, I. Y. Tolstikhina, and T. Stoehlker
Electron capture of Xe^{54+} in collisions with H_2 molecules in the energy range between 5.5 and 30.9 MeV/u
Physical Review A **102**, 042825 (2020).

Q. Lu, C. L. Yan, G. Q. Xu, N. Fu, Y. Yang, Y. Zou, A. V. Volotka, J. Xiao, N. Nakamura, and R. Hutton
Direct measurements for the fine-structure splitting of S VIII and Cl IX
Physical Review A **102**, 042817 (2020).

A. V. Volotka, A. Surzhykov, and S. Fritzsche
Rayleigh scattering of linearly polarized light: Scenario of the complete experiment
Physical Review A **102**, 042814 (2020).

S. Panahiyan, W. Chen, and S. Fritzsche
Fidelity susceptibility near topological phase transitions in quantum walks
Physical Review B **102**, 134111 (2020).

P. Boller, A. Zylstra, P. Neumayer, L. Bernstein, C. Brabetz, J. Despotopulos, J. Glorius, J. Hellmund, E. A. Henry, J. Hornung, J. Jeet, J. Khuyagbaatar, L. Lens, S. Roeder, T. Stoehlker, A. Yakushev, Y. A. Litvinov, D. Shaughnessy, V. Bagnoud, T. Kuehl, and D. H. G. Schneider
First on-line detection of radioactive fission isotopes produced by laser-accelerated protons
Scientific Reports **10**, 17183 (2020).

S. Schippers, A. Perry-Sassmannshausen, T. Buhr, M. Martins, S. Fritzsche, and A. Mueller
Multiple photodetachment of atomic anions via single and double core-hole creation
Journal Of Physics B: Atomic Molecular And Optical Physics **53**, 192001 (2020).

J. Sommerfeldt, R. A. Mueller, A. V. Volotka, S. Fritzsche, and A. Surzhykov
Vacuum polarization and finite-nuclear-size effects in the two-photon decay of hydrogen-like ions
Physical Review A **102**, 042811 (2020).

Z. W. Wu, Z. Q. Tian, J. Jiang, C. Z. Dong, and S. Fritzsche
Hyperfine-induced effects on angular emission of the magnetic-quadrupole line $1s2p_{3/2}\ {}^3P_2 \to 1s^2\ {}^1S_0$ following electron-impact excitation of Tl^{79+} ions
Physical Review A **102**, 042813 (2020).

R. V. Popov, V. M. Shabaev, D. A. Telnov, I. I. Tupitsyn, I. A. Maltsev, Y. S. Kozhedub, A. I. Bondarev, N. V. Kozin, X. Ma, G. Plunien, T. Stoehlker, D. A. Tumakov, and V. A. Zaytsev
How to access QED at a supercritical Coulomb field
Physical Review D **102**, 076005 (2020).

J. Hofbrucker, A. V. Volotka, J. Szlachetko, and S. Fritzsche
Enhanced polarization transfer to the characteristic L alpha x-ray lines near the nonlinear Cooper minimum of two-photon ionization
Physical Review A **102**, 042807 (2020).

M. Coughlan, H. Donnelly, N. Breslin, C. Arthur, G. Nersisyan, M. Yeung, B. Villagomez-Bernabe, M. Afshari, F. Currell, M. Zepf, and B. Dromey
Ultrafast dynamics and evolution of ion-induced opacity in transparent dielectrics
New Journal Of Physics **22**, 103023 (2020).

J. Koerner, M. Krueger, J. Reiter, A. Muenzer, J. Hein, and M. C. Kaluza
Temperature dependent spectroscopic study of Yb^{3+}-doped $KG(WO_4)_2$, $KY(WO_4)_2$, $YAlO_3$ and $YLiF_4$ for laser applications
Optical Materials Express **10**, 2425 (2020).

D. Wanisch and S. Fritzsche
Driven spin chains as high-quality quantum routers
Physical Review A **102**, 032624 (2020).

D. Wu, W. Yu, S. Fritzsche, and X. T. He
Particle-in-cell simulation method for macroscopic degenerate plasmas
Physical Review E **102**, 033312 (2020).

S. Panahiyan and S. Fritzsche
One-dimensional quantum walks driven by two-entangled-qubit coins
Physics Letters A **384**, 126673 (2020).

N. C. Geib, R. Hollinger, E. Haddad, P. Herrmann, F. Legare, T. Pertsch, C. Spielmann, M. Zuerch, and F. Eilenberger
Discrete dispersion scan setup for measuring few-cycle laser pulses in the mid-infrared
Optics Letters **45**, 5295 (2020).

F. Oppermann, P. Wustelt, T. Florin, S. Mhatre, S. Graefe, G. G. Paulus, and M. Lein
Dissociation and ionization of HeH^{+} in sub-cycle-controlled intense two-color fields
Journal Of Physics B: Atomic Molecular And Optical Physics **53**, 174001 (2020).

A. Descamps, B. K. Ofori-Okai, K. Appel, V. Cerantola, A. Comley, J. H. Eggert, L. B. Fletcher, D. O. Gericke, S. Goede, O. Humphries, O. Karnbach, A. Lazicki, R. Loetzsch, D. McGonegle, C. A. J. Palmer, C. Plueckthun, T. R. Preston, R. Redmer, D. G. Senesky, C. Strohm, I. Uschmann, T. G. White, L. Wollenweber, G. Monaco, J. S. Wark, J. B. Hastings, U. Zastrau, G. Gregori, S. H. Glenzer, and E. E. McBride
An approach for the measurement of the bulk temperature of single crystal diamond using an X-ray free electron laser
Scientific Reports **10**, 14564 (2020).

T. Kron, R. Beerwerth, S. Raeder, S. Fritzsche, R. Heinke, P. Schoenberg, M. Truemper, and K. Wendt
Hyperfine structure study of ^{97,98,99}Tc in a new laser ion source for high-resolution laser spectroscopy
Physical Review C **102**, 034307 (2020).

G. O'Neil, S. Sanders, P. Szypryt, Dipti, A. Gall, Y. Yang, S. M. Brewer, R. Doriese, J. Fowler, A. Naing, D. Swetz, J. Tan, J. Ullom, A. V. Volotka, E. Takacs, and Y. Ralchenko
Measurement of the $^{2}P_{1/2} -^{2} P_{3/2}$ fine-structure splitting in fluorinelike Kr, W, Re, Os, and Ir
Physical Review A **102**, 032803 (2020).

S. Tietze, M. Zepf, S. G. Rykovanov, and M. Yeung
Propagation effects in multipass high harmonic generation from plasma surfaces
New Journal Of Physics **22**, 093048 (2020).

J. Hofbrucker, L. Eiri, A. V. Volotka, and S. Fritzsche
Photoelectron Angular Distributions of Nonresonant Two-Photon Atomic Ionization Near Nonlinear Cooper Minima
Atoms **8**, 54 (2020).

J. Reiter, J. Koerner, J. Pejchal, A. Yoshikawa, J. Hein, and M. C. Kaluza
Temperature dependent absorption and emission spectra of $Tm:CaF_2$
Optical Materials Express **10**, 2142 (2020).

W. Eschen, G. Tadesse, Y. Peng, M. Steinert, T. Pertsch, J. Limpert, and J. Rothhardt
Single-shot characterization of strongly focused coherent XUV and soft X-ray beams
Optics Letters **45**, 4798 (2020).

C. Zhang, S. B. Schoun, C. M. Heyl, G. Porat, M. B. Gaarde, and J. Ye
Noncollinear Enhancement Cavity for Record-High Out-coupling Efficiency of an Extreme-UV Frequency Comb
Physical Review Letters **125**, 093902 (2020).

S. Panahiyan and S. Fritzsche
Simulation of novel cell-like topological structures with quantum walk
European Physical Journal Plus **135**, 626 (2020).

S. Chen, J. Chen, G. G. Paulus, and H. Kang
Strong-field frustrated double ionization of argon atoms
Physical Review A **102**, 023103 (2020).

L. Li, J. C. P. Koliyadu, H. Donnelly, D. Alj, O. Delmas, M. Ruiz-Lopez, O. de la Rochefoucauld, G. Dovillaire, M. Fajardo, C. Zhou, S. Ruan, B. Dromey, M. Zepf, and P. Zeitoun
High numerical aperture Hartmann wave front sensor for extreme ultraviolet spectral range
Optics Letters **45**, 4248 (2020).

D. Zille, D. Adolph, S. Skruszewicz, A. M. Sayler, and G. G. Paulus
Species-dependent tunneling ionization of weakly bound atoms in the short-wave infrared regime
New Journal Of Physics **22**, 083021 (2020).

M. Tschernajew, P. Gierschke, H. Lin, V. Hilbert, J. Kurdal, A. Stancalie, J. Limpert, and J. Rothhardt
Differential pumping unit for windowless coupling of laser beams to ultra high vacuum
Vacuum **178**, 109443 (2020).

D. Leimbach, J. Karls, Y. Guo, R. Ahmed, J. Ballof, L. Bengtsson, F. B. Pamies, A. Borschevsky, K. Chrysalidis, E. Eliav, D. Fedorov, V. Fedosseev, O. Forstner, N. Galland, R. F. G. Ruiz, C. Granados, R. Heinke, K. Johnston, A. Koszorus, U. Koster, M. K. Kristiansson, Y. Liu, B. Marsh, P. Molkanov, L. F. Pasteka, J. P. Ramos, E. Renault, M. Reponen, A. Ringvall-Moberg, R. E. Rossel, D. Studer, A. Vernon, J. Warbinek, J. Welander, K. Wendt, S. Wilkins, D. Hanstorp, and S. Rothe
The electron affinity of astatine
Nature Communications **11**, 3824 (2020).

V. Dinu and G. Torgrimsson
Approximating higher-order nonlinear QED processes with first-order building blocks
Physical Review D **102**, 016018 (2020).

H. Kang, A. S. Maxwell, D. Trabert, X. Lai, S. Eckart, M. Kunitski, M. Schoeffler, T. Jahnke, X. Bian, R. Doerner, and C. F. de Morisson Faria
Holographic detection of parity in atomic and molecular orbitals
Physical Review A **102**, 013109 (2020).

H. Gies and J. Ziebell
Asymptotically safe QED
European Physical Journal C **80**, 607 (2020).

C. Aleshire, A. Steinkopff, C. Jauregui, A. Klenke, A. Tuennermann, and J. Limpert
Simplified design of optical elements for filled-aperture coherent beam combination
Optics Express **28**, 21035 (2020).

N. S. Scott, A. Hibbert, J. Ballantyne, S. Fritzsche, A. L. Hazel, D. P. Landau, D. W. Walker, and Z. Was
CPC's 50th Anniversary: Celebrating 50 years of open-source software in computational physics
Computer Physics Communications **252**, 107269 (2020).

C. Jauregui, C. Stihler, and J. Limpert
Transverse mode instability
Advances In Optics And Photonics **12**, 429 (2020).

A. S. Mayer, W. Grosinger, J. Fellinger, G. Winkler, L. W. Perner, S. Droste, S. H. Salman, C. Li, C. M. Heyl, I. Hartl, and O. H. Heckl
Flexible all-PM NALM Yb:fiber laser design for frequency comb applications: operation regimes and their noise properties
Optics Express **28**, 18946 (2020).

I. Tamer, M. Hellwing, Y. Azamoum, M. Hornung, S. Keppler, F. Schorcht, J. Hein, and M. C. Kaluza
Few-cycle fs-pumped NOPA with passive ultrabroadband spectral shaping
Optics Express **28**, 19034 (2020).

H. P. Kang, S. Chen, W. Chu, J. P. Yao, J. Chen, X. J. Liu, Y. Cheng, and Z. Z. Xu
Nonsequential double ionization of alkaline-earth metal atoms by intense mid-infrared femtosecond pulses
Optics Express **28**, 19325 (2020).

F. Karbstein and E. A. Mosman
Enhancing quantum vacuum signatures with tailored laser beams
Physical Review D **101**, 113002 (2020).

H. Bernhardt, A. T. Schmitt, B. Grabiger, B. Marx-Glowna, R. Loetzsch, Hans-Christian Wille, D. Bessas, A. I. Chumakov, R. Rueffer, R. Roehlsberger, T. Stoehlker, I. Uschmann, G. G. Paulus, and K. S. Schulze
Ultra-high precision x-ray polarimetry with artificial diamond channel cuts at the beam divergence limit
Physical Review Research **2**, 023365 (2020).

F. Tuitje, W. Eschen, G. K. Tadesse, J. Limpert, J. Rothhardt, and C. Spielmann
Reliability of ptychography on periodic structures
OSA Continuum **3**, 1691 (2020).

S. H. Hendi, A. M. Tavakkoli, S. Panahiyan, B. E. Panah, and E. Hackmann
Simulation of geodesic trajectory of charged BTZ black holes in massive gravity
European Physical Journal C **80**, 524 (2020).

E. Lindroth, Orban, S. Trotsenko, and R. Schuch
Electron-impact recombination and excitation rates for charge-state-selected highly charged Si ions
Physical Review A **101**, 062706 (2020).

D. Samoilenko, A. V. Volotka, and S. Fritzsche
Elastic Photon Scattering on Hydrogenic Atoms near Resonances
Atoms **8**, 12 (2020).

M. Mueller, C. Aleshire, A. Klenke, E. Haddad, F. Legare, A. Tuennermann, and J. Limpert
10.4 kW coherently combined ultrafast fiber laser
Optics Letters **45**, 3083 (2020).

S. Kuehn, C. Shah, J. R. C. Lopez-Urrutia, K. Fujii, R. Steinbruegge, J. Stierhof, M. Togawa, Z. Harman, N. S. Oreshkina, C. Cheung, M. G. Kozlov, S. G. Porsev, M. S. Safronova, J. C. Berengut, M. Rosner, M. Bissinger, R. Ballhausen, N. Hell, S. Park, M. Chung, M. Hoesch, J. Seltmann, A. S. Surzhykov, V. A. Yerokhin, J. Wilms, F. S. Porter, T. Stoehlker, C. H. Keitel, T. Pfeifer, G. V. Brown, M. A. Leutenegger, and S. Bernitt
High Resolution Photoexcitation Measurements Exacerbate the Long-Standing Fe XVII Oscillator Strength Problem
Physical Review Letters **124**, 225001 (2020).

S. Cousens, M. Yeung, M. Zepf, and B. Dromey
Electron trajectories associated with laser-driven coherent synchrotron emission at the front surface of overdense plasmas
Physical Review E **101**, 053210 (2020).

H. Kang, S. Chen, Z. Lin, W. Chu, J. Yao, W. Quan, J. Chen, X. Liu, Y. Cheng, and Z. Xu
Comparative study of strong-field ionization of alkaline-earth-metal atoms
Physical Review A **101**, 053433 (2020).

D. Wu, W. Yu, Z. M. Sheng, S. Fritzsche, and X. T. He
Uniform warm dense matter formed by direct laser heating in the presence of external magnetic fields
Physical Review E **101**, 051202 (2020).

P. Balla, A. Bin Wahid, I. Sytcevich, C. Guo, Anne-Lise Viotti, L. Silletti, A. Cartella, S. Alisauskas, H. Tavakol, U. Grosse-Wortmann, A. Schoenberg, M. Seidel, A. Trabattoni, B. Manschwetus, T. Lang, F. Calegari, A. Couairon, A. L'Huillier, C. L. Arnold, I. Hartl, and C. M. Heyl
Postcompression of picosecond pulses into the few-cycle regime
Optics Letters **45**, 2572 (2020).

A. McIlvenny, H. Ahmed, C. Scullion, D. Doria, L. Romagnani, P. Martin, K. Naughton, A. Sgattoni, D. R. Symes, A. Macchi, P. McKenna, M. Zepf, S. Kar, and M. Borghesi
Characteristics of ion beams generated in the interaction of ultra-short laser pulses with ultra-thin foils
Plasma Physics And Controlled Fusion **62**, 054001 (2020).

B. Baghdasaryan, F. Steinlechner, and S. Fritzsche
Characterization of opening angle correlations of a biphoton state decomposed in Bessel modes
Physical Review A **101**, 043844 (2020).

E. Appi, C. C. Papadopoulou, J. L. Mapa, N. Wesavkar, C. Jusko, P. Mosel, S. Alisauskas, T. Lang, C. M. Heyl, B. Manschwetus, M. Brachmanski, M. Braune, H. Lindenblatt, F. Trost, S. Meister, P. Schoch, R. Treusch, R. Moshammer, I. Hartl, U. Morgner, and M. Kovacev
A synchronized VUV light source based on high-order harmonic generation at FLASH
Scientific Reports **10**, 6867 (2020).

X. Xu, Y. Zhang, H. Zhang, H. Lu, W. Zhou, C. Zhou, B. Dromey, S. Zhu, M. Zepf, X. He, and B. Qiao
Production of 100-TW single attosecond x-ray pulse
Optica **7**, 355 (2020).

S. Kosugi, F. Koike, T. Nagayasu, F. Hosseini, J. Martins, T. Marchenko, O. Travnikova, M. Oura, T. Gejo, J. R. Harries, J. D. Bozek, K. Ito, E. Sokell, S. Fritzsche, M. N. Piancastelli, M. Simon, and Y. Azuma
Strong configuration interaction in the 3p photoelectron spectrum of Kr
Physical Review A **101**, 042505 (2020).

V. Hilbert, M. Tschernajew, R. Klas, J. Limpert, and J. Rothhardt
A compact, turnkey, narrow-bandwidth, tunable, and high-photon-flux extreme ultraviolet source
AIP Advances **10**, 045227 (2020).

K. Schoenberg, Bagnoud, A. Blazevic, V. E. Fortov, D. O. Gericke, A. Golubev, D. H. H. Hoffmann, D. Kraus, I. V. Lomonosov, Mintsev, S. Neff, P. Neumayer, A. R. Piriz, R. Redmer, O. Rosmej, M. Roth, T. Schenkel, B. Sharkov, N. A. Tahir, D. Varentsov, and Y. Zhao
High-energy-density-science capabilities at the Facility for Antiproton and Ion Research
Physics Of Plasmas **27**, (2020).

Y. Zhang, D. Zille, D. Hoff, P. Wustelt, D. Wuerzler, M. Moeller, A. M. Sayler, and G. G. Paulus
Observing the Importance of the Phase-Volume Effect for Few-Cycle Light-Matter Interactions
Physical Review Letters **124**, 133202 (2020).

D. Wuerzler, S. Skruszewicz, A. M. Sayler, D. Zille, M. Moeller, P. Wustelt, Y. Zhang, J. Tiggesbaeumker, and G. G. Paulus
Accurate retrieval of ionization times by means of the phase-of-the-phase spectroscopy, and its limits
Physical Review A **101**, 033416 (2020).

V. P. Kosheleva, A. V. Volotka, D. A. Glazov, and S. Fritzsche
Many-electron effects in the hyperfine splitting of lithiumlike ions
Physical Review Research **2**, 013364 (2020).

V. Dinu and G. Torgrimsson
Trident process in laser pulses
Physical Review D **101**, 056017 (2020).

Y. X. Zhang, S. Rykovanov, M. Shi, C. L. Zhong, X. T. He, B. Qiao, and M. Zepf
Giant Isolated Attosecond Pulses from Two-Color Laser-Plasma Interactions
Physical Review Letters **124**, 114802 (2020).

B. Boening, W. Paufler, and S. Fritzsche
Polarization-dependent high-intensity Kapitza-Dirac effect in strong laser fields
Physical Review A **101**, 031401 (2020).

J. Deprince, M. A. Bautista, S. Fritzsche, J. A. Garcia, T. R. Kallman, C. Mendoza, P. Palmeri, and P. Quinet
Plasma-environment effects on K lines of astrophysical interest III. IPs, K thresholds, radiative rates, and Auger widths in Fe IX - Fe XVI
Astronomy & Astrophysics **635**, A70 (2020).

R. Klas, W. Eschen, A. Kirsche, J. Rothhardt, and J. Limpert
Generation of coherent broadband high photon flux continua in the XUV with a sub-two-cycle fiber laser
Optics Express **28**, 6188 (2020).

R. Hollinger, D. Hoff, P. Wustelt, S. Skruszewicz, Y. Zhang, H. Kang, D. Wuerzler, T. Jungnickel, M. Dumergue, A. Nayak, R. Flender, L. Haizer, M. Kurucz, B. Kiss, S. Kuhn, E. Cormier, C. Spielmann, G. G. Paulus, P. Tzallas, and M. Kuebel
Carrier-envelope-phase measurement of few-cycle mid-infrared laser pulses using high harmonic generation in ZnO
Optics Express **28**, 7314 (2020).

M. B. Schwab, E. Siminos, T. Heinemann, D. Ullmann, F. Karbstein, S. Kuschel, A. Saevert, M. Yeung, D. Hollatz, A. Seidel, J. Cole, S. P. D. Mangles, B. Hidding, M. Zepf, S. Skupin, and M. C. Kaluza
Visualization of relativistic laser pulses in underdense plasma
Physical Review Accelerators And Beams **23**, 032801 (2020).

M. Afshari, J. Hornung, A. Kleinschmidt, P. Neumayer, D. Bertini, and Bagnoud
Proton acceleration via the TNSA mechanism using a smoothed laser focus
AIP Advances **10**, 035023 (2020).

C. Hahn, E. Menz, P. Pfaefflein, G. Weber, and T. Stoehlker
A scintillator-based particle detector for CRYRING@ESR
X-ray Spectrometry **49**, 338 (2020).

P.-M. Hillenbrand, S. Hagmann, M. E. Groshev, D. Banas, E. P. Benis, C. Brandau, E. De Filippo, O. Forstner, J. Glorius, R. E. Grisenti, A. Gumberidze, D. L. Guo, B. Hai, M. O. Herdrich, M. Lestinsky, Y. A. Litvinov, E. V. Pagano, N. Petridis, M. S. Sanjari, D. Schury, U. Spillmann, S. Trotsenko, M. Vockert, G. Weber, V. A. Yerokhin, and T. Stoehlker
Radiative electron capture to the continuum in $U^{89+} + N_2$ collisions: Experiment and theory
Physical Review A **101**, 022708 (2020).

J. Hofbrucker, A. V. Volotka, and S. Fritzsche
Breakdown of the electric dipole approximation at Cooper minima in direct two-photon ionisation
Scientific Reports **10**, 3617 (2020).

A. Perry-Sassmannshausen, T. Buhr, A. Borovik Jr., M. Martins, S. Reinwardt, S. Ricz, S. O. Stock, F. Trinter, A. Mueller, S. Fritzsche, and S. Schippers
Multiple Photodetachment of Carbon Anions via Single and Double Core-Hole Creation
Physical Review Letters **124**, 083203 (2020).

N. Dimitrov, M. Zhekova, G. G. Paulus, and A. Dreischuh
Inverted field interferometer for measuring the topological charges of optical vortices carried by short pulses
Optics Communications **456**, 124530 (2020).

R. Hollinger, D. Gupta, M. Zapfl, M. Karst, R. Roeder, I. Uschmann, U. Reisloehner, D. Kartashov, C. Ronning, and C. Spielmann
Polarization dependent multiphoton absorption in ZnO thin films
Journal of Physics D **53**, 055102 (2020).

D. Dmytriiev, M. S. Sanjari, Y. A. Litvinov, and T. Stoehlker
Position sensitive resonant Schottky cavities for heavy ion storage rings
Nuclear Instruments & Methods In Physics Research Section B: Beam Interactions With Materials And Atoms **463**, 320 (2020).

S. Schippers, T. Buhr, A. Borovik Jr., K. Holste, A. Perry-Sassmannshausen, K. Mertens, S. Reinwardt, M. Martins, S. Klumpp, K. Schubert, S. Bari, R. Beerwerth, S. Fritzsche, S. Ricz, J. Hellhund, and A. Mueller
The photon-ion merged-beams experiment PIPE at PETRA III-The first five years
X-ray Spectrometry **49**, 11 (2020).

F. M. Kroeger, G. Weber, V. P. Shevelko, S. Hirlaender, M. W. Krasny, and T. Stoehlker
Charge state tailoring of relativistic heavy ion beams for the Gamma Factory project at CERN
X-ray Spectrometry **49**, 25 (2020).

J. Deprince, M. Bautista, S. Fritzsche, J. Garcia, T. Kallman, C. Mendoza, P. Palmeri, and P. Quinet
K-line X-ray fluorescence from highly charged iron ions under dense astrophysical plasma conditions
X-ray Spectrometry **49**, 29 (2020).

R. Sanchez, A. Braeuning-Demian, J. Glorius, S. Hagmann, Pierre-Michel Hillenbrand, A. Kalinin, T. Kohler, Y. A. Litvinov, N. Petridis, S. Sanjari, U. Spillmann, and T. Stoehlker
Towards experiments with highly charged ions at HESR
X-ray Spectrometry **49**, 33 (2020).

V. A. Agababaev, D. A. Glazov, A. V. Volotka, D. V. Zinenko, V. M. Shabaev, and G. Plunien
g factor of the $[(1s)^2(2s)^2 2p]\ ^2P_{3/2}$ state of middle-Z boronlike ions
X-ray Spectrometry **49**, 143 (2020).

J. Rothhardt, M. Bilal, R. Beerwerth, A. V. Volotka, Hilbert, T. Stoehlker, S. Fritzsche, and J. Limpert
Lifetime measurements of ultrashort-lived excited states in Be-like ions
X-ray Spectrometry **49**, 165 (2020).

N. Stallkamp, S. Ringleb, B. Arndt, M. Kiffer, S. Kumar, T. Morgenroth, G. G. Paulus, W. Quint, T. Stoehlker, and M. Vogel
HILITE-A tool to investigate interactions of matter and light
X-ray Spectrometry **49**, 188 (2020).

J. Hornung, Y. Zobus, P. Boller, C. Brabetz, U. Eisenbarth, T. Kuehl, Z. Major, J. B. Ohland, M. Zepf, B. Zielbauer, and Bagnoud
Enhancement of the laser-driven proton source at PHELIX
High Power Laser Science And Engineering **8**, e24 (2020).

E. Shestaev, D. Hoff, A. M. Sayler, A. Klenke, S. Haedrich, F. Just, T. Eidam, P. Jojart, Z. Varallyay, K. Osvay, G. G. Paulus, A. Tuennermann, and J. Limpert
High-power ytterbium-doped fiber laser delivering few-cycle, carrier-envelope phase-stable 100 μJ pulses at 100 kHz
Optics Letters **45**, 97 (2020).

S. Panahiyan
Nonlinearly charged dyonic black holes
Nuclear Physics B **950**, 114831 (2020).

J. Buldt, M. Mueller, H. Stark, C. Jauregui, and J. Limpert
Fiber laser-driven gas plasma-based generation of THz radiation with 50-mW average power
Applied Physics B **126**, 2 (2020).

G. Weber, A. Gumberidze, M. O. Herdrich, R. Maertin, U. Spillmann, A. Surzhykov, D. B. Thorn, S. Trotsenko, N. Petridis, C. J. Fontes, and T. Stoehlker
Towards a determination of absolute cross sections for projectile excitation of hydrogen-like uranium in collisions with neutral atoms
X-ray Spectrometry **49**, 239 (2020).

T. Gassner, A. Gumberidze, M. Trassinelli, R. Hess, U. Spillmann, D. Banas, K. -H. Blumenhagen, F. Bosch, C. Brandau, W. Chen, C. Dimopoulou, E. Foertser, R. E. Grisenti, S. Hagmann, P. -M. Hillenbrand, P. Indelicato, P. Jagodzinski, T. Kaempfer, M. Lestinsky, D. Liesen, Y. A. Litvinov, R. Loetzsch, B. Manil, R. Maertin, F. Nolden, N. Petridis, M. S. Sanjari, K. S. Schulze, M. Schwemlein, A. Simionovici, M. Steck, T. Stoehlker, C. I. Szabo, S. Trotsenko, I. Uschmann, G. Weber, O. Wehrhan, N. Winckler, D. F. A. Winters, N. Winters, E. Ziegler, and H. F. Beyer
High-resolution wavelength-dispersive spectroscopy of K-shell transitions in hydrogen-like gold
X-ray Spectrometry **49**, 204 (2020).

O. Forstner, D. Bemmerer, T. E. Cowan, R. Dressler, A. R. Junghans, D. Schumann, T. Stoehlker, T. Szuecs, A. Wagner, and K. Zuber
Opportunities for measurements of astrophysical-relevant alpha-capture reaction rates at CRYRING@ESR
X-ray Spectrometry **49**, 129 (2020).

S. Hagmann, Pierre-Michel Hillenbrand, Y. A. Litvinov, U. Spillmann, and T. Stoehlker
A magnetic spectrometer for electron-positron pair spectroscopy in storage rings
X-ray Spectrometry **49**, 115 (2020).

M. O. Herdrich, A. Fleischmann, D. Hengstler, S. Allgeier, C. Enss, S. Trotsenko, T. Morgenroth, R. Schuch, G. Weber, and T. Stoehlker
High-precision X-ray spectroscopy of Fe ions in an EBIT using a micro-calorimeter detector: First results
X-ray Spectrometry **49**, 184 (2020).

P. Wustelt, M. Kübel, G. Paulus, and A. Sayler
Strong-field laser-induced fragmentation of small molecules from fast to slow
Advances in Atomic, Molecular and Optical Physics **69**, 67 (2020).

V. Zaytsev, A. Surzhykov, V. Serbo, V. Kosheleva, M. Groshev, V. Yerokhin, V. Shabaev, and T. Stöhlker
Atomic processes with twisted electrons
Journal of Physics: Conference Series **1412**, 052013 (2020).

M. Kiffer, S. Ringleb, N. Stallkamp, S. Kumar, B. Arndt, M. Vogel, W. Quint, and T. Stöhlker
Characterisation of ion bunches by a single-pass non-destructive charge counter
Journal of Physics: Conference Series **1412**, 242004 (2020).

S. Hagmann, P. Hillenbrand, Y. Litvinov, U. Spillmann, and T. Stöhlker
Coincident mapping of e+and e-from free-free pair production in a magnetic toroidal lepton spectrometer
Journal of Physics: Conference Series **1412**, 232004 (2020).

P. Jagodziłski, D. Banaś, M. Pajek, A. Warczak, H. Beyer, A. Gumberidze, G. Weber, Th. Stöhlker, and M. Trassinelli
Concept and simulations of a high-resolution asymmetric von Hamos X-ray spectrometer for CRYRING@ESR electron cooler
Journal of Physics: Conference Series **1412**, 132031 (2020).

A. Borovik, G. Weber, V. Hilbert, H. Lin, P. Pfäfflein, B. Zhu, C. Hahn, M. Lestinsky, S. Schippers, Th. Stöhlker, and J. Rothhardt
Development of a detector to register low-energy, charge-changed ions from ionization experiments at CRYRING@ESR
Journal of Physics: Conference Series **1412**, 242003 (2020).

N. Stallkamp, S. Ringleb, B. Arndt, M. Kiffer, S. Kumar, G. Paulus, W. Quint, T. Stöhlker, and M. Vogel
HILITE-A well-defined ion target for laser experiments
Journal of Physics: Conference Series **1412**, 092009 (2020).

A. Gumberidze, C. Kozhuharov, R. Zhang, S. Trotsenko, Y. Kozhedub, R. Du, H. Bois, F. Beyer, K.-H. Blumenhagen, C. Brandau, A. Bräuning-Demian, W. Chen, O. Forstner, B. Gao, T. Gassner, R. Grisenti, S. Hagmann, P.-M. Hillenbrand, P. Indelicato, A. Kumar, M. Lestinsky, Y. Litvinov, N. Petridis, D. Schury, U. Spillmann, C. Trageser, M. Trassinelli, X. Tu, and T. Stöhlker
Impact parameter sensitive study of inner-shell atomic processes in Xe^{54+}, Xe^{52+} $\rightarrow$ Xe collisions
Journal of Physics: Conference Series **1412**, 142015 (2020).

J. Hofbrucker, A. V. Volotka, and S. Fritzsche
Nonlinear Cooper minimum as a precise tool for understanding multiphoton photoionization
Journal of Physics: Conference Series **1412**, 152017 (2020).

Y. Litvinov, T. Stöhlker, X. Ma, Y. Zhang, and T. Yamaguchi
Nuclear physics research at heavy ion accelerators: Precision studies with stored and cooled exotic nuclei
Journal of Physics: Conference Series **1401**, 012001 (2020).

E. Menz, C. Hahn, P. Pfäfflein, G. Weber, and T. Stöhlker
Performance of a scintillator-based ion detector for CRYRING@ESR
Journal of Physics: Conference Series **1412**, 232006 (2020).

T. Buhr, S. O. Stock, A. Perry-Sassmannshausen, S. Reinwardt, M. Martins, S. Ricz, A. Mueller, S. Fritzsche, and S. Schippers
Photoionization of low-charged silicon ions
Journal of Physics: Conference Series **1412**, 152024 (2020).

M. Lestinsky, Z. Andelkovic, M. Bai, A. Bräuning-Demian, V. Chetvertkova, S. Fedotova, O. Geithner, W. Geithner, O. Gorda, F. Herfurth, A. Kalinin, A. Källberg, S. Litvinov, E. Menz, K. Mohr, R. Sanchez, T. Stöhlker, G. Vorobjev, and U. Weinrich
Status of CRYRING@ESR and preparations for first experiments
Journal of Physics: Conference Series **1412**, 23007 (2020).

D. Schury, A. Méry, J. Ramillon, L. Adoui, J.-Y. Chesnel, A. Lévy, S. Macé, C. Prigent, J. Rangama, P. Rousseau, S. Steydli, M. Trassinelli, D. Vernhet, A. Gumberidze, T. Stöhlker, A. Bruning-Demian, C. Hahn, U. Spillmann, and E. Lamour
The low energy beamline of the FISIC experiment: Current status of construction and performance
Journal of Physics: Conference Series **1412**, 162011 (2020).

L. Varga, K. Blaum, T. Davinson, J. Glorius, B. Jurado, C. Langer, C. Lederer-Woods, Y. Litvinov, R. Reifarth, Z. Slavkovská, T. Stöhlker, P. Woods, and Y. Xing
Towards background-free studies of capture reactions in a heavy-ion storage ring
Journal of Physics: Conference Series **1412**, 232011 (2020).

L. Lamaignère, G. Toci, B. Patrizi, M. Vannini, A. Pirri, S. Fanetti, R. Bini, G. Mennerat, A. Melninkaitis, L. Lukas, and J. Hein
Determination of non-linear refractive index of laser crystals and ceramics via different optical techniques
Optical Materials: X **8**, 100065 (2020).

M. Seidel, P. Balla, T. Binhammer, M. Frede, G. Arisholm, L. Winkelmann, I. Hartl, and C. Heyl
Hybridizing Multi-pass and Multi-plate Bulk Compression
EPJ Web of Conferences **243**, 21001 (2020).

A.-L. Viotti, S. Alisauskas, P. Balla, A. Wahid, I. Sytcevich, C. Guo, L. Silletti, A. Cartella, H. Tavakol, U. Grosse-Wortmann, A. Schönberg, M. Seidel, B. Manschwetus, T. Lang, A. Trabattoni, F. Calegari, A. Couairon, A. L'Huillier, C. Arnold, I. Hartl, and C. Heyl
Post-compression of high average power picosecond pulses for few cycle generation and FEL pump-probe experiments
EPJ Web of Conferences **243**, 21002 (2020).

D. Dmytriiev, M. S. Sanjari, Yu. A. Litvinov, and Th. Stöhlker
Software defined radio for Schottky analysis in storage rings
Journal of Physics: Conference Series **1668**, 012014 (2020).

A. Bonanno, A. Eichhorn, H. Gies, J. Pawlowski, R. Percacci, M. Reuter, F. Saueressig, and G. Paolo Vacca
Critical reflections on asymptotically safe gravity
Frontiers in Physics **8**, 269 (2020).

M. Sanjari, D. Dmytriiev, Y. Litvinov, O. Gumenyuk, R. Hess, R. Joseph, S. Litvinov, M. Steck, and Th. Stöhlker
A 410 MHz resonant cavity pickup for heavy ion storage rings
Review of Scientific Instruments **91**, 083303 (2020).

B. Liu, J. Meyer-ter-Vehn, H. Ruhl, and M. Zepf
Front edge velocity of ultra-intense circularly polarized laser pulses in a relativistically transparent plasma
Plasma Physics and Controlled Fusion **62**, 085014 (2020).

O. Forstner, J. Müller, and K. Stiebing
Opportunities for negative ions studies at the Frankfurt Low-energy Storage Ring (FLSR)
Hyperfine Interactions **241**, 53 (2020).

L. Klar
Detectable Optical Signatures of QED Vacuum Nonlinearities Using High-Intensity Laser Fields
Particles **3**, 223 (2020).

F. Tuitje, M. Zürch, T. Helk, J. Gautier, F. Tissandier, J.-P. Goddet, E. Oliva, A. Guggenmos, U. Kleineberg, H. Stiel, S. Sebban, and C. Spielmann
Ptychography and single-shot nanoscale imaging with plasma-based laser sources
Springer Proceedings in Physics **241**, 155 (2020).

F. Karbstein
Probing Vacuum Polarization Effects with High-Intensity Lasers
Particles **3**, 39 (2020).

THESES

H. T. Olgun
Efficient high energy laser-driven multicycle terahertz generation for accelerators
Doctoral thesis
Universität Hamburg, Fakultät für Mathematik, Informatik und Naturwissenschaften, (2020).

F. Tuitje
Diffraction-based metrology in the extreme ultraviolet
Doctoral thesis
Friedrich-Schiller-Universität Jena, Physikalisch-Astronomische Fakultät, (2020).

M. Beyer
Characterization of optical components of a laser amplifier via spectral interferometry
Bachelor thesis
Friedrich-Schiller-Universität Jena, Physikalisch-Astronomische Fakultät, (2020).

M. Nolte
Charakterisierung expandierter ultradünner DLC-Folien für die Laser-Protonenbeschleunigung
Bachelor thesis
Friedrich-Schiller-Universität Jena, Physikalisch-Astronomische Fakultät, (2020).

R. Hollinger
Extreme nonlinear optics in highly excited semiconductors
Doctoral thesis
Friedrich-Schiller-Universität Jena, Physikalisch-Astronomische Fakultät, (2020).

J. Krause
Oberflächendynamik eines Plasmas im Bereich des steilen Dichtegradienten bei Wechselwirkung mit relativistischen Intensitäten
Bachelor thesis
Friedrich-Schiller-Universität Jena, Physikalisch-Astronomische Fakultät, (2020).

B. Böning
Above-threshold ionization driven by spatially structured laser fields
Doctoral thesis
Friedrich-Schiller-Universität Jena, Physikalisch-Astronomische Fakultät, (2020).

S. Ringleb
The HILITE Setup for High-Intensity-Laser Experiments with Highly Charged Ions: Design and Commissioning
Doctoral thesis
Friedrich-Schiller-Universität Jena, Physikalisch-Astronomische Fakultät, (2020).

J. Hofbrucker
Two-photon ionization of many-electron atoms
Doctoral thesis
Friedrich-Schiller-Universität Jena, Physikalisch-Astronomische Fakultät, (2020).

W. Paufler
High-Harmonic Generation with Laguerre-Gaussian Beams
Doctoral thesis
Friedrich-Schiller-Universität Jena, Physikalisch-Astronomische Fakultät, (2020).

I. Tamer
Petawatt-Class Laser Optimization and Ultrashort Probe Pulse Generation for Relativistic Laser-Plasma Interactions
Doctoral thesis
Friedrich-Schiller-Universität Jena, Physikalisch-Astronomische Fakultät, (2020).